Journal of Computational Physics 515 (2024) 113280

Contents lists available at ScienceDirect

Journal of Computational Physics

journal homepage: www.elsevier.com/locate/jcp

Nodal discontinuous Galerkin methods for Maxwell's equations in Lorentz-Kerr-Raman medium without nonlinear algebraic solver

Maohui Lyu [a], Fengyan Li [b,*]

[a] School of Sciences, Beijing University of Posts and Telecommunications, Beijing 100876, China
[b] Department of Mathematical Sciences, Rensselaer Polytechnic Institute, Troy, NY 12180, USA

ARTICLE INFO

MSC:
35Q60
65M12
78M10

Keywords:
Maxwell's equations
Kerr
Raman
Nodal discontinuous Galerkin
Linear methods
Energy stability

ABSTRACT

The propagation of electromagnetic waves is modeled by time-dependent Maxwell's equations coupled with constitutive laws that describe the responses of the media. In this work, we consider a nonlinear model that describes the electromagnetic wave in an optical medium with the linear Lorentz effect and the cubic nonlinear instantaneous Kerr and delayed Raman effects. Mathematically this model obeys an energy conservative/dissipative law. Though there have been active efforts in designing numerical methods (e.g. of finite difference / finite element /discontinuous Galerkin type) to simulate this model, the methods proposed here are distinctive in that they are free of any nonlinear algebraic solvers. Moreover, in the absence of the Raman effect, our methods also enjoy a provable discrete energy law, and optimal *a priori* error estimates are further established when the exact solutions are sufficiently smooth. The key ingredients of the new methods include some novel treatment in time discretizations and nodal discontinuous Galerkin spatial discretization for the specific nonlinearities, and they also render a local nature of the methods and hence their suitability for parallel implementation with great efficiency. Numerical experiments are performed to illustrate the accuracy, stability, computational efficiency and parallel scalability of the proposed methods. We further apply the methods to simulate some physically relevant problems in one, two, and three dimensions.

1. Introduction

Nonlinear optics is a branch of physics that studies the propagation of light in optical media whose nonlinear responses, though always exist in nature, become important. It is particularly relevant when the light intensity is high. Some examples of nonlinear optical effects include frequency mixing, high order harmonic generation and self-focusing, and they have been harnessed in many applications, such as in the optical device design and biomedical imaging etc [7,1,25]. There has been continuing need for accurate and robust computational tools for simulating and predicting the electromagnetic field behaviors in various optical media, especially based on the full-vector Maxwell's equations.

In this work, we consider the propagation of the electromagnetic waves modeled by the time-dependent Maxwell's equations in a nonlinear optical medium where the material responses include the linear Lorentz effect and the cubic nonlinear instantaneous Kerr and delayed Raman effects. The medium responses are described phenomenologically through some auxiliary differential equations (ADEs) (and indeed ordinary differential equations (ODEs)). More specifically, we consider

* Corresponding author.
E-mail addresses: mlyu@bupt.edu.cn (M. Lyu), lif@rpi.edu (F. Li).

https://doi.org/10.1016/j.jcp.2024.113280
Received 4 February 2024; Received in revised form 10 July 2024; Accepted 11 July 2024

Available online 20 July 2024

$$\mu_0 \partial_t \boldsymbol{H} + \nabla\times\boldsymbol{E} = \boldsymbol{0}, \tag{1a}$$

$$\partial_t \boldsymbol{D} - \nabla\times\boldsymbol{H} = \boldsymbol{0}, \tag{1b}$$

$$\partial_{tt} \boldsymbol{P} + \gamma \partial_t \boldsymbol{P} + \omega_0^2 \boldsymbol{P} = \omega_p^2 \boldsymbol{E}, \tag{1c}$$

$$\partial_{tt} Q + \gamma_v \partial_t Q + \omega_v^2 Q = \omega_v^2 |\boldsymbol{E}|^2, \tag{1d}$$

with suitable initial and boundary conditions on a spatial domain $\Omega \subset \mathbb{R}^d$ $(d = 1, 2, 3)$ over a time interval $[0, T]$, coupled with the constitutive relation

$$\boldsymbol{D} = \epsilon_0 \left(\epsilon_\infty \boldsymbol{E} + \boldsymbol{P} + a(1-\theta)|\boldsymbol{E}|^2 \boldsymbol{E} + a\theta Q \boldsymbol{E} \right). \tag{2}$$

Here $\boldsymbol{H}$, $\boldsymbol{E}$ are the magnetic and electric fields. $\nabla\times$ is the standard curl operator.[1] $\boldsymbol{D}$ is the electric flux density which is related to the electric field through the constitutive relation (2), including the instantaneous linear response $\epsilon_0 \epsilon_\infty \boldsymbol{E}$, the delayed linear Lorentz dispersion $\epsilon_0 \boldsymbol{P}$ whose evolution is described by the second order ODE (1c), the cubic nonlinear instantaneous Kerr response $\epsilon_0 a(1-\theta)|\boldsymbol{E}|^2 \boldsymbol{E}$, and the nonlinear delayed Raman molecular vibrational response $\epsilon_0 a\theta Q \boldsymbol{E}$. The Raman effect is modeled by a second order nonlinear ODE in (1d). μ_0 and ϵ_0 are the permeability and permittivity in the free space, and ϵ_∞ is the relative permittivity of the optical medium in the infinite frequency limit. In the ADEs (1c)-(1d), ω_0, ω_p and ω_v are the resonance frequency, plasma frequency and vibration frequency of the medium, respectively, and γ and γ_v are the non-negative damping constants. The non-negative parameter a measures the strength of the nonlinearity in the model, and θ measures the relative strength of the Kerr and Raman nonlinearities. The system is termed as the Lorentz-Kerr-Raman model, and for the special case with $\theta = 0$, it is termed as the Lorentz-Kerr model. For the convenience of reference, just as in [23], we say the model (1)-(2) is in a mixed-order form, given its PDE part (1a)-(1b) in a first order form while the ADE part (1c)-(1d) in a second order form. When the boundary conditions are periodic, one can easily verify that the model obeys an energy conservative (when $\gamma = \gamma_v = 0$) / dissipative (when $\gamma^2 + \gamma_v^2 \neq 0$) law, namely

$$\frac{d}{dt}\mathcal{E}(t) = -\frac{\epsilon_0 \gamma}{\omega_p^2} \int_\Omega |\partial_t \boldsymbol{P}|^2 d\Omega - \frac{\epsilon_0 a\theta \gamma_v}{2\omega_v^2} \int_\Omega (\partial_t Q)^2 d\Omega \le 0, \tag{3}$$

where

$$\begin{aligned} \mathcal{E}(t) = \int_\Omega \Big(& \frac{\mu_0}{2}|\boldsymbol{H}|^2 + \frac{\epsilon_0 \epsilon_\infty}{2}|\mathbf{E}|^2 + \frac{\epsilon_0}{2\omega_p^2}|\partial_t \boldsymbol{P}|^2 + \frac{\epsilon_0 \omega_0^2}{2\omega_p^2}|\mathbf{P}|^2 \\ & + \frac{3\epsilon_0 a(1-\theta)}{4}|\mathbf{E}|^4 + \frac{\epsilon_0 a\theta}{4\omega_v^2}(\partial_t Q)^2 + \frac{\epsilon_0 a\theta}{2} Q|\mathbf{E}|^2 + \frac{\epsilon_0 a\theta}{4} Q^2 \Big) d\Omega. \end{aligned} \tag{4}$$

Moreover, when $\theta \in [0, \frac{3}{4}]$, we have $\mathcal{E}(t) \ge 0$ and it defines an energy of the entire system. The aim of this work is to design efficient and accurate numerical methods, respecting the energy law (3) whenever possible, for the system (1)-(2).

To put the present work into perspective, we begin with a brief review of some relevant work that aims at preserving the energy law (3) at the numerical level. In [5], a class of (modal) discontinuous Galerkin (DG) methods was developed for the *first order form* of the system (1)-(2), after additional unknowns $\boldsymbol{J} = \partial_t \boldsymbol{P}$ and $\sigma = \partial_t Q$ were introduced, in 1D with $d = 1$. With novel techniques proposed to handle the nonlinearities based on the differentiated form of the relation $Y = E^3$ with an auxiliary unknown Y, discrete energy laws were derived and proved for the proposed schemes. This work was further extended in [22] to multiple dimensions with the vector-valued electric field in the nonlinearity, and moreover, the computational efficiency was greatly improved by using the nodal version of the DG discretizations [16] instead of the modal ones to treat nonlinearities. In [23], a family of nodal DG methods was designed for the model in the mixed-order form (1)-(2). To establish a provable energy law, an additional auxiliary field $\boldsymbol{W} = Q\boldsymbol{E}$ is introduced associated with the nonlinear Raman effect, with the differentiated form of $\boldsymbol{W} = Q\boldsymbol{E}$ discretized. The history of using finite difference time domain (FDTD) methods to simulate (1)-(2) is rather long, with the work in [13,18,15,14,12] as some examples. In [6], FDTD methods with provable energy laws were proposed in 1D. Though not explored, these methods can be generalized to 2D and 3D based on the strategies in [22] to deal with the nonlinearity. In the finite element framework, for the model with the nonlinearity of only Kerr-type (i.e. $\theta = 0$) without the linear Lorentz effect, methods with the provable energy stability/boundedness were developed in [17] when the nonlinearity is essentially 1D (i.e. the electric field is scalar), while methods were proposed in [2] for the 3D model with the energy stability/boundedness numerically investigated.

All numerical methods mentioned above involve solving local or global nonlinear algebraic equations or systems over each time step, as one would naturally expect for simulating the underlying nonlinear model. We refer to such methods as *nonlinear methods*, while terming those that are free of any nonlinear algebraic solvers/iterations as *linear methods*. To the best of our knowledge, there is no work available in literatures to design linear methods for the Maxwell's equations with both the nonlinear Kerr and Raman effects, with the (discrete analog of) energy law possibly satisfied. For the Kerr model, a linear method was proposed in [26] by

[1] When $d = 2$, the curl operator is defined as $\nabla\times\boldsymbol{E} = -\partial_y E_x + \partial_x E_y$, $\nabla\times\boldsymbol{H} = (\partial_y H_z, -\partial_x H_z)^\top$ for the transverse magnetic (TM) mode $(\boldsymbol{E}, \boldsymbol{H}) = (E_x, E_y, H_z)$, and it is $\nabla\times\boldsymbol{E} = (\partial_y E_z, -\partial_x E_z)^\top$, $\nabla\times\boldsymbol{H} = -\partial_y H_x + \partial_x H_y$ for the transverse electric (TE) mode $(\boldsymbol{E}, \boldsymbol{H}) = (E_z, H_x, H_y)$. When $d = 1$, for example with $\boldsymbol{E} = E_z$ and $\boldsymbol{H} = H_y$, the curl operator is given as $\nabla\times\boldsymbol{E} = -\partial_x E_z$, $\nabla\times\boldsymbol{H} = \partial_x H_y$.

directly using the cubic root formula to solve for the quantity $|\boldsymbol{E}_h^{n+1}|^2$. For the Lorentz-Kerr-Raman model, by using the electric field value at the previous time step to linearize the constitutive relation, a first-order FDTD linear scheme was proposed in [27]. A comparison for the linear schemes in [26,27] and an iterative scheme was performed in [24] to simulate the Kerr model, and the cost effectiveness of non-iterative schemes was demonstrated in 1D and was projected for high dimensions. For the Lorentz-Kerr model, FDTD linear methods with the second order accuracy were proposed in [11] by utilizing two copies of solutions on dual grids staggered in time, and also recently in [21] without the redundancy in solution approximations on dual grids based on a different second order discretization for (2) when $\theta = 0$. None of these linear methods mentioned above however obey the (discrete analogue of) energy law (3) rigorously.

The main contribution of this work is to design a class of linear methods for the Maxwell's equations in a nonlinear optical medium modeled by (1)-(2) in any space dimensions, and no nonlinear algebraic equation/system needs to be solved as time progresses. The design of the methods is based on the model in its mixed-order form just as (1)-(2). For the constitutive relation (2) and the associated ADEs (1c)-(1d) (and some derived equations, i.e. for $\boldsymbol{Y}$ and $\boldsymbol{W}$, as one will see), the time integrators are second order accurate and two-step, with the latter involving three time levels and hence providing the opportunity for one to properly linearize the nonlinear terms. To possibly achieve a provable discrete energy law, an auxiliary field $\boldsymbol{Y}$ is introduced as $\boldsymbol{Y} = |\boldsymbol{E}|^2\boldsymbol{E}$ for the Kerr nonlinearity as in [5,22] and this relation is then differentiated and discretized with second order accuracy, and moreover, suitable discretization is formulated for the linear Lorentz term. Similarly, for the Raman nonlinearity, we introduce an auxiliary field $\boldsymbol{W} = \boldsymbol{Q}\boldsymbol{E}$ as in [23], again with the differentiated form of this relation properly discretized, along with a specific linearization of $|\boldsymbol{E}|^2$ in (1d). For the PDE part (1a)-(1b), the second order staggered leap-frog temporal discretization is applied together with the nodal DG space discretizations (of any accuracy) and suitably chosen numerical fluxes. This leads to an explicit treatment for the PDE operator. In other words, temporal implicitness of the proposed methods only comes from the ADE part, and this, combined with the nodal DG strategy, makes the implicitness extremely local and indeed associated with each interpolation point (that arises from the nodal DG framework), also see the discussions in Section 2. As a consequence, the proposed methods have high parallel efficiency similarly to standard explicit DG methods for hyperbolic problems [3]. The efficiency is further enhanced with the proposed methods being linear. For the Lorentz-Kerr model with $\theta = 0$, the existence and uniqueness of the discrete solution over each time step is also established, and additionally, a discrete analogue of the energy law (3) is proved. Such theoretical results are not available when the methods are applied to the general Lorentz-Kerr-Raman model. Motivated by the findings for the case of $\theta = 0$, a discrete quasi-energy is introduced for the general model and numerically monitored over time (see Fig. 5 in Section 4.1.2, Fig. 7 in Section 4.2.1). This will provide evidence that the proposed methods are stable when they are applied to the general Lorentz-Kerr-Raman model. Furthermore, for the Lorentz-Kerr model, *a priori* error estimates are established when the exact solutions are sufficiently smooth. The results are optimal with respect to the temporal local truncation errors and the approximation properties of the discrete space, under a relatively standard time step condition when the model is linear (with $a = 0$), yet under a more restrictive time step condition along with some constraint on the approximation order of the discrete space for the general model.

The rest of the paper is organized as follows. In Section 2, a family of fully discrete linear methods is formulated for the system (1)-(2). In Section 3, we establish the unique solvability and a discrete energy law of the methods when they are applied to the Lorentz-Kerr model, and discuss these aspects when the methods are applied to the general case. For the Lorentz-Kerr model, error analysis is also performed in this section. The performance of the proposed methods is demonstrated numerically in Section 4, followed by the concluding remarks in Section 5.

2. Proposed numerical methods

In this section, we will formulate a class of linear methods for the nonlinear optical model (1)-(2). The methods will be second order accurate in time and can be arbitrary order accurate in space, with great computational efficiency ensured by the local nature of the methods due to their explicitness for the PDE part, nodal DG discretizations in space for nonlinearities, and also by the linear nature of the methods as a result of the temporal discretizations suitably designed for both linear and nonlinear terms of the model. A discrete analogue of the energy law will be demonstrated numerically for the full Lorentz-Kerr-Raman model, and will be established rigorously for the Lorentz-Kerr model in next section. In our presentation, d_E is the number of the components of the electric field $\boldsymbol{E}$. We always have $d_E \le d$, with the inequality possible, e.g. in the transverse magnetic (TM) mode in 2D when $d = 2$ and $d_E = 1$.

Mesh and discrete space. Our presentation will be for three dimensions with $d = 3$, and it can be easily adapted to the cases of $d = 1, 2$. Boundary conditions for $\boldsymbol{E}$ and $\boldsymbol{H}$ are assumed to be periodic. Let the spatial domain be $\Omega = [x_a, x_b]\times[y_a, y_b]\times[z_a, z_b]$, with a Cartesian mesh

$$\mathcal{T}_h = \left\{K :\ K = I_{ix}\times I_{iy}\times I_{iz},\ 1 \le ix \le N_x,\ 1 \le iy \le N_y,\ 1 \le iz \le N_z\right\},$$

where $I_{i\zeta} = [\zeta_{i\zeta-\frac{1}{2}}, \zeta_{i\zeta+\frac{1}{2}}]$ is a subinterval in the partition of $[\zeta_a, \zeta_b]$: $\zeta_a = \zeta_{\frac{1}{2}} < \zeta_{\frac{3}{2}} < \cdots < \zeta_{N_\zeta+\frac{1}{2}} = \zeta_b$, with $\zeta = x, y, z$. For each element $K = I_{ix}\times I_{iy}\times I_{iz}$, we denote its center as (x_c^K, y_c^K, z_c^K), and its length in the ζ-direction as $\Delta\zeta^K = \zeta_{i\zeta+\frac{1}{2}} - \zeta_{i\zeta-\frac{1}{2}}$, $\zeta = x, y, z$. We write $h = \max\limits_{K\in\mathcal{T}_h,\zeta=x,y,z}\Delta\zeta^K$, and use $\mathcal{F}_h$ to denote the collection of inter-element faces of $\mathcal{T}_h$. We further assume the mesh is quasi-uniform, namely, there exists a constant δ such that $h \le \delta\Delta\zeta^K, \zeta = x, y, z, \forall K \in \mathcal{T}_h$ as the mesh is refined.

Associated with $\mathcal{T}_h$, we introduce a finite dimensional function space

$$V_h^k = \left\{v \in L^2(\Omega) :\ v|_K \in Q^k(K), \forall K \in \mathcal{T}_h\right\}. \tag{5}$$

Here, $Q^k(K)$ is the set of tensor-type polynomials of degree up to k in each variable on K. Without confusion, we will use the same notation V_h^k to represent its vector version. Note that the functions in V_h^k can be discontinuous at inter-element interfaces. For each given $F = \overline{K^+} \cap \overline{K^-}$ in $\mathcal{F}_h$, we designate a unit normal $\boldsymbol{n}_F$ such that $\boldsymbol{n}_F \cdot (1,1,1)^\top > 0$, with $\boldsymbol{n}_F$ as the outward normal along the boundary of K^+. We then define the jump of a function $\boldsymbol{u} \in V_h^k$ across F as $[\![\boldsymbol{u}]\!]_F = \boldsymbol{u}^+ - \boldsymbol{u}^-$, where $\boldsymbol{u}^\pm$ are the traces of $\boldsymbol{u}$ along F from the element $K^\pm$. The standard notation $(\cdot,\cdot)$ will be used as the L^2 inner product for $L^2(\Omega)$, and $\|\cdot\|$ is the associated L^2-norm.

Interpolation operator. For the computational efficiency especially when handling the nonlinearity, nodal DG discretizations will be adopted in space, and this will rely on an interpolation operator $\mathcal{I}_h$. We will describe this operator following the presentation in [22] that is for two dimensions. Let $\{\xi_m\}_{m=0}^k$ be the $k+1$ Gauss-Legendre quadrature points on the interval $[-1,1]$ with the positive weights $\{\widehat{\omega}_m\}_{m=0}^k$, satisfying $\sum_{k=0}^m \widehat{\omega}_m = 2$. The corresponding numerical quadrature is exact for polynomials of degree up to $2k+1$ (i.e. for functions in $P^{2k+1}([-1,1])$). Let $\{\mathcal{L}_n(\xi)\}_{n=0}^k$ be the Lagrange basis of $P^k([-1,1])$, satisfying $\mathcal{L}_n(\xi_m) = \delta_{mn}$. Here δ_{mn} is the Kronecker delta. In each element $K = I_{ix} \times I_{iy} \times I_{iz}$, we define

$$\phi_{lmn}^K(x,y,z) = \mathcal{L}_l\Big(\frac{x - x_c^K}{\Delta x^K/2}\Big)\mathcal{L}_m\Big(\frac{y - y_c^K}{\Delta y^K/2}\Big)\mathcal{L}_n\Big(\frac{z - z_c^K}{\Delta z^K/2}\Big), \tag{6}$$

then $\{\phi_{lmn}^K(x,y,z)\}_{l,m,n=0}^k$ forms an orthogonal basis for $V_h^k|_K = Q^k(K)$ with respect to the L^2 inner product on K. We now can introduce a local interpolation operator $\mathcal{I}_h^K : C(K) \mapsto Q^k(K)$,

$$(\mathcal{I}_h^K f)(x,y,z) = \sum_{l,m,n=0}^k f(x_l^K, y_m^K, z_n^K)\phi_{lmn}^K(x,y,z), \quad (x,y,z) \in K, \tag{7}$$

with $x_l^K = x_c^K + \xi_l \Delta x^K/2$, $y_m^K = y_c^K + \xi_m \Delta y^K/2$, $z_n^K = z_c^K + \xi_n \Delta z^K/2$, and $C(K)$ denotes the space of continuous functions on K. It is easy to see that $\big(\mathcal{I}_h^K f\big)(x_l^K, y_m^K, z_n^K) = f(x_l^K, y_m^K, z_n^K)$, $\forall l,m,n = 0,\cdots,k$. A global interpolation operator $\mathcal{I}_h$ is then defined as $\mathcal{I}_h : W_h(\Omega) \mapsto V_h^k$, with $\mathcal{I}_h\Big|_K = \mathcal{I}_h^K$, where $W_h(\Omega) = \{f \in L^2(\Omega),\ f|_K \in C(K), \forall K \in \mathcal{T}_h\}$. Here again we also use $\mathcal{I}_h$ to represent its vector version.

Numerical methods. Let $0 = t^0 < t^1 < \cdots < t^{N_t} = T$ be a uniform partition of $[0,T]$ with $t^n = n\tau$, $\tau = T/N_t$. In addition, $t^{n+\frac{1}{2}} = \frac{1}{2}(t^n + t^{n+1})$. We are now ready to present our proposed numerical methods for (1)-(2). Given u_h^n, $u_h^{n-1} \in V_h^k$, $u = \boldsymbol{D}$, $\boldsymbol{E}$, $\boldsymbol{P}$, Q and $\boldsymbol{H}_h^{n+1/2} \in V_h^k$, find $u_h^{n+1} \in V_h^k$, $u = \boldsymbol{D}$, $\boldsymbol{E}$, $\boldsymbol{P}$, Q and $\boldsymbol{H}_h^{n+3/2} \in V_h^k$, satisfying

PDEs:

$$\Big(\frac{\boldsymbol{D}_h^{n+1} - \boldsymbol{D}_h^n}{\tau}, \boldsymbol{\phi}\Big) + \mathcal{B}_h^H(\boldsymbol{H}_h^{n+1/2}, \boldsymbol{\phi}) = 0, \quad \forall \boldsymbol{\phi} \in V_h^k, \tag{8a}$$

$$\mu_0\Big(\frac{\boldsymbol{H}_h^{n+3/2} - \boldsymbol{H}_h^{n+1/2}}{\tau}, \boldsymbol{\phi}\Big) + \mathcal{B}_h^E\left(\boldsymbol{E}_h^{n+1}, \boldsymbol{\phi}\right) = 0, \quad \forall \boldsymbol{\phi} \in V_h^k, \tag{8b}$$

Constitutive relation (including ADEs):

$$\boldsymbol{D}_h^{n+1} = \epsilon_0\Big(\epsilon_\infty \boldsymbol{E}_h^{n+1} + \boldsymbol{P}_h^{n+1} + a(1-\theta)\boldsymbol{Y}_h^{n+1} + a\theta \boldsymbol{W}_h^{n+1}\Big), \tag{8c}$$

$$\boldsymbol{Y}_h^{n+1} - \boldsymbol{Y}_h^{n-1} = \mathcal{I}_h\Big(\left|\boldsymbol{E}_h^n\right|^2(\boldsymbol{E}_h^{n+1} - \boldsymbol{E}_h^{n-1}) + 2\left(\boldsymbol{E}_h^n \cdot (\boldsymbol{E}_h^{n+1} - \boldsymbol{E}_h^{n-1})\right)\boldsymbol{E}_h^n\Big), \tag{8d}$$

$$\boldsymbol{W}_h^{n+1} - \boldsymbol{W}_h^{n-1} = \mathcal{I}_h\Big((Q_h^{n+1} - Q_h^{n-1})\boldsymbol{E}_h^n + Q_h^n(\boldsymbol{E}_h^{n+1} - \boldsymbol{E}_h^{n-1})\Big), \tag{8e}$$

$$\frac{\boldsymbol{P}_h^{n+1} - 2\boldsymbol{P}_h^n + \boldsymbol{P}_h^{n-1}}{\tau^2} + \gamma\frac{\boldsymbol{P}_h^{n+1} - \boldsymbol{P}_h^{n-1}}{2\tau} + \omega_0^2\frac{\boldsymbol{P}_h^{n+1} + \boldsymbol{P}_h^{n-1}}{2} = \omega_p^2\frac{\boldsymbol{E}_h^{n+1} + \boldsymbol{E}_h^{n-1}}{2}, \tag{8f}$$

$$\frac{Q_h^{n+1} - 2Q_h^n + Q_h^{n-1}}{\tau^2} + \gamma_v\frac{Q_h^{n+1} - Q_h^{n-1}}{2\tau} + \omega_v^2\frac{Q_h^{n+1} + Q_h^{n-1}}{2} = \omega_v^2\mathcal{I}_h\Big(\boldsymbol{E}_h^n \cdot \frac{\boldsymbol{E}_h^{n+1} + \boldsymbol{E}_h^{n-1}}{2}\Big). \tag{8g}$$

Here, the bilinear forms $\mathcal{B}_h^H(\boldsymbol{H}_h^{n+1/2}, \boldsymbol{\phi})$ and $\mathcal{B}_h^E(\boldsymbol{E}_h^{n+1}, \boldsymbol{\phi})$ are defined as

$$\mathcal{B}_h^H(\boldsymbol{H}_h^{n+1/2}, \boldsymbol{\phi}) = -\Big(\boldsymbol{H}_h^{n+1/2}, \nabla\times\boldsymbol{\phi}\Big) - \sum_{F\in\mathcal{F}_h}\Big\langle \boldsymbol{n}_F \times \widetilde{\boldsymbol{H}_h^{n+1/2}}, [\![\boldsymbol{\phi}]\!]\Big\rangle_F, \tag{9a}$$

$$\mathcal{B}_h^E(\boldsymbol{E}_h^{n+1}, \boldsymbol{\phi}) = \big(\boldsymbol{E}_h^{n+1}, \nabla\times\boldsymbol{\phi}\big) + \sum_{F\in\mathcal{F}_h}\Big\langle \boldsymbol{n}_F \times \widehat{\boldsymbol{E}_h^{n+1}}, [\![\boldsymbol{\phi}]\!]\Big\rangle_F, \tag{9b}$$

where $\widetilde{\boldsymbol{H}_h^{n+1/2}}$ and $\widehat{\boldsymbol{E}_h^{n+1}}$ are numerical fluxes,

$$\widetilde{\boldsymbol{H}_h^{n+1/2}} = \beta \boldsymbol{H}_h^{n+1/2,-} + (1-\beta)\boldsymbol{H}_h^{n+1/2,+}, \quad \widehat{\boldsymbol{E}_h^{n+1}} = (1-\beta)\boldsymbol{E}_h^{n+1,-} + \beta \boldsymbol{E}_h^{n+1,+}, \tag{10}$$

with a constant parameter β. Particularly, they will give the commonly used alternating fluxes when $\beta = 0$ and $\beta = 1$, to be used in this work and referred to as

$$\text{Alternating I}: \quad \widetilde{\boldsymbol{H}_h^{n+1/2}} = \boldsymbol{H}_h^{n+1/2,+}, \quad \widehat{\boldsymbol{E}_h^{n+1}} = \boldsymbol{E}_h^{n+1,-}, \tag{11a}$$

$$\text{Alternating II}: \quad \widetilde{\boldsymbol{H}_h^{n+1/2}} = \boldsymbol{H}_h^{n+1/2,-}, \quad \widehat{\boldsymbol{E}_h^{n+1}} = \boldsymbol{E}_h^{n+1,+}. \tag{11b}$$

For any given $\boldsymbol{\psi} \in V_h^k$, it is easy to check that $\mathcal{B}_h^H(\boldsymbol{\psi}, \cdot)$ is a linear bounded functional on V_h^k. Based on Riesz representation, there exists a unique function $\boldsymbol{\varphi} \in V_h^k$ such that $\mathcal{B}_h^H(\boldsymbol{\psi}, \boldsymbol{\phi}) = (\boldsymbol{\varphi}, \boldsymbol{\phi}), \forall \boldsymbol{\phi} \in V_h^k$. This defines a (linear bounded) discrete curl operator $\nabla_h \times : \boldsymbol{\psi} \mapsto -\boldsymbol{\varphi}$ from V_h^k to V_h^k, and therefore

$$\mathcal{B}_h^H(\boldsymbol{\psi}, \boldsymbol{\phi}) = -(\nabla_h \times \boldsymbol{\psi}, \boldsymbol{\phi}), \quad \forall \boldsymbol{\phi} \in V_h^k. \tag{12}$$

The equation (9a) can be further written into its strong form

$$\frac{\boldsymbol{D}_h^{n+1} - \boldsymbol{D}_h^n}{\tau} = \nabla_h \times \boldsymbol{H}_h^{n+1/2}. \tag{13}$$

Discussions. Below are a few remarks we would like to make for the proposed methods.

1.) The most distinctive property of the proposed methods, unlike any of the methods we previously developed in [5,22,23] for (1)-(2) or its first order form, is that the methods here are *linear* and free of any nonlinear algebraic solvers/iterations. This can also be seen from the flow chart of the overall methods in Algorithm 1.

2.) Similar as in our previous work, the nonlinear Kerr term $|\boldsymbol{E}|^2\boldsymbol{E}$ and the nonlinear Raman term $Q\boldsymbol{E}$ in the constitutive relation are discretized based on the differentiated forms of two additional auxiliary relations, $\boldsymbol{Y} = |\boldsymbol{E}|^2\boldsymbol{E}$ and $\boldsymbol{W} = Q\boldsymbol{E}$, namely,

$$\partial_t \boldsymbol{Y} = |\boldsymbol{E}|^2 \partial_t \boldsymbol{E} + 2(\boldsymbol{E} \cdot \partial_t \boldsymbol{E})\boldsymbol{E}, \quad \partial_t \boldsymbol{W} = \boldsymbol{E}\partial_t Q + Q\partial_t \boldsymbol{E}. \tag{14}$$

The two auxiliary unknowns $\boldsymbol{Y}$ and $\boldsymbol{W}$ need not be solved in actual implementation as discussed in [23], also see Algorithm 1.

3.) The proposed methods are based on a second order staggered leap-frog method in time for the PDE part (1a)-(1b), linear two-step temporal discretizations of second order accuracy for the ADEs (1c)-(1d) and for the two additional auxiliary equations we introduced in (14), along with suitable temporal treatments of linear and nonlinear terms, and nodal DG discretizations of any formal order of accuracy in space.

4.) To implement the proposed methods, one still needs to solve linear algebraic systems. With the explicit-in-time staggered leap-frog method applied to the PDE part as in (8a)-(8b), the linear systems to be solved, though being variable-coefficient after the linearization or frozen-coefficient like treatment of the nonlinear terms (e.g. see (8d), (8e), (8g)), are related to the ADEs (also ODEs) and therefore spatially local. This will become more clear if one notes that, with the nodal treatment in space, a nonlinear relation such as (8e) is equivalent to

$$(\boldsymbol{W}_h^{n+1} - \boldsymbol{W}_h^{n-1})(x_l^K, y_m^K, z_n^K) = ((Q_h^{n+1} - Q_h^{n-1})\boldsymbol{E}_h^n + Q_h^n(\boldsymbol{E}_h^{n+1} - \boldsymbol{E}_h^{n-1}))(x_l^K, y_m^K, z_n^K),$$

$\forall l, m, n = 0, \cdots, k$, $\forall K \in \mathcal{T}_h$, hence the linear system on each element K is further decoupled. Indeed, one linear system of the size $d_E \times d_E$ needs to be solved at each interpolation point (x_l^K, y_m^K, z_n^K) to update the unknown electric field $\boldsymbol{E}_h$ (of d_E components) at this point over one time step. Therefore the proposed methods are very efficient, especially within the parallel implementation environment, as to be demonstrated in Section 4.1.2. In contrast, for the methods in [23], one nonlinear system of the size $d_E \times d_E$ needs to be solved at each interpolation point.

5.) There is some subtle difference between the discretizations here and in our previous work even for linear terms. Using the zeroth-order terms $\boldsymbol{P}$ and $\boldsymbol{E}$ in (1c) as an example, in [23], a central discretization $\frac{u_h^{n+1} + 2u_h^n + u_h^{n-1}}{4}$, $u = \boldsymbol{P}$, $\boldsymbol{E}$, was employed, with which, a discrete energy relation can be identified in the presence of both Kerr and Raman nonlinearities. Here in this work, in order to prove an energy law for the Lorentz-Kerr model (see Theorem 2) without any nonlinear algebraic iterations in the entire algorithm, it is necessary to make some modification as in (8f) to discretize the $\boldsymbol{P}$ and $\boldsymbol{E}$ terms.

6.) Upwind-type numerical fluxes as in [5] are not used here for the PDE part (8a)-(8b), as they will lead to an implicit discretization when coupled with the staggered leap-frog temporal discreization hence reduce the efficiency of the fully discrete schemes.

Note that the proposed schemes (8)-(9) are multi-step methods. In addition to the initialization at $t = 0$ through interpolation, the one-step methods in [5,22] are applied to obtain $\boldsymbol{H}_h^{1/2}$ and u_h^1, $u = \boldsymbol{E}$, $\boldsymbol{P}$ and Q for the initialization. The flow chart to implement the proposed linear methods in 3D is summarized in Algorithm 1. One can see that in the main part of the algorithm, our methods indeed update $\boldsymbol{E}, \boldsymbol{P}, Q$ as time progresses, with $\boldsymbol{D}, \boldsymbol{Y}, \boldsymbol{W}$ being auxiliary variables.

3. Solvability, discrete energy law, and error estimates

In this section, we will examine the solvability of the proposed methods, introduce the discrete energy, and establish the associated energy law if available. *A priori* error estimates will also be established for the proposed methods when they are applied to the linear

Algorithm 1: The flow chart to implement the proposed methods.

Initialization: Starting with $u_h^0 = (I_h u)(\cdot, t=0)$, $u = \boldsymbol{H}, \boldsymbol{E}, \boldsymbol{P}, \partial_t \boldsymbol{P}, Q, \partial_t Q, \boldsymbol{D}$,

(i) compute $\boldsymbol{H}_h^{1/2}$ explicitly via $\mu_0\Big(\frac{\boldsymbol{H}_h^{1/2}-\boldsymbol{H}_h^0}{\tau/2}, \boldsymbol{\phi}\Big) + \mathcal{B}_h^E\left(\boldsymbol{E}_h^0, \boldsymbol{\phi}\right) = 0,\ \forall\, \boldsymbol{\phi} \in V_h^k$;

(ii) compute u_h^1, $u = \boldsymbol{E}, \boldsymbol{P}, Q$ using (the 3D version of) the one-step nonlinear methods in [22] of the same spatial accuracy;

(iii) compute $\boldsymbol{H}_h^{3/2}$ explicitly via (8b).

Time marching: For $n = 1, ..., N_t - 1$,

(**S.1**) compute $\boldsymbol{D}_h^{n+1} - \boldsymbol{D}_h^{n-1}$ explicitly based on two time steps of (8a);

(**S.2**) in a fully decoupled fashion, at each interpolation point (x_l^K, y_m^K, z_n^K), $\forall l, m, n = 0, \cdots, k, \forall K \in \mathcal{T}_h$,

- update $\boldsymbol{E}_h^{n+1}$ by solving a $d_E \times d_E$ system of linear equations derived from (8c)-(8g);
- update $\boldsymbol{P}_h^{n+1}$ and Q_h^{n+1} based on the analytical formulations derived from (8f)-(8g).

(**S.3**) update $\boldsymbol{H}_h^{n+3/2}$ explicitly using (8b).

model with $\theta = a = 0$ and to the Lorentz-Kerr model ($\theta = 0$), when the exact solutions are sufficiently smooth. From here on, vectors by default are column vectors.

3.1. Solvability

Over each time step, a linear system of $d_E \times d_E$ ($d_E \le d$) needs to be solved at each interpolation point (x_l^K, y_m^K, z_n^K), $\forall l, m, n = 0, \cdots, k, \forall K \in \mathcal{T}_h$. Its unique solvability will be established next for the Lorentz-Kerr model with $\theta = 0$.

Theorem 1 *(Existence and uniqueness). With $\theta = 0$, the numerical solution of the proposed methods (8)-(9) is uniquely solvable.*

Proof. Assume $\boldsymbol{H}_h^{n-1/2}, \boldsymbol{H}_h^{n+1/2}, \boldsymbol{E}_h^{n-1}, \boldsymbol{E}_h^n, \boldsymbol{P}_h^{n-1}, \boldsymbol{P}_h^n$ are available. With the local property of the methods, one can see that the unique solvability of the solution will boil down to the unique solvability of $\boldsymbol{E}_h^{n+1}$ at each interpolation point (x_l^K, y_m^K, z_n^K), $\forall l, m, n = 0, \cdots, k, \forall K \in \mathcal{T}_h$.

Following Algorithm 1, we first compute $\boldsymbol{D}_h^{n+1} - \boldsymbol{D}_h^{n-1}$ based on two time steps of (8a), or its strong form (13), obtaining

$$\boldsymbol{D}_h^{n+1} - \boldsymbol{D}_h^{n-1} = \tau \nabla_h \times (\boldsymbol{H}_h^{n+1/2} + \boldsymbol{H}_h^{n-1/2}). \tag{15}$$

Based on (8c) with $\theta = 0$, (8d), (8f), we further have

$$\boldsymbol{D}_h^{n+1} - \boldsymbol{D}_h^{n-1} = \epsilon_0\Big(\epsilon_\infty(\boldsymbol{E}_h^{n+1} - \boldsymbol{E}_h^{n-1}) + (\boldsymbol{P}_h^{n+1} - \boldsymbol{P}_h^{n-1}) + a(\boldsymbol{Y}_h^{n+1} - \boldsymbol{Y}_h^{n-1})\Big), \tag{16a}$$

$$\boldsymbol{Y}_h^{n+1} - \boldsymbol{Y}_h^{n-1} = \mathcal{I}_h\Big(\big(\left|\boldsymbol{E}_h^n\right|^2 \mathbb{I} + 2\boldsymbol{E}_h^n(\boldsymbol{E}_h^n)^\top\big)(\boldsymbol{E}_h^{n+1} - \boldsymbol{E}_h^{n-1})\Big), \tag{16b}$$

$$\boldsymbol{P}_h^{n+1} - \boldsymbol{P}_h^{n-1} = \frac{\omega_p^2\tau^2(\boldsymbol{E}_h^{n+1} - \boldsymbol{E}_h^{n-1})}{2 + \gamma\tau + \omega_0^2\tau^2} + \frac{4(\boldsymbol{P}_h^n - \boldsymbol{P}_h^{n-1}) - 2\omega_0^2\tau^2\boldsymbol{P}_h^{n-1} + 2\omega_p^2\tau^2\boldsymbol{E}_h^{n-1}}{2 + \gamma\tau + \omega_0^2\tau^2}. \tag{16c}$$

Here $\mathbb{I}$ is the identify matrix of $d_E \times d_E$.

We now consider all the equations above at a given interpolation point, and write $\boldsymbol{E}_h^m$ at this point as $\boldsymbol{e}^m \in \mathbb{R}^{d_E}$, $m = n+1, n-1$. The equations are now linear in $\boldsymbol{e}^{n+1} - \boldsymbol{e}^{n-1}$. In fact, $\boldsymbol{e}^{n+1} - \boldsymbol{e}^{n-1}$ satisfies

$$\mathbb{A}(\boldsymbol{e}^{n+1} - \boldsymbol{e}^{n-1}) = \boldsymbol{S}^n, \tag{17}$$

with the coefficient matrix as

$$\mathbb{A} = \epsilon_0\Big(\epsilon_\infty + \frac{\omega_p^2\tau^2}{2 + \gamma\tau + \omega_0^2\tau^2}\Big)\mathbb{I} + \epsilon_0 a\left(|\boldsymbol{e}^n|^2\,\mathbb{I} + 2\boldsymbol{e}^n(\boldsymbol{e}^n)^\top\right),$$

and the source term $\boldsymbol{S}^n$ as

$$\boldsymbol{S}^n = \tau\nabla_h \times (\boldsymbol{H}_h^{n+1/2} + \boldsymbol{H}_h^{n-1/2}) - \epsilon_0 \frac{4(\boldsymbol{P}_h^n - \boldsymbol{P}_h^{n-1}) - 2\omega_0^2\tau^2\boldsymbol{P}_h^{n-1} + 2\omega_p^2\tau^2\boldsymbol{E}_h^{n-1}}{2 + \gamma\tau + \omega_0^2\tau^2}, \tag{18}$$

with the term on the right evaluated at the interpolation point. Note that $\mathbb{A}$ is symmetric positive definite, and this ensures the unique solvability of $\boldsymbol{e}^{n+1} - \boldsymbol{e}^{n-1}$, hence of $\boldsymbol{e}^{n+1}$. □

Remark 1. For the general case with $\theta \neq 0$, unique solvability of the numerical solution of the proposed methods can be similarly established if one can prove that the respective matrix $\mathbb{A}$ at each interpolation point, namely,

$$\mathbb{A} = \epsilon_0\Big(\epsilon_\infty + \frac{\omega_p^2\tau^2}{2 + \gamma\tau + \omega_0^2\tau^2}\Big)\mathbb{I} + \epsilon_0 a(1-\theta)\left(|\boldsymbol{e}^n|^2\,\mathbb{I} + 2\boldsymbol{e}^n(\boldsymbol{e}^n)^\top\right) + \epsilon_0 a\theta\Big(\frac{\omega_v^2\tau^2}{2 + \gamma_v\tau + \omega_v^2\tau^2}\boldsymbol{e}^n(\boldsymbol{e}^n)^\top + q^n\mathbb{I}\Big)$$

is invertible. Here e^n, q^n are $\boldsymbol{E}_h^n, Q_h^n$ at this interpolation point, respectively. This would require some nontrivial *a priori* bound estimate of the numerical solution Q_h^n, and such estimate is unavailable at this point.

3.2. Discrete energy and energy law

Next we will state and prove that the proposed methods (8)-(9) for the Lorentz-Kerr model (with $\theta = 0$) satisfy a discrete analogue of the energy law (3). To prepare, we will start with an identity

$$\mathcal{B}_h^H(\boldsymbol{\phi}, \boldsymbol{\psi}) + \mathcal{B}_h^E(\boldsymbol{\psi}, \boldsymbol{\phi}) = 0, \quad \forall\, \boldsymbol{\phi}, \boldsymbol{\psi} \in V_h^k, \tag{19}$$

under the assumption of periodic boundary conditions, and it can be verified by using $\nabla\cdot(\boldsymbol{\phi}\times\boldsymbol{\psi}) = \boldsymbol{\psi}\cdot(\nabla\times\boldsymbol{\phi}) - \boldsymbol{\phi}\cdot(\nabla\times\boldsymbol{\psi})$, and an equality for the adopted numerical fluxes in (10),

$$\left\langle [\![\boldsymbol{\phi}\times\boldsymbol{\psi}]\!], \boldsymbol{n}_F \right\rangle_F + \left\langle \boldsymbol{n}_F\times\widehat{\boldsymbol{\psi}}, [\![\boldsymbol{\phi}]\!] \right\rangle_F - \left\langle \boldsymbol{n}_F\times\widetilde{\boldsymbol{\phi}}, [\![\boldsymbol{\psi}]\!] \right\rangle_F = 0, \quad \forall\, \boldsymbol{\phi}, \boldsymbol{\psi} \in V_h^k.$$

The following lemma presents an inequality that will be used repeatedly in our analysis, and it can be obtained based on some standard inverse inequalities associated with polynomial spaces (see [9], or Lemma A.4 in [22]) and Cauchy-Schwartz inequality.

Lemma 1. *The following holds*

$$\left|\mathcal{B}_h^E(\boldsymbol{\psi}, \boldsymbol{\phi})\right| \le \frac{C_\star}{h}\|\boldsymbol{\psi}\|\,\|\boldsymbol{\phi}\| \le \frac{C_\star}{2h}\left(\frac{1}{\vartheta}\|\boldsymbol{\psi}\|^2 + \vartheta\|\boldsymbol{\phi}\|^2\right),\ \forall\, \boldsymbol{\psi}, \boldsymbol{\phi} \in V_h^k,\ \forall \vartheta > 0. \tag{20}$$

Here $C_\star$ is a constant independent of the meshsize h and the time step τ, yet depending on the polynomial degree k and the parameter δ related to the non-uniformness of the mesh.

Theorem 2 *(Discrete energy law). With $\theta = 0$ and periodic boundary conditions, the numerical solution of the proposed methods (8)-(9) with numerical fluxes (10) satisfies the energy law*

$$\mathcal{E}_{h,LK}^{n+1/2} - \mathcal{E}_{h,LK}^{n-1/2} = -\frac{\epsilon_0\gamma\tau}{\omega_p^2}\int_\Omega \left|\frac{\boldsymbol{P}_h^{n+1} - \boldsymbol{P}_h^{n-1}}{2\tau}\right|^2 d\Omega \le 0, \tag{21}$$

where the discrete energy $\mathcal{E}_{h,LK}^{n+1/2}$ at $t = t^{n+\frac{1}{2}}$ is defined as

$$\begin{aligned}\mathcal{E}_{h,LK}^{n+1/2} = \int_\Omega \Bigg(&\mu_0 \frac{\boldsymbol{H}_h^{n+3/2} + \boldsymbol{H}_h^{n+1/2}}{2}\cdot\frac{\boldsymbol{H}_h^{n+1/2} + \boldsymbol{H}_h^{n-1/2}}{2} - \frac{\mu_0}{2}\left|\boldsymbol{H}_h^{n+1/2}\right|^2 \\ &+ \frac{\epsilon_0\epsilon_\infty}{2}\frac{\left|\boldsymbol{E}_h^{n+1}\right|^2 + \left|\boldsymbol{E}_h^{n}\right|^2}{2} + \frac{\epsilon_0}{2\omega_p^2}\left|\frac{\boldsymbol{P}_h^{n+1} - \boldsymbol{P}_h^{n}}{\tau}\right|^2 + \frac{\epsilon_0\omega_0^2}{2\omega_p^2}\frac{\left|\boldsymbol{P}_h^{n+1}\right|^2 + \left|\boldsymbol{P}_h^{n}\right|^2}{2} \\ &+ \frac{\epsilon_0 a}{4} I_h\left(\left|\boldsymbol{E}_h^{n+1}\right|^2\left|\boldsymbol{E}_h^{n}\right|^2 + 2\left(\boldsymbol{E}_h^{n+1}\cdot\boldsymbol{E}_h^{n}\right)^2\right)\Bigg) d\Omega.\end{aligned} \tag{22}$$

Furthermore, $\mathcal{E}_{h,LK}^{n+1/2} \ge 0$ under the following CFL condition for the time step size τ,

$$v_\infty\frac{\tau}{h} \le \frac{2-\sqrt{3}}{C_\star}, \tag{23}$$

where $v_\infty = \frac{1}{\sqrt{\epsilon_0\epsilon_\infty\mu_0}}$ is the velocity of light in the optical medium.

Proof. Step 1: to establish the energy law (21)-(22). Applying two time steps to (8a) and (8b) respectively, we have

$$\left(\frac{\boldsymbol{D}_h^{n+1} - \boldsymbol{D}_h^{n-1}}{2\tau}, \boldsymbol{\phi}\right) + \mathcal{B}_h^H\left(\frac{\boldsymbol{H}_h^{n+1/2} + \boldsymbol{H}_h^{n-1/2}}{2}, \boldsymbol{\phi}\right) = 0,\ \forall \boldsymbol{\phi} \in V_h^k, \tag{24a}$$

$$\frac{\mu_0}{2}\left(\frac{\boldsymbol{H}_h^{n+3/2} - \boldsymbol{H}_h^{n+1/2}}{\tau} + \frac{\boldsymbol{H}_h^{n-1/2} - \boldsymbol{H}_h^{n-3/2}}{\tau}, \boldsymbol{\phi}\right) + \mathcal{B}_h^E\left(\frac{\boldsymbol{E}_h^{n+1} + \boldsymbol{E}_h^{n-1}}{2}, \boldsymbol{\phi}\right) = 0,\ \forall \boldsymbol{\phi} \in V_h^k. \tag{24b}$$

Taking $\boldsymbol{\phi} = \frac{\boldsymbol{E}_h^{n+1} + \boldsymbol{E}_h^{n-1}}{2}$ in (24a) and $\boldsymbol{\phi} = \frac{\boldsymbol{H}_h^{n+1/2} + \boldsymbol{H}_h^{n-1/2}}{2}$ in (24b), summing up the results and using the relation (19), we obtain

$$\left(\frac{\boldsymbol{D}_h^{n+1} - \boldsymbol{D}_h^{n-1}}{2}, \frac{\boldsymbol{E}_h^{n+1} + \boldsymbol{E}_h^{n-1}}{2}\right) - \frac{\mu_0}{2}\int_\Omega\left(\left|\boldsymbol{H}_h^{n+1/2}\right|^2 - \left|\boldsymbol{H}_h^{n-1/2}\right|^2\right) d\Omega \tag{25}$$

$$+\mu_0\Big(\frac{\boldsymbol{H}_h^{n+3/2}+\boldsymbol{H}_h^{n+1/2}}{2}-\frac{\boldsymbol{H}_h^{n-1/2}+\boldsymbol{H}_h^{n-3/2}}{2},\frac{\boldsymbol{H}_h^{n+1/2}+\boldsymbol{H}_h^{n-1/2}}{2}\Big)=0.$$

On the other hand, by equation (8c), we have

$$\Big(\boldsymbol{D}_h^{n+1}-\boldsymbol{D}_h^{n-1},\frac{\boldsymbol{E}_h^{n+1}+\boldsymbol{E}_h^{n-1}}{2}\Big)=\frac{\epsilon_0\epsilon_\infty}{2}\left(\left|\boldsymbol{E}_h^{n+1}\right|^2+\left|\boldsymbol{E}_h^{n}\right|^2\right)-\frac{\epsilon_0\epsilon_\infty}{2}\left(\left|\boldsymbol{E}_h^{n}\right|^2+\left|\boldsymbol{E}_h^{n-1}\right|^2\right) \tag{26}$$

$$+\epsilon_0\Big(\boldsymbol{P}_h^{n+1}-\boldsymbol{P}_h^{n-1},\frac{\boldsymbol{E}_h^{n+1}+\boldsymbol{E}_h^{n-1}}{2}\Big)+\epsilon_0 a\Big(\boldsymbol{Y}_h^{n+1}-\boldsymbol{Y}_h^{n-1},\frac{\boldsymbol{E}_h^{n+1}+\boldsymbol{E}_h^{n-1}}{2}\Big).$$

For the Lorentz term, from (8f), we get

$$\Big(\boldsymbol{P}_h^{n+1}-\boldsymbol{P}_h^{n-1},\frac{\boldsymbol{E}_h^{n+1}+\boldsymbol{E}_h^{n-1}}{2}\Big)=\frac{1}{\omega_p^2}\int_\Omega\Big(\Big|\frac{\boldsymbol{P}_h^{n+1}-\boldsymbol{P}_h^{n}}{\tau}\Big|^2-\Big|\frac{\boldsymbol{P}_h^{n}-\boldsymbol{P}_h^{n-1}}{\tau}\Big|^2 \tag{27}$$

$$+\frac{\omega_0^2}{2}\Big(\left|\boldsymbol{P}_h^{n+1}\right|^2+\left|\boldsymbol{P}_h^{n}\right|^2\Big)-\frac{\omega_0^2}{2}\Big(\left|\boldsymbol{P}_h^{n}\right|^2+\left|\boldsymbol{P}_h^{n-1}\right|^2\Big)\Big)d\Omega+\frac{2\gamma\tau}{\omega_p^2}\int_\Omega\Big|\frac{\boldsymbol{P}_h^{n+1}-\boldsymbol{P}_h^{n-1}}{2\tau}\Big|^2d\Omega.$$

For the nonlinear Kerr term, using (8d) and the property of the interpolation operator $\mathcal{I}_h$, given by Lemma 1 in [22], we have,

$$\begin{aligned}&\Big(\boldsymbol{Y}_h^{n+1}-\boldsymbol{Y}_h^{n-1},\frac{\boldsymbol{E}_h^{n+1}+\boldsymbol{E}_h^{n-1}}{2}\Big) \\ =&\int_\Omega\mathcal{I}_h\Big(\left|\boldsymbol{E}_h^{n}\right|^2(\boldsymbol{E}_h^{n+1}-\boldsymbol{E}_h^{n-1})+2\left(\boldsymbol{E}_h^{n}\cdot(\boldsymbol{E}_h^{n+1}-\boldsymbol{E}_h^{n-1})\right)\boldsymbol{E}_h^{n},\frac{\boldsymbol{E}_h^{n+1}+\boldsymbol{E}_h^{n-1}}{2}\Big)d\Omega \\ =&\frac{1}{2}\int_\Omega\mathcal{I}_h\left(\left|\boldsymbol{E}_h^{n+1}\right|^2\left|\boldsymbol{E}_h^{n}\right|^2-\left|\boldsymbol{E}_h^{n}\right|^2\left|\boldsymbol{E}_h^{n-1}\right|^2+2\left(\boldsymbol{E}_h^{n+1}\cdot\boldsymbol{E}_h^{n}\right)^2-2\left(\boldsymbol{E}_h^{n}\cdot\boldsymbol{E}_h^{n-1}\right)^2\right)d\Omega.\end{aligned} \tag{28}$$

Combining (25)-(28), we reach the discrete energy law (21), with $\mathcal{E}_{h,LK}^{n+1/2}$ given in (22).

Step 2: non-negativeness of $\mathcal{E}_{h,LK}^{n+1/2}$ and the associated time step condition. Though the discrete energy law (21) holds for the numerical solution, the quantity $\mathcal{E}_{h,LK}^{n+1/2}$ may not be non-negative unless some condition is further imposed on the time step size τ as one would expect. Next we will derive such condition on τ. Applying two time steps to (8b), taking $\boldsymbol{\phi}=\boldsymbol{H}_h^{n+3/2}+\boldsymbol{H}_h^{n+1/2}$ and using (20) with $\vartheta=\sqrt{\frac{\mu_0}{\epsilon_0\epsilon_\infty}}$, as well as the triangle inequality, we have

$$\begin{aligned}&\mu_0\left(\boldsymbol{H}_h^{n+3/2}+\boldsymbol{H}_h^{n+1/2},\boldsymbol{H}_h^{n+1/2}+\boldsymbol{H}_h^{n-1/2}\right)\geq\mu_0\left\|\boldsymbol{H}_h^{n+3/2}+\boldsymbol{H}_h^{n+1/2}\right\|^2 \\ &-\frac{C_\star\tau}{2h}\Big(\sqrt{\frac{\epsilon_0\epsilon_\infty}{\mu_0}}\left\|\boldsymbol{E}_h^{n+1}+\boldsymbol{E}_h^{n}\right\|^2+\sqrt{\frac{\mu_0}{\epsilon_0\epsilon_\infty}}\left\|\boldsymbol{H}_h^{n+3/2}+\boldsymbol{H}_h^{n+1/2}\right\|^2\Big) \\ &\geq\mu_0\Big(1-\frac{\lambda}{2}\Big)\left\|\boldsymbol{H}_h^{n+3/2}+\boldsymbol{H}_h^{n+1/2}\right\|^2-\epsilon_0\epsilon_\infty\lambda\left(\left\|\boldsymbol{E}_h^{n+1}\right\|^2+\left\|\boldsymbol{E}_h^{n}\right\|^2\right).\end{aligned} \tag{29}$$

Here we write $v_\infty=1/\sqrt{\epsilon_0\epsilon_\infty\mu_0}$ and $\lambda=\frac{C_\star v_\infty\tau}{h}$.

Similarly, with $\boldsymbol{H}_h^{n+3/2}-\boldsymbol{H}_h^{n+1/2}=\boldsymbol{H}_h^{n+3/2}+\boldsymbol{H}_h^{n+1/2}-2\boldsymbol{H}_h^{n+1/2}$, we take $\boldsymbol{\phi}=\boldsymbol{H}_h^{n+3/2}+3\boldsymbol{H}_h^{n+1/2}$ in (8b) and apply (20) with $\vartheta=\sqrt{\frac{\mu_0}{\epsilon_0\epsilon_\infty}}$, and get

$$\begin{aligned}4\mu_0\left\|\boldsymbol{H}_h^{n+1/2}\right\|^2\leq&\mu_0\left\|\boldsymbol{H}_h^{n+3/2}+\boldsymbol{H}_h^{n+1/2}\right\|^2+\frac{C_\star\tau}{2h}\sqrt{\frac{\epsilon_0\epsilon_\infty}{\mu_0}}\left\|\boldsymbol{E}_h^{n+1}\right\|^2 \\ &+\frac{C_\star\tau}{h}\sqrt{\frac{\mu_0}{\epsilon_0\epsilon_\infty}}\left\|\boldsymbol{H}_h^{n+3/2}+\boldsymbol{H}_h^{n+1/2}\right\|^2+4\frac{C_\star\tau}{h}\sqrt{\frac{\mu_0}{\epsilon_0\epsilon_\infty}}\left\|\boldsymbol{H}_h^{n+1/2}\right\|^2.\end{aligned} \tag{30}$$

This further leads to

$$\left\|\boldsymbol{H}_h^{n+1/2}\right\|^2\leq\frac{1+\lambda}{4(1-\lambda)}\left\|\boldsymbol{H}_h^{n+3/2}+\boldsymbol{H}_h^{n+1/2}\right\|^2+\frac{\epsilon_0\epsilon_\infty}{\mu_0}\frac{\lambda}{8(1-\lambda)}\left\|\boldsymbol{E}_h^{n+1}\right\|^2, \tag{31}$$

provided that

$$1-\lambda>0. \tag{32}$$

Combining (29)-(31), we come to

$$\mu_0\left(\boldsymbol{H}_h^{n+3/2}+\boldsymbol{H}_h^{n+1/2},\boldsymbol{H}_h^{n+1/2}+\boldsymbol{H}_h^{n-1/2}\right)-2\mu_0\left\|\boldsymbol{H}_h^{n+1/2}\right\|^2+\epsilon_0\epsilon_\infty\left(\left\|\boldsymbol{E}_h^{n+1}\right\|^2+\left\|\boldsymbol{E}_h^{n}\right\|^2\right)$$
$$\geq\frac{\mu_0}{2}\left(2-\lambda-\frac{1+\lambda}{1-\lambda}\right)\left\|\boldsymbol{H}_h^{n+3/2}+\boldsymbol{H}_h^{n+1/2}\right\|^2$$
$$+\epsilon_0\epsilon_\infty\left(1-\lambda-\frac{\lambda/4}{1-\lambda}\right)\left\|\boldsymbol{E}_h^{n+1}\right\|^2+\epsilon_0\epsilon_\infty\left(1-\lambda\right)\left\|\boldsymbol{E}_h^{n}\right\|^2\geq 0,$$

with the last inequality ensured by the following conditions on λ along with (32),

$$2-\lambda-\frac{1+\lambda}{1-\lambda}\geq 0,\quad 1-\lambda-\frac{\lambda/4}{1-\lambda}\geq 0. \tag{33}$$

These conditions can be simplified as $\lambda\leq 2-\sqrt{3}$, hence $v_\infty\tau/h\leq(2-\sqrt{3})/C_\star$.

In addition, by using a positivity preserving property of $\mathcal{I}_h$ (see Lemma 2 in [22]), namely

$$\int_\Omega \mathcal{I}_h f\,d\Omega\geq 0,\quad \forall\, f\in W_h(\Omega)\ \text{and}\ f\geq 0, \tag{34}$$

we know that the term in (22) associated with the nonlinear Kerr effect is always non-negative, i.e. $\int_\Omega \mathcal{I}_h\left(\left|\boldsymbol{E}_h^{n+1}\right|^2\left|\boldsymbol{E}_h^{n}\right|^2+2\left(\boldsymbol{E}_h^{n+1}\cdot\boldsymbol{E}_h^{n}\right)^2\right)d\Omega\geq 0$. Finally, one concludes the discrete energy $\mathcal{E}_{h,LK}^{n+1/2}$ is non-negative under the time step condition (23). □

Remark 2. For the nonlinear energy stable methods proposed in [5] (1D) and [22] (multi-D) based on the first order form of the model as well as for the nonlinear energy stable methods in [23] based on the mixed order form of model, when the numerical fluxes are alternating (11) or the generalized version (10), and when the nonlinearity parameter $\theta\in[0,\frac{3}{4}]$ (including the Lorentz-Kerr case with $\theta=0$), an energy law as in (3) can be rigorously established with respect to a carefully defined discrete energy, which is non-negative under a milder CFL condition, $v_\infty\frac{\tau}{h}\leq\frac{2}{C_\star}$. (This was shown in [5] in 1D, and can be shown for the methods in [22,23] by using (20) and setting the medium-dependent constant ϑ as the wave impedance $\vartheta=\sqrt{\mu_0/(\epsilon_0\epsilon_\infty)}$. The analysis in [22,23] adopted a medium-independent ϑ and thus led to a less balanced time step condition.) Following our numerical analysis, the methods here require a smaller CFL condition, with a reduced coefficient $2-\sqrt{3}$, for a more ambitious goal of simultaneously achieving a provable energy law and rendering linear methods free of any nonlinear algebraic iterations. On the other hand, the numerical evidence in Section 4.1.1 shows that the actual time steps allowed by our proposed methods and those by the nonlinear methods in [5,22] are likely comparable.

Remark 3. For the general Lorentz-Kerr-Raman model (i.e. $\theta\neq 0$), we are unable to identify a discrete energy for the proposed methods, with respect to which a provable energy law can be established. Motivated by the theoretical result for the special Lorentz-Kerr case with its discrete energy $\mathcal{E}_{h,LK}^{n+1/2}$ in (22), we define a discrete quasi-energy $\mathcal{E}_{h,LKR}^{n+1/2}$ at $t=t^{n+\frac{1}{2}}$ for the full model,

$$\mathcal{E}_{h,LKR}^{n+1/2}=\int_\Omega\Bigg(\mu_0\frac{\boldsymbol{H}_h^{n+3/2}+\boldsymbol{H}_h^{n+1/2}}{2}\cdot\frac{\boldsymbol{H}_h^{n+1/2}+\boldsymbol{H}_h^{n-1/2}}{2}-\frac{\mu_0}{2}|\boldsymbol{H}_h^{n+1/2}|^2 \tag{35}$$
$$+\frac{\epsilon_0\epsilon_\infty}{2}\frac{\left|\boldsymbol{E}_h^{n+1}\right|^2+\left|\boldsymbol{E}_h^{n}\right|^2}{2}+\frac{\epsilon_0}{2\omega_p^2}\left|\frac{\boldsymbol{P}_h^{n+1}-\boldsymbol{P}_h^{n}}{\tau}\right|^2+\frac{\epsilon_0\omega_0^2}{2\omega_p^2}\frac{\left|\boldsymbol{P}_h^{n+1}\right|^2+\left|\boldsymbol{P}_h^{n}\right|^2}{2}$$
$$+\frac{\epsilon_0 a(1-\theta)}{4}\mathcal{I}_h\left(\left|\boldsymbol{E}_h^{n+1}\right|^2\left|\boldsymbol{E}_h^{n}\right|^2+2\left(\boldsymbol{E}_h^{n+1}\cdot\boldsymbol{E}_h^{n}\right)^2\right)+\frac{\epsilon_0 a\theta}{4\omega_v^2}\left(\frac{Q_h^{n+1}-Q_h^{n}}{\tau}\right)^2$$
$$+\frac{\epsilon_0 a\theta}{2}\mathcal{I}_h\left(\frac{Q_h^{n+1}+Q_h^{n}}{2}\boldsymbol{E}_h^{n+1}\cdot\boldsymbol{E}_h^{n}\right)+\frac{\epsilon_0 a\theta}{4}\frac{\left(Q_h^{n+1}\right)^2+\left(Q_h^{n}\right)^2}{2}\Bigg)d\Omega.$$

Apparently $\mathcal{E}_{h,LKR}^{n+1/2}$ is a second order discretization of $\mathcal{E}(t)$ in (4). With a direct calculation, we have

$$\frac{a(1-\theta)}{4}\left(\left|\boldsymbol{E}_h^{n+1}\right|^2\left|\boldsymbol{E}_h^{n}\right|^2+2\left(\boldsymbol{E}_h^{n+1}\cdot\boldsymbol{E}_h^{n}\right)^2\right)+\frac{a\theta}{4}\frac{\left(Q_h^{n+1}\right)^2+\left(Q_h^{n}\right)^2}{2}+\frac{a\theta}{2}\frac{Q_h^{n+1}+Q_h^{n}}{2}\boldsymbol{E}_h^{n+1}\cdot\boldsymbol{E}_h^{n}$$
$$\geq\frac{3a(1-\theta)}{4}\left(\boldsymbol{E}_h^{n+1}\cdot\boldsymbol{E}_h^{n}\right)^2+\frac{a\theta}{4}\frac{\left(Q_h^{n+1}\right)^2+\left(Q_h^{n}\right)^2}{2}+\frac{a\theta}{2}\frac{Q_h^{n+1}+Q_h^{n}}{2}\boldsymbol{E}_h^{n+1}\cdot\boldsymbol{E}_h^{n}$$
$$=\frac{a(3-4\theta)}{4}\left(\boldsymbol{E}_h^{n+1}\cdot\boldsymbol{E}_h^{n}\right)^2+\frac{a\theta}{8}\left(\left(Q_h^{n+1}+\boldsymbol{E}_h^{n+1}\cdot\boldsymbol{E}_h^{n}\right)^2+\left(Q_h^{n}+\boldsymbol{E}_h^{n}\cdot\boldsymbol{E}_h^{n}\right)^2\right)\geq 0,$$

therefore $\mathcal{E}_{h,LKR}^{n+1/2}\geq 0$ as long as $\theta\in[0,\frac{3}{4}]$ just as required in the continuous case, and under the same time step condition (23). Again, we here use the positivity preserving property of $\mathcal{I}_h$ in (34). Though no energy law is proved with respect to this discrete quasi-

energy $\mathcal{E}_{h,LKR}^{n+1/2}$, it is still meaningful to numerically monitor the time evolution of this non-negative quality, to get some supporting evidence that the linear methods are stable for the full Lorentz-Kerr-Raman model as time progresses. One such study can be found in Section 4.1.2, see Fig. 5.

3.3. Error estimates

This section is devoted to the *a priori* error estimates for the proposed methods applied to the Lorentz-Kerr model (with $\theta = 0$) up to a given time $T > 0$, when the exact solutions are sufficiently smooth. Particularly, in Section 3.3.1, a master error relation will be derived first. Based on this foundational relation, we proceed to establish the error estimates for the linear model (with $a = 0$ in the absence of the Kerr effect) in Section 3.3.2 under a similar type of time step condition (23) for the discrete energy law, before we present the error estimates for the general Lorentz-Kerr model in Section 3.3.3 under a more stringent time step condition, along with some constraint on the polynomial degree k. Throughout, it is assumed $h, \tau \le 1$.

Let us begin with some shorthand notation

$$\delta_{\tau^2}^n u = \frac{u^{n+1} - 2u^n + u^{n-1}}{\tau^2}, \quad \delta_{2\tau}^n u = \frac{u^{n+1} - u^{n-1}}{2\tau}, \quad \overline{\overline{u^n}} = \frac{u^{n+1} + u^{n-1}}{2},$$
$$\delta_{\tau}^s u = \frac{u^{s+1/2} - u^{s-1/2}}{\tau}, \quad \overline{u^{s+1/2}} = \frac{u^{s+1} + u^s}{2}, \quad s = n, n + \frac{1}{2}.$$

With $v^n = v(\cdot, t^n)$, we further define $e_v^n = v^n - v_h^n = \eta_v^n - \xi_v^n$, with $\eta_v^n = v^n - \mathcal{R}_{v,h} v^n$ and $\xi_v^n = v_h^n - \mathcal{R}_{v,h} v^n$ for $v = \boldsymbol{H}, \boldsymbol{E}, \boldsymbol{P}$. Each $\mathcal{R}_{v,h}$ is a projection operator onto V_h^k. Specifically, we take $\mathcal{R}_{\boldsymbol{P},h} = \Pi_h^{0,0,0}$ as the standard L^2 projection. With the alternating I numerical fluxes, we take $\mathcal{R}_{\boldsymbol{H},h} = \Pi_h^{+,+,+}$, $\mathcal{R}_{\boldsymbol{E},h} = \Pi_h^{-,-,-}$, while with the alternating II numerical fluxes, we take $\mathcal{R}_{\boldsymbol{H},h} = \Pi_h^{-,-,-}$, $\mathcal{R}_{\boldsymbol{E},h} = \Pi_h^{+,+,+}$. These are the 3D version of the Radau projections as in Appendix A.1 of [22] (also see [10,20]). The main approximation properties of the discrete V_h^k through these projection operators and the interpolation operator $\mathcal{I}_h$ are summarized next.

Lemma 2 *(Approximation properties of V_h^k). Let Π_h be any of the operators $\mathcal{I}_h$, $\Pi_h^{0,0,0}$, $\Pi_h^{\pm,\pm,\pm}$. There exists some constant $C_k > 0$ and $C_w > 0$, such that*

$$\|w - \Pi_h w\| \le C_k C_w h^{k+1}, \quad \|w - \Pi_h w\|_\infty \le C_k C_w h^{k+1}, \tag{36a}$$
$$\|\Pi_h^{\pm,\pm,\pm} w\|_\infty \le C_k C_w, \tag{36b}$$
$$\|\delta_{2\tau}^n (w - \Pi_h w)\| + \|\delta_{\tau^2}^n (w - \Pi_h w)\| + \|\delta_{\tau}^n (w - \Pi_h w)\| \le C_k C_w h^{k+1}, \tag{36c}$$

for functions w from certain Sobolev spaces and with a constant C_w depending on some Sobolev norm of w.[2] *Here n is any relevant integer between 1 and $N_t = T/\tau$.*

Particularly, the results in (36a)-(36b) become standard in numerical analysis for DG methods, and they can be established following classical arguments as in [9], while the result in (36c) follows the Taylor's theorem and the commuting property $\partial_t \Pi_h = \Pi_h \partial_t$. Unless specified otherwise, throughout this section, $C_\dagger$ represents some positive constant that only depends on $\dagger$. Some examples include C_k, C_w, C_ρ etc. Moreover, C denotes a generic positive constant. This constant is independent of n, h, τ, and may depend on the polynomial degree k, the time T, some model parameters, and/or some norms of the exact solutions and their derivatives. Both C and $C_\dagger$ can take different values at different occurrences. The next lemma is a direct result of the Taylor's theorem.

Lemma 3 *(Local truncation errors). Related to the temporal discretizations of the proposed methods, we define the local truncation errors as below,*

$$\boldsymbol{\tau}_{\boldsymbol{D}}^{n+1/2} := \delta_\tau^{n+1/2} \boldsymbol{D} - \partial_t \boldsymbol{D}^{n+1/2}, \tag{37a}$$
$$\boldsymbol{\tau}_{\boldsymbol{H}}^{n+1} := \delta_\tau^{n+1} \boldsymbol{H} - \partial_t \boldsymbol{H}^{n+1}, \tag{37b}$$
$$\boldsymbol{\tau}_{\boldsymbol{P}}^{n} := \delta_{\tau^2}^n \boldsymbol{P} + \gamma \delta_{2\tau}^n \boldsymbol{P} + \omega_0^2 \overline{\overline{\boldsymbol{P}^n}} - \omega_p^2 \overline{\overline{\boldsymbol{E}^n}}, \tag{37c}$$
$$\boldsymbol{\tau}_{\boldsymbol{Y}}^{n} := (|\boldsymbol{E}^n|^2 \mathbb{I} + 2\boldsymbol{E}^n \boldsymbol{E}^{n\top}) \delta_{2\tau}^n \boldsymbol{E}) - \delta_{2\tau}^n (|\boldsymbol{E}|^2 \boldsymbol{E}). \tag{37d}$$

The following bounds hold for the exact solutions $\boldsymbol{D}, \boldsymbol{H}, \boldsymbol{P}, \boldsymbol{E}$, with some constant $C > 0$ and for any relevant n between 1 and $N_t = T/\tau$,

$$\|\boldsymbol{\tau}_{\boldsymbol{D}}^{n+1/2}\|, \|\boldsymbol{\tau}_{\boldsymbol{H}}^{n+1}\|, \|\boldsymbol{\tau}_{\boldsymbol{P}}^{n}\|, \|\boldsymbol{\tau}_{\boldsymbol{Y}}^{n}\| \le C\tau^2. \tag{38}$$

[2] As an example, $\|w - \Pi_h^{0,0,0} w\| \le C_k h^{k+1} \|w\|_{H^{k+1}(\Omega)}, \quad \forall w \in H^{k+1}(\Omega)$.

3.3.1. The master error relation

First, we establish the master error relation, the foundation of the error analysis. The proof is given Appendix A, following some similar derivation as in **Step 1** of Theorem 2.

Theorem 3 *(Error analysis: the master error relation). With $\theta = 0$ and periodic boundary conditions, the following error relation holds for the numerical solution of the proposed methods (8)-(9) with numerical fluxes (10),*

$$\widehat{\mathcal{E}}_h^{n+1/2} - \widehat{\mathcal{E}}_h^{n-1/2} + a\tau\mathcal{N}^n\big(\overline{\overline{\xi_{\boldsymbol{E}}^n}}\big) = \tau S_0^n, \tag{39}$$

where

$$\begin{aligned}\widehat{\mathcal{E}}_h^{n+1/2} :=& \mu_0 \int_\Omega \overline{\xi_{\boldsymbol{H}}^{n+1}} \cdot \overline{\xi_{\boldsymbol{H}}^{n}} d\Omega - \frac{\mu_0}{2}\|\xi_{\boldsymbol{H}}^{n+1/2}\|^2 + \frac{\epsilon_0\epsilon_\infty}{4}(\|\xi_{\boldsymbol{E}}^{n+1}\|^2 + \|\xi_{\boldsymbol{E}}^{n}\|^2) \\ &+ \frac{\epsilon_0}{2\omega_p^2}\|\delta_\tau^{n+1/2}\xi_{\boldsymbol{P}}\|^2 + \frac{\epsilon_0\omega_0^2}{4\omega_p^2}(\|\xi_{\boldsymbol{P}}^{n+1}\|^2 + \|\xi_{\boldsymbol{P}}^{n}\|^2),\end{aligned} \tag{40}$$

$$S_0^n := -\frac{\epsilon_0\gamma}{\omega_p^2}\|\delta_{2\tau}^n\xi_{\boldsymbol{P}}\|^2 + \mathcal{K}^n\big(\overline{\overline{\xi_{\boldsymbol{E}}^n}}\big) + \mathcal{M}^n\big(\overline{\xi_{\boldsymbol{H}}^n}\big) + \mathcal{L}^n\big(\overline{\overline{\xi_{\boldsymbol{E}}^n}}\big) - \mathcal{Q}^n\big(\delta_{2\tau}^n\xi_{\boldsymbol{P}}\big), \tag{41}$$

with

$$\mathcal{K}^n(\boldsymbol{\phi}) := \mathcal{B}_h^H(\overline{\eta_{\boldsymbol{H}}^n}, \boldsymbol{\phi}) - (\overline{\boldsymbol{\tau}_{\boldsymbol{D}}^n}, \boldsymbol{\phi}), \tag{42a}$$

$$\mathcal{M}^n(\boldsymbol{\phi}) := \frac{\mu_0}{2}(\delta_\tau^{n+1}\eta_{\boldsymbol{H}} + \delta_\tau^{n-1}\eta_{\boldsymbol{H}}, \boldsymbol{\phi}) + \mathcal{B}_h^E(\overline{\overline{\eta_{\boldsymbol{E}}^n}}, \boldsymbol{\phi}) - \mu_0(\overline{\overline{\boldsymbol{\tau}_{\boldsymbol{H}}^n}}, \boldsymbol{\phi}), \tag{42b}$$

$$\mathcal{L}^n(\boldsymbol{\phi}) := \epsilon_0(\epsilon_\infty\delta_{2\tau}^n\eta_{\boldsymbol{E}} + \delta_{2\tau}^n\eta_{\boldsymbol{P}}, \boldsymbol{\phi}), \qquad \mathcal{N}^n(\boldsymbol{\phi}) := \epsilon_0\big(\delta_{2\tau}^n(\boldsymbol{Y}_h - |\boldsymbol{E}|^2\boldsymbol{E})\big), \boldsymbol{\phi}\big), \tag{42c}$$

$$\mathcal{Q}^n(\boldsymbol{\phi}) := \epsilon_0\omega_p^{-2}(\delta_{\tau^2}^n\eta_{\boldsymbol{P}} + \gamma\delta_{2\tau}^n\eta_{\boldsymbol{P}} + \omega_0^2\overline{\overline{\eta_{\boldsymbol{P}}^n}} - \omega_p^2\overline{\overline{\eta_{\boldsymbol{E}}^n}} - \boldsymbol{\tau}_{\boldsymbol{P}}^n, \boldsymbol{\phi}). \tag{42d}$$

3.3.2. Error estimates for the linear model with $a = 0$

In this subsection, we will focus on the error analysis for the linear model with $a = 0$ in the absence of the Kerr effect. Optimal error estimates will be established under a similar type of time step condition (23) for the provable discrete energy law. Some details in the proof will be further used to analyze the general Lorentz-Kerr model with $a > 0$ in the next subsection.

Lemma 4. *There holds*

$$S_0^n \le C(h^{2k+2} + \tau^4) + C(h^{k+1} + \tau^2)(\|\xi_{\boldsymbol{E}}^{n+1}\| + \|\xi_{\boldsymbol{E}}^{n-1}\| + \|\overline{\xi_{\boldsymbol{H}}^n}\|). \tag{43}$$

Proof. Based on (the 3D analogue of) the super-convergence results in [10,20] for Q^k-type DG approximations with any alternating numerical flux pair in (11) on Cartesian meshes, one gets

$$|\mathcal{B}_h^H(\overline{\eta_{\boldsymbol{H}}^n}, \boldsymbol{\phi})| \le Ch^{k+1}\|\boldsymbol{\phi}\|, \qquad |\mathcal{B}_h^E(\overline{\overline{\eta_{\boldsymbol{E}}^n}}, \boldsymbol{\phi})| \le Ch^{k+1}\|\boldsymbol{\phi}\|, \quad \forall \boldsymbol{\phi} \in V_h^k. \tag{44}$$

Using the approximation property in Lemma 2, the bounds of local truncation errors in Lemma 3, Cauchy-Schwartz inequality, we have

$$S_0^n \le -\frac{\epsilon_0\gamma}{\omega_p^2}\|\delta_{2\tau}^n\xi_{\boldsymbol{P}}\|^2 + C(h^{k+1} + \tau^2)(\|\xi_{\boldsymbol{E}}^{n+1}\| + \|\xi_{\boldsymbol{E}}^{n-1}\| + \|\overline{\xi_{\boldsymbol{H}}^n}\| + \|\delta_{2\tau}^n\xi_{\boldsymbol{P}}\|). \tag{45}$$

One can reach the estimate (43) after applying a simple inequality: $-\alpha x^2 + \beta x \le \beta^2/(4\alpha)$ with any $\alpha > 0$. □

For error estimates, $\widehat{\mathcal{E}}_h^{n+1/2}$ needs to be non-negative in an *approximately stronger sense*, as specified and established in the next proposition. The proof is given in Appendix B, by following some similar but refined analysis as in Step 2 of Theorem 2.

Proposition 1. *For any pre-set constant $\rho_{err} \in (0, 1 - \sqrt{2/3})$, there holds*

$$\widehat{\mathcal{E}_{h,\#}}^{n+1/2} \le \widehat{\mathcal{E}}_h^{n+1/2} + C_{\rho_{err}}C\tau^2(h^{2k+2} + \tau^4), \tag{46}$$

under a time step condition

$$\frac{v_\infty\tau}{h} \le r_{\rho_{err}}\frac{2 - \sqrt{3}}{C_\star}. \tag{47}$$

Here

$$r_{\rho_{err}} = \frac{2(1-\rho_{err}) - \sqrt{(1-\rho_{err})^2+2}}{2-\sqrt{3}} \in (0,1), \tag{48}$$

$$\widehat{\mathcal{E}_{h,\#}}^{n+1/2} = \rho_{err}\left(\frac{\mu_0}{2}\|\xi_{\boldsymbol{H}}^{n+1}\|^2 + \frac{\epsilon_0\epsilon_\infty}{4}(\|\xi_{\boldsymbol{E}}^{n+1}\|^2 + \|\xi_{\boldsymbol{E}}^{n}\|^2)\right) + \frac{\epsilon_0\omega_0^2}{4\omega_p^2}(\|\xi_{\boldsymbol{P}}^{n+1}\|^2 + \|\xi_{\boldsymbol{P}}^{n}\|^2). \tag{49}$$

Theorem 4 *(Error estimates for the linear model: $a=0$). Let $\rho_{err} \in (0, 1-\sqrt{2/3})$ be any pre-chosen constant and assume $\tau \le 1/2$. With $\theta = a = 0$ and periodic boundary conditions, the numerical solutions of the proposed methods (8)-(9) with numerical fluxes (10) have the following error estimates under the time step condition (47).*

- *With $\widehat{\mathcal{E}_{h,\#}}^{n+1/2}$ defined in (49), we have for $n: 1 < n < N_t$,*

$$\widehat{\mathcal{E}_{h,\#}}^{n+1/2} \le C_{\rho_{err}} C(h^{2k+2} + \tau^4) + 3\widehat{\mathcal{E}_h}^{3/2}. \tag{50}$$

- *If, in addition, $|\widehat{\mathcal{E}_h}^{3/2}| \le C_{\rho_{err}} C(h^{2k+2} + \tau^4)$, then for $n: 1 < n < N_t$,*

$$\|e_{\boldsymbol{E}}^n\|, \|\overline{e_{\boldsymbol{H}}^n}\|, \|e_{\boldsymbol{H}}^{n+1/2}\|, \|e_{\boldsymbol{P}}^n\| \le C_{\rho_{err}} C(h^{k+1} + \tau^2). \tag{51}$$

Proof. With a simple application of Cauchy-Schwartz inequality, one has

$$S_0^n \le C_{\rho_{err}} C(h^{2k+2} + \tau^4) + \widehat{\mathcal{E}_{h,\#}}^{n+1/2} + \widehat{\mathcal{E}_{h,\#}}^{n-1/2}.$$

Now we sum up the master error relation (39) with $a=0$, using $\tau n \le T$ and the inequality above, and obtain

$$\begin{aligned}\widehat{\mathcal{E}_h}^{n+1/2} &= \widehat{\mathcal{E}_h}^{3/2} + \tau\sum_{m=2}^{n} S_0^m \\ &\le C_{\rho_{err}} C(h^{2k+2} + \tau^4) + \widehat{\mathcal{E}_h}^{3/2} + \tau\sum_{m=2}^{n}\left(\widehat{\mathcal{E}_{h,\#}}^{m+1/2} + \widehat{\mathcal{E}_{h,\#}}^{m-1/2}\right).\end{aligned} \tag{52}$$

This leads to, under the assumption $\tau \le 1/2$,

$$\begin{aligned}\widehat{\mathcal{E}_{h,\#}}^{n+1/2} &\le C_{\rho_{err}} C(h^{2k+2} + \tau^4) + 2\widehat{\mathcal{E}_h}^{3/2} + 2\tau\widehat{\mathcal{E}_{h,\#}}^{3/2} + 4\tau\sum_{m=2}^{n-1}\widehat{\mathcal{E}_{h,\#}}^{m+1/2}, \\ &\le C_{\rho_{err}} C(h^{2k+2} + \tau^4) + 3\widehat{\mathcal{E}_h}^{3/2} + 4\tau\sum_{m=2}^{n-1}\widehat{\mathcal{E}_{h,\#}}^{m+1/2},\end{aligned} \tag{53}$$

hence the first estimate in (50) following a discrete Gronwall inequality. Furthermore, if $|\widehat{\mathcal{E}_h}^{3/2}| \le C_{\rho_{err}} C(h^{2k+2} + \tau^4)$, then $\widehat{\mathcal{E}_{h,\#}}^{n+1/2} \le C_{\rho,\rho_{err}} C(h^{2k+2} + \tau^4)$, for $n > 1$. We also obtain $\|\xi_{\boldsymbol{H}}^{n+1/2}\| \le C_{\rho_{err}} C(h^{k+1} + \tau^2)$ by using the bound in (B.6). Finally, using the triangle inequality $\|e_v\| \le \|\xi_v\| + \|\eta_v\|$ and the approximation properties in Lemma 2, we can conclude the second estimate in (51). □

Remark 4. The summation in (51) is from $m=2$, as $\widehat{\mathcal{E}_h}^{1/2}$ is undefined. With some careful estimate for the initial steps, one can further verify the assumption on the size of $\widehat{\mathcal{E}_h}^{3/2}$. This will not be discussed due to the technical involvement.

Remark 5. The error estimates in Theorem 4 are *optimal* with respect to the temporal local truncation errors and the approximation properties of the discrete space V_h^k in space. Note the factor ρ_{err} in (48) satisfies $\lim_{\rho_{err}\to 0} r_{\rho_{err}} = 1$, indicating that the error estimates hold under nearly the same (but slightly smaller) time step condition (23) as for the discrete energy law in Theorem 2.

3.3.3. *Error estimates for the Lorentz-Kerr model with $a > 0$*

We now turn to the error analysis of the proposed methods for the Lorentz-Kerr model with $a > 0$. The key is to estimate the contribution of $\mathcal{N}^n(\overline{\overline{\xi_{\boldsymbol{E}}^n}})$ in the master error relation (39).

To prepare, we introduce an auxiliary field $\boldsymbol{A}_h^n$,

$$\boldsymbol{A}_h^n = \boldsymbol{E}^n - \eta_{\boldsymbol{E}}^n = \mathcal{R}_{\boldsymbol{E},h}\boldsymbol{E}^n \tag{54}$$

associated with the electric field. This enables us to write $\boldsymbol{E}_h^n = \boldsymbol{A}_h^n + \xi_{\boldsymbol{E}}^n$. Based on the approximation property of the projection operator $\mathcal{R}_{\boldsymbol{E},h}$, $\partial_t \boldsymbol{A}_h^n = \mathcal{R}_{\boldsymbol{E},h}(\partial_t \boldsymbol{E}^n)$ and Taylor's theorem, one can get the following for the sufficiently regular exact solution $\boldsymbol{E}$.

Lemma 5. *There exists a constant C, such that for any relevant index n between 0 and N_t, there hold*

$$\|\boldsymbol{A}_h^n\|_\infty \le C, \quad \|\delta_\tau^{n+1/2}\boldsymbol{A}_h\|_\infty \le C, \quad \|\delta_{2\tau}^n \boldsymbol{A}_h\|_\infty \le C, \quad \|\delta_{2\tau}^n \boldsymbol{E}\|_\infty \le C. \tag{55}$$

We also recall some properties of the interpolation operators $\mathcal{I}_h$ (see Lemma 1 and Lemma A.3 in [22]), which will be frequently used in the analysis.

Lemma 6 *(Properties of $\mathcal{I}_h$ [22]). For any $f, g \in W_h(\Omega)$, there hold*

$$\int_\Omega \mathcal{I}_h(fg)d\Omega = \int_\Omega \mathcal{I}_h(f)\mathcal{I}_h(g)d\Omega, \qquad \int_\Omega \mathcal{I}_h(f)\psi d\Omega = \int_\Omega \mathcal{I}_h(f\psi)d\Omega, \quad \forall \psi \in V_h^k. \tag{56}$$

As a special case, we have $\int_\Omega \mathcal{I}_h(\phi\psi)d\Omega = \int_\Omega \phi\psi d\Omega$, $\forall \psi, \phi \in V_h^k$. Moreover

$$\Big|\int_\Omega \mathcal{I}_h(fg)d\Omega\Big| \le C_k\|f\|\|g\|, \quad \forall f, g \in W_h(\Omega). \tag{57}$$

Using the discretization for the Kerr term in (8d) (or in (16b)), the term $\mathcal{N}^n(\boldsymbol{\phi})$ in (42c) can be rewritten as

$$\mathcal{N}^n(\boldsymbol{\phi}) = \epsilon_0\Big(\mathcal{I}_h\big((|\boldsymbol{E}_h^n|^2\mathbb{I} + 2\boldsymbol{E}_h^n\boldsymbol{E}_h^{n\top})\delta_{2\tau}^n\boldsymbol{E}_h - (|\boldsymbol{E}^n|^2\mathbb{I} + 2\boldsymbol{E}^n\boldsymbol{E}^{n\top})\delta_{2\tau}^n\boldsymbol{E}\big), \boldsymbol{\phi}\Big) + \epsilon_0\big(\mathcal{I}_h(\boldsymbol{\tau}_{\boldsymbol{Y}}^n), \boldsymbol{\phi}\big),$$

where $\boldsymbol{\tau}_{\boldsymbol{Y}}^n$ is one local truncation error in (37). By a careful study of the first term in the decomposition above for $\mathcal{N}^n(\boldsymbol{\phi})$, the master error equation (39) will be reformulated as in the next corollary. The proof is given in Appendix C, with (C.4) being a key identity.

Corollary 1 *(Error analysis: an updated master error equation). With $a > 0$, the master error equation in (39) can be reformulated as*

$$\mathcal{E}_h^{n+1/2} - \mathcal{E}_h^{n-1/2} = \tau S_0^n - a\tau\sum_{i=1}^5 S_i^n \tag{58}$$

where $\mathcal{E}_h^{n+1/2}$ gathers the contribution of both linear and nonlinear effects

$$\mathcal{E}_h^{n+1/2} := \widehat{\mathcal{E}}_h^{n+1/2} + a\widetilde{\mathcal{E}}_h^{n+1/2}. \tag{59}$$

The terms S_i^n, $i = 1, \cdots, 5$, and $\widetilde{\mathcal{E}}_h^{n+1/2}$ are

$$S_1^n := \epsilon_0\Big(\mathcal{I}_h\big((|\xi_{\boldsymbol{E}}^n|^2\mathbb{I} + 2\xi_{\boldsymbol{E}}^n\xi_{\boldsymbol{E}}^{n\top} + 2\boldsymbol{A}_h^n\cdot\xi_{\boldsymbol{E}}^n\mathbb{I} + 2\boldsymbol{A}_h^n\xi_{\boldsymbol{E}}^{n\top} + 2\xi_{\boldsymbol{E}}^n\boldsymbol{A}_h^{n\top})\delta_{2\tau}^n\boldsymbol{A}_h\big), \overline{\overline{\xi_{\boldsymbol{E}}^n}}\Big), \tag{60a}$$

$$S_2^n := \epsilon_0\Big(\mathcal{I}_h\big((|\eta_{\boldsymbol{E}}^n|^2\mathbb{I} - 2\boldsymbol{E}^n\cdot\eta_{\boldsymbol{E}}^n\mathbb{I} + 2\eta_{\boldsymbol{E}}^n\eta_{\boldsymbol{E}}^{n\top} - 2\boldsymbol{E}^n\eta_{\boldsymbol{E}}^{n\top} - 2\eta_{\boldsymbol{E}}^n\boldsymbol{E}^{n\top})\delta_{2\tau}^n\boldsymbol{E}\big), \overline{\overline{\xi_{\boldsymbol{E}}^n}}\Big), \tag{60b}$$

$$S_3^n := -\epsilon_0\Big(\mathcal{I}_h\big((|\boldsymbol{A}_h^n|^2\mathbb{I} + 2\boldsymbol{A}_h^n\boldsymbol{A}_h^{n\top})\delta_{2\tau}^n\eta_{\boldsymbol{E}}\big), \overline{\overline{\xi_{\boldsymbol{E}}^n}}\Big), \tag{60c}$$

$$S_4^n := \epsilon_0\big(\mathcal{I}_h(\boldsymbol{\tau}_{\boldsymbol{Y}}^n), \overline{\overline{\xi_{\boldsymbol{E}}^n}}\big), \tag{60d}$$

$$\begin{aligned} S_5^n := -\frac{\epsilon_0}{4}\Bigg\{ & \int_\Omega \mathcal{I}_h\Big(\delta_\tau^{n-1/2}(|\boldsymbol{A}_h|^2)(|\xi_{\boldsymbol{E}}^n|^2 + |\xi_{\boldsymbol{E}}^{n-1}|^2)\Big)d\Omega + 2\int_\Omega \mathcal{I}_h\Big(\xi_{\boldsymbol{E}}^{n\top}\delta_\tau^{n-1/2}(\boldsymbol{A}_h\boldsymbol{A}_h^\top)\xi_{\boldsymbol{E}}^n\Big)d\Omega \\ & + 2\int_\Omega \mathcal{I}_h\Big(\xi_{\boldsymbol{E}}^{n-1\top}\delta_\tau^{n-1/2}(\boldsymbol{A}_h\boldsymbol{A}_h^\top)\xi_{\boldsymbol{E}}^{n-1}\Big)d\Omega + 2\int_\Omega \mathcal{I}_h\Big(\delta_\tau^{n-1/2}(\boldsymbol{A}_h\cdot\xi_{\boldsymbol{E}})(|\xi_{\boldsymbol{E}}^n|^2 + |\xi_{\boldsymbol{E}}^{n-1}|^2)\Big)d\Omega \\ & + 4\int_\Omega \mathcal{I}_h\Big(\xi_{\boldsymbol{E}}^{n\top}\delta_\tau^{n-1/2}(\boldsymbol{A}_h\xi_{\boldsymbol{E}}^\top)\xi_{\boldsymbol{E}}^n\Big)d\Omega + 4\int_\Omega \mathcal{I}_h\Big(\xi_{\boldsymbol{E}}^{n-1\top}\delta_\tau^{n-1/2}(\boldsymbol{A}_h\xi_{\boldsymbol{E}}^\top)\xi_{\boldsymbol{E}}^{n-1}\Big)d\Omega\Bigg\}, \end{aligned} \tag{60e}$$

$$\begin{aligned} \widetilde{\mathcal{E}_h^{n+1/2}} := \frac{\epsilon_0}{4}\Bigg\{ & \|\mathcal{I}_h(|\xi_{\boldsymbol{E}}^{n+1}||\xi_{\boldsymbol{E}}^n|)\|^2 + \int_\Omega \mathcal{I}_h\Big(|\boldsymbol{A}_h^n|^2(|\xi_{\boldsymbol{E}}^{n+1}|^2 + |\xi_{\boldsymbol{E}}^n|^2)\Big)d\Omega + 2\int_\Omega \mathcal{I}_h\Big((\boldsymbol{A}_h^n\cdot\xi_{\boldsymbol{E}}^n)^2\Big)d\Omega \\ & + 2\int_\Omega \mathcal{I}_h\Big((\boldsymbol{A}_h^n\cdot\xi_{\boldsymbol{E}}^{n+1} + \xi_{\boldsymbol{E}}^n\cdot\xi_{\boldsymbol{E}}^{n+1})^2\Big)d\Omega + \int_\Omega \mathcal{I}_h\Big((\boldsymbol{A}_h^n\cdot\xi_{\boldsymbol{E}}^n)(2|\xi_{\boldsymbol{E}}^{n+1}|^2 + 6|\xi_{\boldsymbol{E}}^n|^2)\Big)d\Omega\Bigg\}. \end{aligned} \tag{61}$$

To deal with nonlinearity, we will make an assumption for the L^∞ error of the electric field *during the initial steps* of the proposed methods.

L^∞-Assumption: For $n = 0, 1, 2$, there holds $\|\xi_{\boldsymbol{E}}^n\|_\infty \le C\tau$ for small enough τ. Here C is some *fixed* constant, independent of h, τ.

Theorem 5 *(Error estimates for the Lorentz-Kerr model: $a > 0$). Let $\rho_{err} \in (0, 1 - \sqrt{2/3})$ be any pre-chosen constant. Assume the L^∞-**Assumption** holds and $|\mathcal{E}_h^{3/2}| \le C_{\rho_{err}} C(h^{2k+2} + \tau^4)$. With $\theta = 0$ and periodic boundary conditions, the numerical solutions of the proposed methods (8)-(9) with numerical fluxes (10) and $k > d - 1$ have the following error estimates for $n : 1 < n < N_t$,*

$$\mathcal{E}_{h,\#}^{n+1/2} \le C_{\rho_{err}} C(h^{2k+2} + \tau^4), \tag{62}$$

hence

$$\|e_{\boldsymbol{E}}^n\|, \|\overline{e_{\boldsymbol{H}}^n}\|, \|e_{\boldsymbol{H}}^{n+1/2}\|, \|e_{\boldsymbol{P}}^n\| \le C_{\rho_{err}} C(h^{k+1} + \tau^2), \tag{63}$$

under the time step condition

$$\tau = C_{cfl,LK} h^{d/2+\gamma} \tag{64}$$

and with sufficiently small h, e.g. $h < h_0$ for some $h_0 > 0$. Here $\gamma = 1/2$ when $d = 1$, and when $d = 2, 3$, γ is any pre-chosen sufficiently small real number in $(0, \frac{1}{2}]$, and $C_{cfl,LK} \in [\varrho_m, \varrho_M]$ for a pre-set pair of positive numbers ϱ_m, ϱ_M.

Proof. First of all, we make *a priori* assumption that

$$\|\xi_{\boldsymbol{E}}^n\|_\infty \le C\tau, \qquad 0 \le n < N_t. \tag{65}$$

This assumption will be proved later via mathematical induction.

Step 1: to bound $\mathcal{E}_h^{n+1/2}$ from below. Based on the positivity preserving property in (34) of the interpolation operator $\mathcal{I}_h$, we know all the terms in $\widehat{\mathcal{E}_h^{n+1/2}}$ are non-negative except the last one. For this last term, under the assumption (65) and with the bound on $\boldsymbol{A}_h^n$ in Lemma 5, we have

$$\int_\Omega \mathcal{I}_h\Big((\boldsymbol{A}_h^n \cdot \xi_{\boldsymbol{E}}^n)(2|\xi_{\boldsymbol{E}}^{n+1}|^2 + 6|\xi_{\boldsymbol{E}}^n|^2)\Big) d\Omega \ge -CC\tau(\|\xi_{\boldsymbol{E}}^{n+1}\|^2 + \|\xi_{\boldsymbol{E}}^n\|^2), \tag{66}$$

therefore, in combination with the result in Proposition 1 (hence under the time step condition (47)), and for the sufficiently small τ (i.e. $\tau \le \tau_0$, with $\tau_0 = \rho_{err}\epsilon_0\epsilon_\infty/(8aCC)$),

$$\mathcal{E}_h^{n+1/2} \ge \widehat{\mathcal{E}_{h,\#}^{n+1/2}} + \frac{\epsilon_0 a}{4}\|\mathcal{I}_h(|\xi_{\boldsymbol{E}}^{n+1}||\xi_{\boldsymbol{E}}^n|)\|^2 - aCC\tau(\|\xi_{\boldsymbol{E}}^{n+1}\|^2 + \|\xi_{\boldsymbol{E}}^n\|^2) \ge \mathcal{E}_{h,\#}^{n+1/2},$$

where

$$\begin{aligned}\mathcal{E}_{h,\#}^{n+1/2} =& \rho_{err}\Big(\frac{\mu_0}{2}\|\overline{\xi_{\boldsymbol{H}}^{n+1}}\|^2 + \frac{\epsilon_0\epsilon_\infty}{8}(\|\xi_{\boldsymbol{E}}^{n+1}\|^2 + \|\xi_{\boldsymbol{E}}^n\|^2)\Big) \\ &+ \frac{\epsilon_0 a}{4}\|\mathcal{I}_h(|\xi_{\boldsymbol{E}}^{n+1}||\xi_{\boldsymbol{E}}^n|)\|^2 + \frac{\epsilon_0\omega_0^2}{4\omega_p^2}(\|\xi_{\boldsymbol{P}}^{n+1}\|^2 + \|\xi_{\boldsymbol{P}}^n\|^2).\end{aligned} \tag{67}$$

Step 2: to estimate $\mathcal{S}_i^n, i = 1, \cdots 5$. We start with $\mathcal{S}_1^n$. Using Cauchy-Schwartz inequality, the bounds related to $\boldsymbol{A}_h$ in Lemma 5, and the properties of $\mathcal{I}_h$ in Lemma 6, we get

$$\Big|\big(\mathcal{I}_h((|\xi_{\boldsymbol{E}}^n|^2 + 2\xi_{\boldsymbol{E}}^n\xi_{\boldsymbol{E}}^{n\top})\delta_{2\tau}^n\boldsymbol{A}_h), \overline{\overline{\xi_{\boldsymbol{E}}^n}}\big)\Big| \le C\|\xi_{\boldsymbol{E}}^n\|\big(\|\mathcal{I}_h(|\xi_{\boldsymbol{E}}^{n+1}||\xi_{\boldsymbol{E}}^n|)\| + \|\mathcal{I}_h(|\xi_{\boldsymbol{E}}^n||\xi_{\boldsymbol{E}}^{n-1}|)\|\big), \tag{68}$$

$$\Big|\big(\mathcal{I}_h((\boldsymbol{A}_h^n \cdot \xi_{\boldsymbol{E}}^n\mathbb{I} + \boldsymbol{A}_h^n\xi_{\boldsymbol{E}}^{n\top} + \xi_{\boldsymbol{E}}^n\boldsymbol{A}_h^{n\top})\delta_{2\tau}^n\boldsymbol{A}_h), \overline{\overline{\xi_{\boldsymbol{E}}^n}}\big)\Big| \le C\|\xi_{\boldsymbol{E}}^n\|\Big(\|\xi_{\boldsymbol{E}}^{n+1}\| + \|\xi_{\boldsymbol{E}}^{n-1}\|\Big). \tag{69}$$

For $\mathcal{S}_i^n$, $i = 2, 3, 4$, using the approximation property in Lemma 2 and bounds for local truncation errors in Lemma 3, one has

$$|\sum_{i=2}^4 \mathcal{S}_i^n| \le C(h^{k+1} + \tau^2)\big(\|\xi_{\boldsymbol{E}}^{n+1}\| + \|\xi_{\boldsymbol{E}}^{n-1}\|\big). \tag{70}$$

For $\mathcal{S}_5^n$, we note that

$$\delta_\tau^{n-1/2}(|\boldsymbol{A}_h|^2) = (\delta_\tau^{n-1/2}\boldsymbol{A}_h)\cdot(\boldsymbol{A}_h^n + \boldsymbol{A}_h^{n-1}), \quad \delta_\tau^{n-1/2}(\boldsymbol{A}_h \cdot \xi_{\boldsymbol{E}}) = (\delta_\tau^{n-1/2}\boldsymbol{A}_h)\cdot\xi_{\boldsymbol{E}}^n + \boldsymbol{A}_h^{n-1}\cdot(\delta_\tau^{n-1/2}\xi_{\boldsymbol{E}}).$$

With the *a prior* assumption in (65), $\|\delta_\tau^{n-1/2}\xi_{\boldsymbol{E}}\|_\infty \le C$. This, in combination with the bounds in Lemma 5, implies the uniform boundedness of both terms above with respect to n, τ and the spatial variable. Similarly, one can argue the uniform boundedness of $\delta_\tau^{n-1/2}(\boldsymbol{A}_h\boldsymbol{A}_h^\top)$, $\delta_\tau^{n-1/2}(\boldsymbol{A}_h\xi_{\boldsymbol{E}}^\top)$, $\delta_\tau^{n-1/2}(\boldsymbol{A}_h\xi_{\boldsymbol{E}}^\top)$. With these, one can reach

$$|S_5^n| \le C(\|\xi_{\boldsymbol{E}}^n\|^2 + \|\xi_{\boldsymbol{E}}^{n-1}\|^2). \tag{71}$$

We can combine (43) and (68)-(71), and obtain

$$S_0^n - a\sum_{i=1}^{5} S_i^n \le S_0^n + a|\sum_{i=1}^{5} S_i^n| \le C_{\rho_{err}} C(h^{2k+2} + \tau^4) + C\left(\mathcal{E}_{h,\#}^{n+1/2} + \mathcal{E}_{h,\#}^{n-1/2}\right).$$

Now we sum up the updated master error relation (58), using $\tau n \le T$ and the inequality above, and obtain

$$\mathcal{E}_{h,\#}^{n+1/2} \le \mathcal{E}_h^{n+1/2} \le C_{\rho_{err}} C(h^{2k+2} + \tau^4) + \mathcal{E}_h^{3/2} + \tau C \sum_{m=2}^{n} \left(\mathcal{E}_{h,\#}^{m+1/2} + \mathcal{E}_{h,\#}^{m-1/2}\right) \tag{72}$$

For $\tau \le \tau_1$ (e.g. with $\tau_1 = 1/(2C)$) and with $|\mathcal{E}_h^{3/2}| \le C_{\rho_{err}} C(h^{2k+2} + \tau^4)$, we will have

$$\mathcal{E}_{h,\#}^{n+1/2} \le C_{\rho_{err}} C(h^{2k+2} + \tau^4) + 4\tau C \sum_{m=1}^{n-1} \mathcal{E}_{h,\#}^{m+1/2}, \tag{73}$$

hence the first estimate in (62) following a discrete Gronwall inequality. We also obtain $\|\xi_{\boldsymbol{H}}^{n+1/2}\| \le C_{\rho_{err}} C(h^{k+1} + \tau^2)$ by using the bound in (B.6). Moreover, using triangle inequality $\|e_v\| \le \|\xi_v\| + \|\eta_v\|$ and the approximation properties in Lemma 2, we can conclude the second estimate in (63).

Finally, we want to use mathematical induction to prove the *a prior* assumption (65). This is based on a milder assumption, **L^∞-Assumption**, related to the initial steps. With this milder assumption, suppose $\|\xi_{\boldsymbol{E}}^m\|_\infty \le C\tau$ for all $m \le n$, with n as any given positive integer $n \in [2, N_t)$, then from our error analysis, we know $\|\xi_{\boldsymbol{E}}^{n+1}\| \le C_{err} C(\tau^2 + h^{k+1})$. Using the standard inverse inequality associated with the discrete space V_h^k (see Lemma A.4 in [22]), and a rather stringent time step condition in (64), and a restriction on the polynomial degree, namely, $k > d - 1$, we have

$$\|\xi_{\boldsymbol{E}}^{n+1}\|_\infty \le C_k h^{-d/2} \|\xi_{\boldsymbol{E}}^{n+1}\| \le C_{err} C C_k h^{-d/2}(\tau^2 + h^{k+1}) \le C_{err} C C_k (\varrho_M + \varrho_m^{-1}) \tau h^\gamma. \tag{74}$$

One can set $h_1 = \min(1, \sqrt[\gamma]{C/(C_{err} C C_k (\varrho_M + \varrho_m^{-1}))})$, independent of n, h, τ, such that for any $h \le h_1$, we have $C_{err} C C_k (\varrho_M + \varrho_m^{-1}) h^\gamma \le C$, hence

$$\|\xi_{\boldsymbol{E}}^{n+1}\|_\infty \le C\tau. \tag{75}$$

Particularly, $\gamma = 1/2$ is taken in one dimension (with $d = 1$) so the time step condition (64) is compatible with that in Proposition 1 (i.e. (47)), while when $d = 2, 3$, one needs to impose $\gamma \in (0, 1/2]$ to ensure $k + 1 - d/2 \ge d + 1 - d/2 \ge d/2 + 2\gamma$, hence $h^{k+1-d/2} \le h^{d/2+2\gamma} \le \varrho_m^{-1} \tau h^\gamma$, as in (74). One also notes that with the time step condition (64), τ being sufficiently small is equivalent to h being sufficiently small. Hence the requirements above, namely $\tau \le \min(\tau_0, \tau_1)$ and $h \le h_1$, can be altogether rewritten into $h \le h_0$ for some $h_0 > 0$. □

Remark 6. As in the linear case in Section 3.3.2, assumptions are made without a proof about the errors in the solution during the first few steps, e.g. via **L^∞-Assumption** and $|\mathcal{E}_h^{3/2}| \le C_{\rho_{err}} C(h^{2k+2} + \tau^4)$.

Remark 7. Like in the linear case with $a = 0$, error estimates are optimal for the general Lorentz-Kerr model. For the general model, a rather stringent time step condition (64) is required, along with the constraint on the polynomial degree k, both in their relations to the dimension d. They are needed in order to bound some divided differences of the numerical electric field (e.g. related to $\delta_\tau^{n-1/2} \xi_{\boldsymbol{E}} = \delta_\tau^{n-1/2} \boldsymbol{E}_h - \mathcal{R}_{\boldsymbol{E},h}(\delta_\tau^{n-1/2} \boldsymbol{E})$) present in S_5^n. It is speculated that these restrictive conditions are more a limitation of our analysis, not of the proposed methods themselves, as partially evidenced by numerical experiments. There has been active research on eliminating/relaxing such time step conditions, e.g. in [19] by considering an auxiliary semi-discrete in time methods in the analysis. However it is unclear how to apply such framework, as it seems nontrivial to establish the regularity in high order Sobolev norms of the semi-discrete in time solutions for the nonlinear optical model considered here.

4. Numerical examples

In this section, we will present a set of numerical examples to demonstrate the performance of the proposed methods in terms of their accuracy, efficiency, and energy conservation / stability. Particularly, in combining with the numerical study in [23], our linear methods are shown to be computationally competitive when being compared with the nonlinear ones in [5,22,23]. A scalability study is further performed to illustrate the parallel efficiency. All simulations are performed on uniform meshes (with the mesh size $\Delta\xi$ in ξ-direction, $\xi = x, y, z$), and in double precision unless specified otherwise, and they are based on the nondimensionlized form of the model, though some examples and their results are presented with the physical units for better illustration.

4.1. Accuracy, energy conservation / stability and efficiency

In this section, we investigate the accuracy, energy conservation / stability, computational efficiency and parallel scalability of our proposed linear schemes. The error tolerance[3] in the Newton's iteration (used either in the nonlinear initialization of linear methods, or in nonlinear schemes for comparison) is denoted as Err_{tol} and will be specified, while the local $d_E \times d_E$ linear system (e.g. from the proposed linear methods or during the Newton iterations) is solved based on the analytical expression of the solution. Unless otherwise stated, the maximum number of nonlinear iterations is set as $\max_{it} = 20$.

4.1.1. 1D kink shape solution

We first consider a 1D kink shape solution in $\Omega = [0, 6]$, satisfying the following governing equations

$$\partial_t H = \partial_x E, \quad \partial_t D = \partial_x H,$$
$$\partial_{tt} P = -\omega_0^2 P + \omega_p^2 E, \quad D = \epsilon_\infty E + aE^3 + P,$$

in the absence of the Raman nonlinear effect as well as the damping in the linear dispersive Lorentz effect, i.e. with $\theta = \gamma = 0$. The solution is 6-periodic in space, with the electric field $E(x,t) = \Theta(x - vt)$ determined by

$$\frac{d\Theta}{d\xi} = \Phi, \quad \frac{d\Phi}{d\xi} = \frac{6av^2\Theta\Phi^2 + (\epsilon_\infty\omega_0^2 + \omega_p^2 - \omega_0^2/v^2)\Theta + a\omega_0^2\Theta^3}{1 - \epsilon_\infty v^2 - 3av^2\Theta^2},$$

where $\epsilon_\infty = 2.25$, $\epsilon_s = 5.25$, $\beta_1 = \epsilon_s - \epsilon_\infty$, $\omega_0 = 93.627179982222216$, $\omega_p = \omega_0\sqrt{\beta_1}$, $a = \epsilon_\infty/3$, $v = 0.6545/\sqrt{\epsilon_\infty}$, $E(0) = 0$, $\Phi(0) = 0.24919666777865812$. One can follow the procedure in [5] to get the initial conditions for other quantities.

The simulation is performed up to the final time $T = 9/v$. To match the $(k+1)$-th order spatial accuracy, we pre-set $dt = C\Delta x^{(k+1)/2}$ with $C = 0.2/v$ for $k = 1$, $C = 1$ for $k = 2$, and $C = 2$ for $k = 3$, and the actual time step size is taken as $\tau = \frac{T}{\lceil T/dt \rceil + 1}$ to ensure a uniform mesh in time. Here $\lceil x \rceil$ represents the greatest integer less than or equal to x. This test is carried out sequentially using Fortran on a computer with Intel Core i7-10850H CPU 2.70 GHz and 64 GB Memory.

Accuracy, comparison and efficiency. In Table 1 (left panel), we present the numerical errors and convergence rates of the electric field E_h at the final time T of the proposed linear methods with Alternating I flux. One can observe the optimal $(k+1)$-th order convergence rates for $k = 1, 2, 3$ especially in the L^2 norm. As a comparison, we also provide the results by the nonlinear schemes proposed in [5] (implemented in the nodal DG setting, instead of the original modal DG setting, for better efficiency) with the error tolerance $Err_{tol} = 10^{-5}$ (see right panel). The CPU times (measured in seconds) are reported in the columns "t_{cpu}". One will see that the linear methods are more cost efficient than the nonlinear ones, when the same time step size is taken in both methods. Results with Alternating II flux lead to similar observation, and they are omitted.

One natural question will arise: is the comparison above fair for cost efficiency, given that the allowable time step sizes to ensure provable discrete energy laws are not the same for the linear methods here and for the nonlinear ones, as discussed in Remark 2. Particularly, our analysis indicates smaller time step sizes are required for the linear methods. Though it is theoretically challenging to know whether our analysis gives sharp bounds for allowable time step sizes, numerical experiments can provide some insights. For this, we take $k = 2$ and $N_x = 800$ and use Alternating I flux, and report in Fig. 1 the L^2 (solid line) and L^∞ (dashed line) errors in E_h at the final time T (left figure) as well as the CPU times (right figure) of the linear method and nonlinear method [5] for a set of different values of the actual time step size τ. When both methods work well (i.e. are stable) with the same τ taken, they lead to visually indistinguishable errors, with linear methods showing better cost efficiency, just as observed from Table 1. As τ grows, particularly when $\tau \geq 1.857567759 \times 10^{-3}$, neither method produces reliable solutions: the L^2 error in the solution by the nonlinear method suddenly jumps to 2.07857×10^{-2} from 5.48822×10^{-7} and the number of nonlinear Newton iteration grows, while the linear method will blow up shortly afterward. One can also refer to Fig. 2 for some computed E_h at T with three sampled values of τ. This study seems to suggest that both nonlinear and linear methods allow comparable time step sizes for stability, and our analysis for the allowable time step size is not sharp, at least not for the proposed linear methods. It is therefore reasonable to compare the cost efficiency of both methods by taking the same time step size as in Table 1.

Surely the actual running time of nonlinear methods depends closely on the stopping criteria. In the column "*iter*" of Table 1, the average number of Newton's iterations per time step is recorded for the nonlinear methods. With $Err_{tol} = 10^{-5}$, averagely 1-2 Newton's iterations are needed. To have a more comprehensive assessment and comparison between the linear and nonlinear methods, we carry out two additional tests for nonlinear methods with Alternating I flux. The first one is to keep $Err_{tol} = 10^{-5}$ while allowing only one Newton's iteration (see the left panel of Table 2). This test is natural, as the readers will wonder whether "nonlinear methods with single Newton's iteration" shall perform similarly as the proposed linear methods. The second test is to take $Err_{tol} = 10^{-4}$ (see the right panel of Table 2). In both scenarios, one will observe some level of accuracy deterioration while the computational cost is still higher than the respective one of the linear schemes especially on finer meshes. This again shows that the setting for the comparison in Table 1 is reasonable.

If we take into account the optimal accuracy of the methods, our observations up to now show that the linear methods here are computationally more efficient. Indeed, in combination with our previous study in [23] (see its Tables 1-2), one can conclude that

[3] For each $d_E \times d_E$ nonlinear system $F(u) = 0$ associated with an interpolation point, the classical Newton's iteration method is applied with $\|F(u^s)\|_\infty < Err_{tol}$.

Table 1
1D kink shape solution: numerical errors and convergence rates of E_h of the proposed methods ("linear methods") and the methods in [5] ("nonlinear methods") with $Err_{tol} = 10^{-5}$ and Alternating I flux, CPU times, averaged iteration numbers in nonlinear iteration.

N_x	linear methods					nonlinear methods					
	L^2		L^∞		t_{cpu}	L^2		L^∞		t_{cpu}	*iter*
$k=1$											
100	1.4E-04	-	5.7E-04	-	0.00	1.3E-04	-	5.5E-04	-	0.01	1.9
200	3.8E-05	1.9	1.5E-04	1.9	0.01	4.2E-05	1.6	1.9E-04	1.5	0.02	1.9
400	1.3E-05	1.5	5.3E-05	1.5	0.11	1.2E-05	1.8	4.4E-05	2.1	0.15	1.7
800	3.6E-06	1.9	1.6E-05	1.7	0.15	3.3E-06	1.9	1.5E-05	1.6	0.31	1.4
1600	9.1E-07	2.0	3.8E-06	2.1	0.59	7.4E-07	2.2	4.0E-06	1.9	1.18	1.3
$k=2$											
100	3.5E-05	-	1.8E-04	-	0.01	3.5E-05	-	1.7E-04	-	0.02	1.5
200	4.4E-06	3.0	2.2E-05	3.0	0.05	4.4E-06	3.0	2.2E-05	3.0	0.08	1.4
400	5.5E-07	3.0	2.8E-06	3.0	0.61	5.5E-07	3.0	2.7E-06	3.0	0.86	1.3
800	6.9E-08	3.0	3.5E-07	3.0	1.46	6.9E-08	3.0	3.5E-07	2.9	2.59	1.3
$k=3$											
100	8.3E-06	-	3.5E-05	-	0.02	8.4E-06	-	3.5E-05	-	0.04	1.4
200	5.2E-07	4.0	2.1E-06	4.1	0.13	5.2E-07	4.0	2.2E-06	4.0	0.28	1.3
400	3.3E-08	4.0	1.5E-07	3.8	2.38	3.3E-08	4.0	1.5E-07	3.9	3.86	1.2

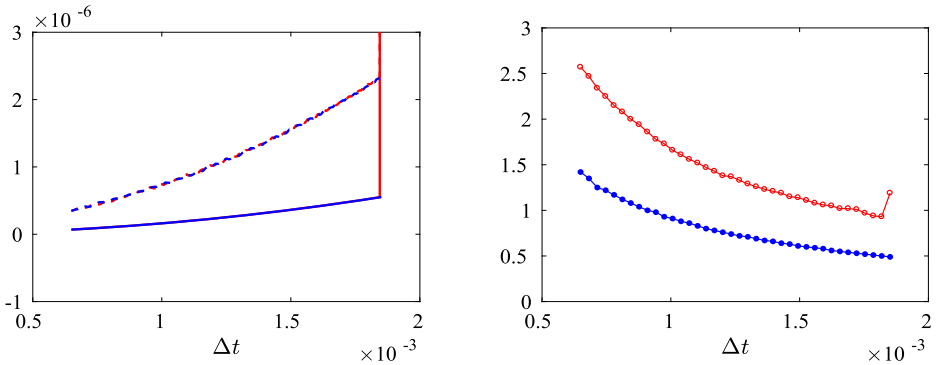

Fig. 1. 1D kink shape solution, with $k=2$, $N_x=800$ and Alternating I flux. Left: L^2 (solid line) and L^∞ (dashed line) errors in E_h versus the time step size τ, right: the CPU times. Red: nonlinear methods [5], blue: linear method.

the proposed linear methods here are relatively more cost efficient than the nonlinear ones in [5] (based on the first order form of the model) and in [23] (based on the mixed order form of the model), with each achieving the designed accuracy orders.

Energy conservation. For this example ($\theta=0,\gamma=0$), the exact solution satisfies an energy conservation relation as in (3). As a final test in this subsection, in Fig. 3, we present the time histories of the energy deviation from the initial energy, namely, $\mathcal{E}_{h,LK}^{n+1/2}-\mathcal{E}_{h,LK}^{3/2}$ as n increases, on the mesh with $N_x=400$, when $k=1,2,3$ with alternating fluxes. The results show that the discrete energy $\mathcal{E}_{h,LK}^{n+1/2}$ is conserved up to machine accuracy, validating our theoretical findings in Theorem 2.

When $k=3$, the energy deviation shows linear growth in time. (This trend is also observed over a longer time interval $[0,200]$.) Similar linear growth was reported for nonlinear methods (e.g. Figure 6.2(c) in [5]). It seems this linear growth is an artifact associated with the finite precision computation, and this is partially supported by the histories of the energy deviation computed in higher precisions, see Fig. 3. Recall that by default the numerical results in this work are obtained from simulations in double precision.

4.1.2. 3D manufactured solution

In this section, we will conduct several tests in 3D.

Accuracy and efficiency. The accuracy of the proposed methods will be demonstrated through a manufactured solution in the domain $\Omega=\left[0,\frac{2\pi}{|k_x|}\right]\times\left[0,\frac{2\pi}{|k_y|}\right]\times\left[0,\frac{2\pi}{|k_z|}\right]$, where $\boldsymbol{k}=(k_x,k_y,k_z)^\top$ is a nonzero wave vector. We take

$$\boldsymbol{D}(\boldsymbol{x},t)=\begin{pmatrix}\mathcal{D}_x\\ \mathcal{D}_y\\ \mathcal{D}_z\end{pmatrix}\cos(\boldsymbol{k}\cdot\boldsymbol{x}+|\boldsymbol{k}|t),\quad \boldsymbol{H}(\boldsymbol{x},t)=\begin{pmatrix}\mathcal{H}_x\\ \mathcal{H}_y\\ \mathcal{H}_z\end{pmatrix}\cos(\boldsymbol{k}\cdot\boldsymbol{x}+|\boldsymbol{k}|t), \tag{76}$$

with

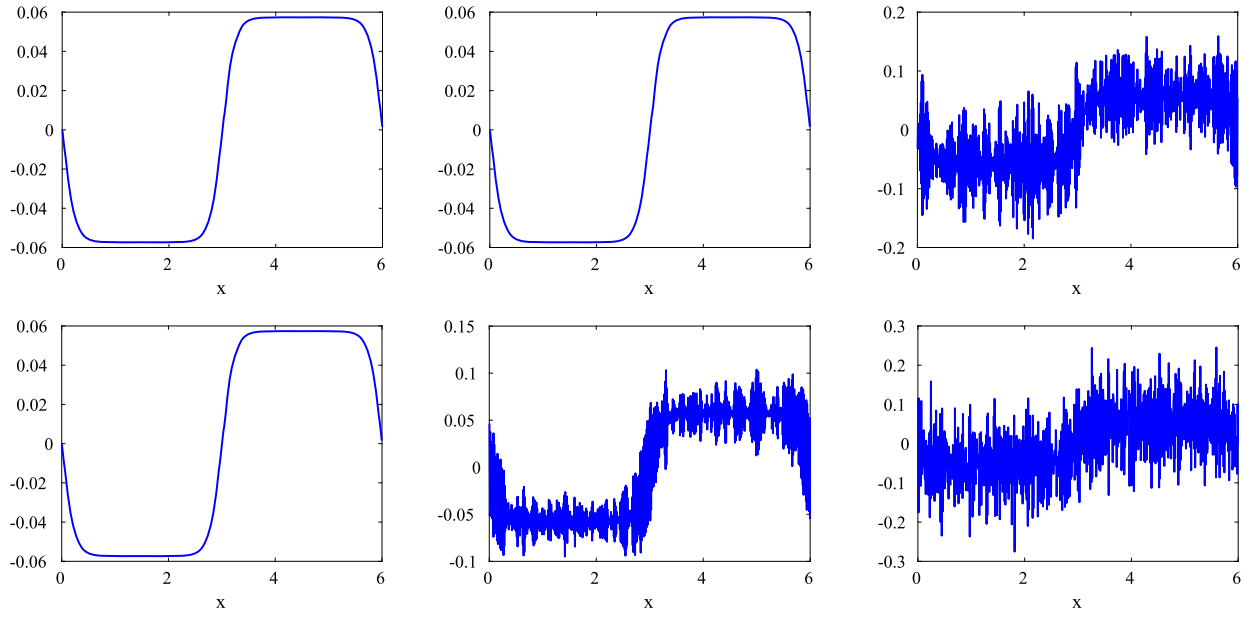

Fig. 2. 1D kink shape solution, the computed E_h at T with $k = 2$, $N_x = 800$ and Alternating I flux. Top: linear method, bottom: nonlinear methods; Left: $\tau = 1.844610301 \times 10^{-3}$, middle: $\tau = 1.851066355 \times 10^{-3}$, right: $\tau = 1.857567759 \times 10^{-3}$.

Table 2
1D kink shape solution: numerical errors and convergence rates of E_h of the "nonlinear methods" in [5] with Alternating I flux, and CPU times. Left panel: one iteration allowed with $\max_{it} = 1$, $Err_{tol} = 10^{-5}$, right panel: $Err_{tol} = 10^{-4}$.

N_x	$\max_{it} = 1$, $Err_{tol} = 10^{-5}$					$Err_{tol} = 10^{-4}$					
	L^2		L^∞		t_{cpu}	L^2		L^∞		t_{cpu}	*iter*
$k = 1$											
100	1.3E-04	-	5.8E-04	-	0.00	1.3E-04	-	5.5E-04	-	0.01	1.6
200	4.2E-05	1.6	2.0E-04	1.5	0.01	4.2E-05	1.6	1.9E-04	1.5	0.02	1.4
400	1.2E-05	1.8	4.8E-05	2.1	0.10	1.2E-05	1.8	4.4E-05	2.1	0.13	1.3
800	3.5E-06	1.8	1.8E-05	1.4	0.18	3.3E-06	1.9	1.5E-05	1.6	0.28	1.2
1600	8.6E-07	2.0	4.8E-06	1.9	0.73	7.5E-07	2.1	3.9E-06	1.9	1.11	1.1
$k = 2$											
100	3.6E-05	-	1.7E-04	-	0.01	3.5E-05	-	1.7E-04	-	0.01	1.3
200	4.6E-06	3.0	2.3E-05	2.9	0.05	4.4E-06	3.0	2.2E-05	3.0	0.08	1.2
400	7.4E-07	2.6	3.3E-06	2.8	0.54	5.7E-07	2.9	2.7E-06	3.0	0.70	1.1
800	1.8E-07	2.0	7.2E-07	2.2	1.71	1.8E-07	1.7	7.2E-07	1.9	2.44	1.0
$k = 3$											
100	8.6E-06	-	3.5E-05	-	0.02	8.4E-06	-	3.5E-05	-	0.04	1.3
200	7.0E-07	3.6	2.9E-06	3.6	0.17	5.4E-07	4.0	2.1E-06	4.1	0.26	1.1
400	1.2E-07	2.5	4.6E-07	2.7	2.49	1.2E-07	2.2	4.6E-07	2.2	3.34	1.0

$$(\mathcal{D}_x, \mathcal{D}_y, \mathcal{D}_z)^\top = e_0\Big(1, -\frac{k_x^2 + k_z^2}{k_x k_y}, \frac{k_z}{k_x}\Big)^\top, \quad (\mathcal{H}_x, \mathcal{H}_y, \mathcal{H}_z)^\top = e_0|\boldsymbol{k}|\Big(-\frac{k_z}{k_x k_y}, 0, \frac{1}{k_y}\Big)^\top, \tag{77}$$

and a constant e_0. These fields satisfy the PDE part of the system (1a)-(1b). We further take

$$\boldsymbol{E}(\boldsymbol{x}, t) = \boldsymbol{P}(\boldsymbol{x}, t) = \boldsymbol{D}(\boldsymbol{x}, t), \quad Q(\boldsymbol{x}, t) = \mathcal{H}_z \cos(\boldsymbol{k} \cdot \boldsymbol{x} + |\boldsymbol{k}|t), \tag{78}$$

and add source terms to the part of the system related to the constitutive law, namely, (1c)-(1d) and (2), so the fields specified above will satisfy the system (modified with additional sources) with periodic boundary conditions in space. In our simulation, we fix $e_0 = 1$ and $\boldsymbol{k} = (1, 1, 1)^\top$, with the model parameters $\epsilon_\infty = 2.0$, $\omega_0 = \omega_p = 1.0$, $\gamma = 0.05$, $a = 0.2$, $\theta = 0.3$, $\omega_v = 1.0$, $\gamma_v = 0.05$. The final time is $T = \frac{1}{|\boldsymbol{k}|}$, and the time step τ is set as

$$\tau = \frac{T}{\lceil T/dt \rceil + 1}, \text{ with } dt = Ch^{\frac{k+1}{2}}, C = 0.1, h = \frac{3}{1/\Delta x + 1/\Delta y + 1/\Delta z}.$$

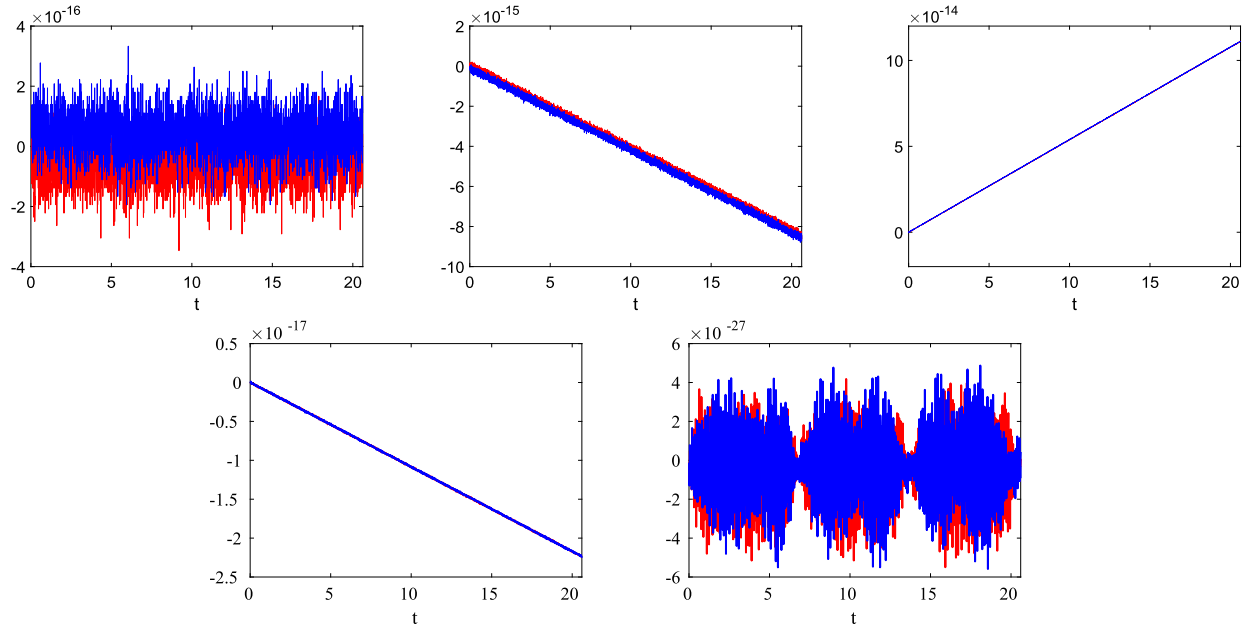

Fig. 3. 1D kink shape solution: energy deviation $\mathcal{E}^{n+1/2}_{h,LK} - \mathcal{E}^{3/2}_{h,LK}$. Top: in double precision, $k = 1$ (left), $k = 2$ (middle), $k = 3$ (right). Bottom: in higher precision and for $k = 3$, with 20 effective digits (left) and 32 effective digits (right). Mesh: $N_x = 400$. Blue: Alternating I, red: Alternating II.

This experiment is carried out using MPI Fortran on the cluster LSSC-IV of the State Key Laboratory on Scientific and Engineering Computing, Chinese Academy of Sciences, with 1000 processors.

In Table 3, we present the numerical errors, convergence rates for the first component E_{xh} and the CPU times by the proposed linear methods and by the nonlinear methods in [22] with the error tolerance $Err_{tol} = 10^{-6}$, both using Alternating I flux. Optimal $(k+1)$-th order convergence rates are achieved for $k = 1, 2, 3$. The errors of the two families of methods are comparable yet the CPU times elapsed by the linear methods are less than those of the nonlinear ones. Note that on average 4-5 Newton's iterations are needed per time step. Similar observation has been made when Alternating II flux is applied, with the results omitted.

Just as in 1D case, we perform two additional sets of tests for the nonlinear methods to have a better assessment of the computational efficiency. The first test is to take $Err_{tol} = 10^{-5}$, and the second test is to keep $Err_{tol} = 10^{-6}$ while limiting the maximum Newton's iterations to be $\max_{it} = 4$ for each nonlinear update. In either case, CPU times are still higher than those of the linear methods, while some level of deterioration is observed in accuracy order or in actual errors. The results are not included to save space. Again, in combination with our previous study in [23] (see its Tables 3-4) for 2D examples, it seems one can conclude that the proposed linear methods here are computationally competitive in comparison to the nonlinear ones in [22] (based on the first order form of the model) and in [23] (based on the mixed order form of the model), with each achieving the designed accuracy orders.

Energy conservation / stability. We start with verifying the energy conservation property of the proposed methods for the Lorentz-Kerr model as suggested in Theorem 2. To this end, we set $\theta = \gamma = 0$ and switch off the artificial source terms in the simulations. The fields in (76)-(78) are used as the initial conditions (and they are no longer the exact solutions). The evolution of the energy deviation from the initial energy, namely, $\mathcal{E}^{n+1/2}_{h,LK} - \mathcal{E}^{3/2}_{h,LK}$, up to time $T = 100/|\boldsymbol{k}|$ are shown in Fig. 4 for the two numerical fluxes on the mesh of $N_x = N_y = N_z = 20$. One can observe that the discrete energy preserves quite well over long time simulation.

We next show the energy stability of the proposed linear methods for the full Lorentz-Kerr-Raman model with both the nonlinear Kerr and Raman effects. In order to focus on the time evolution of the energy related to the discretization yet not due to the physical damping, we turn off the damping and take $\gamma = \gamma_v = 0$. With $\theta = 0.3$, the model satisfies an energy conservation law (3)-(4), though a discrete analogue of such law is not rigorously available for our linear methods. Nevertheless, we measure the energy numerically using the discrete quasi-energy $\mathcal{E}^{n+1/2}_{h,LKR}$ in (35), and present the time history of its relative deviation $\left(\mathcal{E}^{n+1/2}_{h,LKR} - \mathcal{E}^{3/2}_{h,LKR}\right) \Big/ \mathcal{E}^{3/2}_{h,LKR}$ in Fig. 5. As one can see, the discrete quasi-energy $\mathcal{E}^{n+1/2}_{h,LKR}$ fluctuates around the initial energy $\mathcal{E}^{3/2}_{h,LKR} (\approx 3000)$ within a relative deviation at the magnitude of 10^{-5}, and well stays bounded over time. This provides a numerical evidence that the proposed methods for the full Lorentz-Kerr-Raman model are stable in time. It is yet to find out whether a discrete energy law can be established for the proposed methods respect to either the discrete quasi-energy $\mathcal{E}^{n+1/2}_{h,LKR}$ or some better defined discrete energy.

Parallel scalability. We conclude this section with a parallel scalability study of the linear methods. Since the methods are explicit in the PDE part and extremely local, one would expect them to have similar parallel efficiency as the standard explicit DG methods applied to hyperbolic problems [4]. As in the standard MPI implementation, we divide the computational domain into N_p subdomains, with N_p being the number of the processors, then advance in time the methods in each subdomain on one processor, and at the same

Table 3
3D manufactured solution: numerical errors and convergence rates of E_{xh} of the proposed methods ("linear methods") and the methods in [22] ("nonlinear methods") with $Err_{tol} = 10^{-6}$ and Alternating I flux, CPU times, averaged numbers of nonlinear iterations. $N_x = N_y = N_z = N$.

N	linear methods					nonlinear methods					
	L^2		L^∞		t_{cpu}	L^2		L^∞		t_{cpu}	*iter*
$k = 1$											
20	6.9E-03	-	3.7E-02	-	0.43	6.8E-03	-	3.7E-02	-	0.20	4.8
40	1.8E-03	1.9	9.2E-03	2.0	0.02	1.7E-03	2.0	9.2E-03	2.0	0.03	4.7
80	5.2E-04	1.8	2.5E-03	1.9	0.30	5.1E-04	1.7	2.5E-03	1.9	0.99	4.6
160	1.3E-04	2.0	8.0E-04	1.6	5.31	1.3E-04	2.0	8.1E-04	1.6	8.73	4.6
320	3.2E-05	2.0	1.9E-04	2.1	53.1	3.2E-05	2.0	1.9E-04	2.1	100	4.6
640	8.3E-06	1.9	4.6E-05	2.0	816	8.3E-06	1.9	4.6E-05	2.0	1554	4.6
$k = 2$											
20	1.9E-04	-	8.9E-04	-	0.48	1.8E-04	-	8.4E-04	-	0.27	4.7
40	2.5E-05	2.9	1.1E-04	3.0	0.45	2.3E-05	3.0	1.0E-04	3.1	0.46	4.6
80	3.1E-06	3.0	1.6E-05	2.8	6.99	2.9E-06	3.0	1.3E-05	2.9	9.85	4.6
160	4.2E-07	2.9	2.6E-06	2.6	111	4.0E-07	2.9	2.1E-06	2.6	160	4.6
320	5.0E-08	3.1	3.3E-07	3.0	2360	4.7E-08	3.1	2.7E-07	3.0	3434	4.6
$k = 3$											
20	3.2E-05	-	7.6E-05	-	0.37	1.5E-05	-	3.8E-05	-	0.45	4.6
40	2.0E-06	4.0	4.8E-06	4.0	3.31	9.5E-07	4.0	2.5E-06	3.9	5.17	4.6
80	1.3E-07	3.9	2.9E-07	4.0	89.1	5.9E-08	4.0	1.7E-07	3.9	107	4.6
160	7.9E-09	4.0	2.0E-08	3.9	2627	3.8E-09	4.0	1.3E-08	3.7	3184	4.6

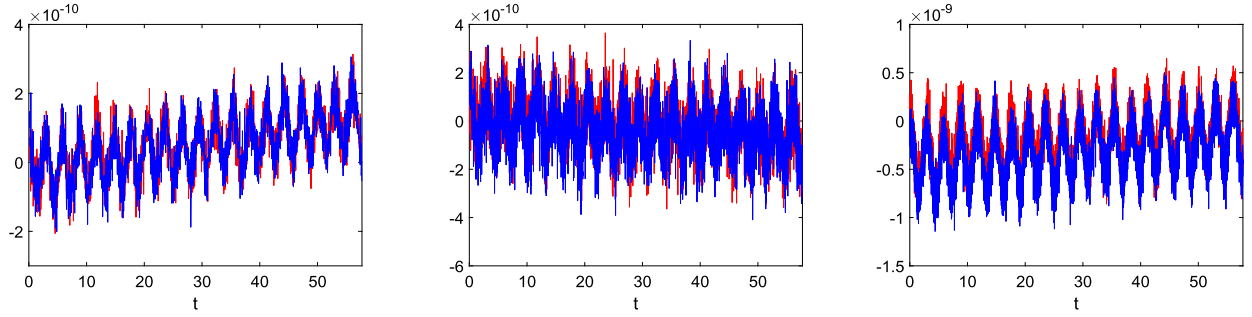

Fig. 4. 3D example: energy deviation $\mathcal{E}^{n+1/2}_{h,LK} - \mathcal{E}^{3/2}_{h,LK}$ for the Lorentz-Kerr model. Left: $k = 1$, middle: $k = 2$, right: $k = 3$. Mesh: $N_x = N_y = N_z = 20$. Blue: Alternating I, red: Alternating II.

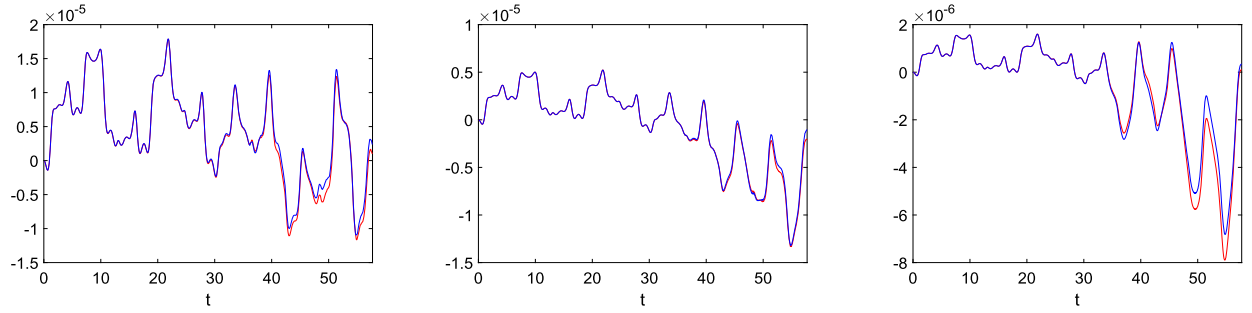

Fig. 5. 3D example: relative quasi-energy deviation $\left(\mathcal{E}^{n+1/2}_{h,LKR} - \mathcal{E}^{3/2}_{h,LKR}\right) \Big/ \mathcal{E}^{3/2}_{h,LKR}$ for the full Lorentz-Kerr-Raman model. Left: $k = 1$, middle: $k = 2$, right: $k = 3$. Mesh: $N_x = N_y = N_z = 20$. Blue: Alternating I, red: Alternating II.

time, exchange information between the neighboring processors in a surrounding ghost layer [3]. We here take Alternating I flux and $k = 2$ as an example to examine both the strong and weak scalability of the methods.

In the strong scalability study, we fix the problem size by taking $N_x = N_y = N_z = 80$. In Table 4, we report the speed-up and parallel efficiency E_{strong} as the number of processors N_p increases from $N_p = 1$ to $N_p = 1024$. Here, the "speed-up" is the CPU time of one processor over that of N_p processors, and $E_{\text{strong}} = \frac{\text{speed-up}}{N_p}$. One can see that the "speed-up" scales with the number of

Table 4
Strong scalability: $k = 2$, Alternating I flux, $N_x = N_y = N_z = 80$.

N_p	t_{cpu}	speed-up	E_{strong}
1-8 1	4239.73	–	–
2	2126.85	1.99	99.67%
4	1068.37	3.97	99.21%
8	538.28	7.88	98.46%
16	270.60	15.67	97.92%
32	136.50	31.06	97.06%
64	68.26	62.11	97.05%
128	34.92	121.41	94.85%
256	18.02	235.34	91.93%
512	9.56	443.51	86.62%
1024	9.52	445.51	43.51%

Table 5
Weak scalability: $k = 2$, Alternating I flux.

N_p	$N_x \times N_y \times N_z$	t_{cpu}	E_{weak}
1	$20 \times 20 \times 20$	50.54	–
2	$40 \times 20 \times 20$	51.41	98.31%
4	$40 \times 40 \times 20$	51.47	98.19%
8	$40 \times 40 \times 40$	51.52	98.11%
16	$80 \times 40 \times 40$	52.08	97.05%
32	$80 \times 80 \times 40$	52.45	96.37%
64	$80 \times 80 \times 80$	53.32	94.79%
128	$160 \times 80 \times 80$	55.20	91.56%
256	$160 \times 160 \times 80$	55.92	90.41%
512	$160 \times 160 \times 160$	59.26	85.29%
1024	$320 \times 160 \times 160$	60.29	83.84%

processors, achieving over 91% efficiency on up to 256 processors. The efficiency reduction for $N_p = 512$ and 1024 is due to the communication between neighboring processors.

To examine the weak scalability, we increase the problem size and the number of processors simultaneously while keeping the task over each processor almost identical. A weak parallel efficiency E_{weak} is defined as the CPU time with one single processor over that by N_p processors. In Table 5, we provide the CPU times for running the simulations over 200 time steps on different meshes using different numbers of processors. As we can see, over 90% (resp. 80%) efficiency is achieved on up to 256 processors (resp. 1024 processors), exhibiting good scalability for large scale simulations.

4.2. Physically relevant simulations

In this section, we apply the proposed linear methods to some physically relevant wave propagation problems in 1D, 2D and 3D. In our simulations, numerical fluxes are chosen according to the kind of incident waves injected to the computational domain. More specifically, if an incident wave is given in terms of the electric field $\boldsymbol{E}(\boldsymbol{x}, t)$ (resp. the magnetic field $\boldsymbol{H}(\boldsymbol{x}, t)$) on (part of) the inflow boundary with respect to the prescribed direction $(1, 1, 1)^\top$, e.g. at $x = x_a$, or at $y = y_a$, the Alternating I (resp. II) flux will be used. On the remaining boundaries of the domain, we adopt the strategy of approximate absorbing boundary conditions as in [5,22], and apply some modified numerical fluxes, see e.g. Section 6.2 in [5]. As observed previously in [22], these artificial numerical boundary treatments can be further improved especially over long time simulation in order to effectively suppress nonphysical reflection at boundaries. For the two numerical examples in Sections 4.2.2-4.2.3, computational domains larger than the domains of interest will be taken in the actual simulation to reduce the artifacts of numerical boundary treatments. All initial conditions are set to be zero. The DG space V_h^k with $k = 2$ and $k = 1$ are used in the 2D and 3D examples, respectively. In the simulations, we use 500 and 1000 processors for the 2D and 3D simulations, respectively. When applying the nonlinear schemes in the initialization (see Algorithm 1), the error tolerance and the maximum number of nonlinear iterations by the Newton's method are taken as $Err_{tol} = 10^{-8}$ and $\max_{it} = 20$, respectively.

4.2.1. 1D soliton-like wave propagation

In this example, we simulate a soliton-like wave propagation in 1D [12,5], with the governing equations

$$\partial_t H - \partial_x E = 0, \quad \partial_t D - \partial_x H = 0,$$
$$D = \epsilon_\infty E + P + a(1-\theta)E^3 + a\theta Q E,$$
$$\partial_{tt} P + \gamma \partial_t P + \omega_0^2 P = \omega_p^2 E,$$

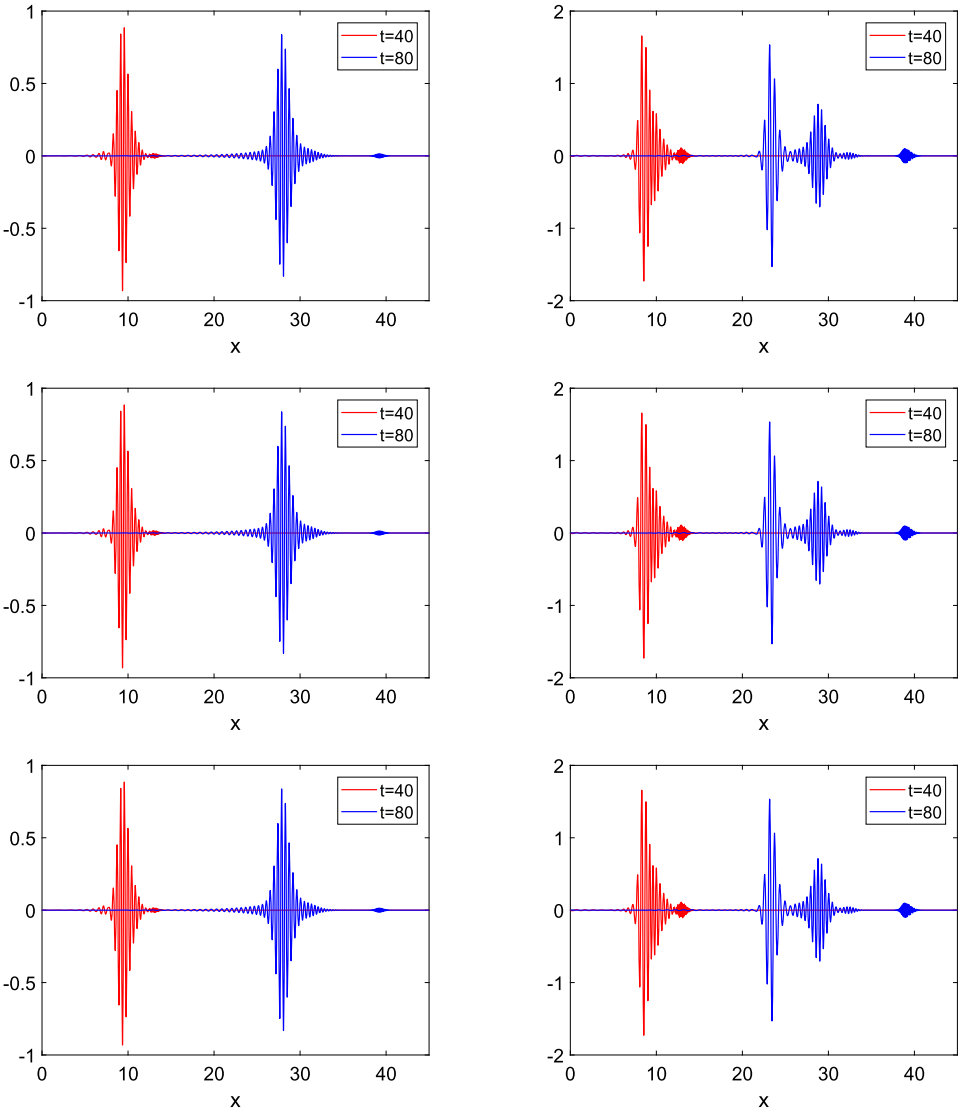

Fig. 6. 1D soliton-like wave propagation. Left column: fundamental soliton with $M = 1$. Right column: second-order soliton with $M = 2$. From top to bottom: $k = 1, 2, 3$.

$$\partial_{tt} Q + \gamma_v \partial_t Q + \omega_v^2 Q = \omega_v^2 E^2,$$

and the model parameters

$$\epsilon_\infty = 2.25, \quad \epsilon_s = 5.25, \quad \beta_1 = \epsilon_s - \epsilon_\infty, \quad \gamma = 1.168 \times 10^{-5}, \quad \gamma_v = 29.2/32,$$
$$a = 0.07, \quad \theta = 0.3, \quad \Omega_0 = 12.57, \quad \omega_0 = 5.84, \quad \omega_v = 1.28, \quad \omega_p = \omega_0 \sqrt{\beta_1}.$$

On the left boundary $x = 0$, an incident wave as follows will enter

$$E(x = 0, t) = f(t) \cos(\Omega_0 t), \quad f(t) = M \operatorname{sech}(t - 20), \tag{79}$$

where M physically characterizes the order of solitons. The computational domain is taken as $\Omega = [0, 45]$. At $x = 0$, the boundary condition is weakly imposed through the use of Alternating I numerical flux; at $x = 45$, an approximate absorbing boundary condition as in [5] is applied numerically. The final time is $T = 80$. For $k = 1, 2, 3$, the spatial and temporal meshsizes are taken as $\Delta x = 45/6400$, $\tau = 0.1\Delta x$.

In Figs. 6, we present the snapshots of the electric fields corresponding to the fundamental ($M = 1$) and second-order ($M = 2$) solitons at $t = 40$ and $t = 80$ for $k = 1, 2, 3$. The results are in good agreement with those obtained by the nonlinear schemes in [5,23]. Fig. 7 provides the time history of the discrete quasi-energy $\mathcal{E}_{h,LKR}^{n+1/2}$ of the system. Due to the damping effect of the medium, one can observe this quasi-energy decays after the wave fully enters the domain, showing the robustness of the proposed schemes. During the

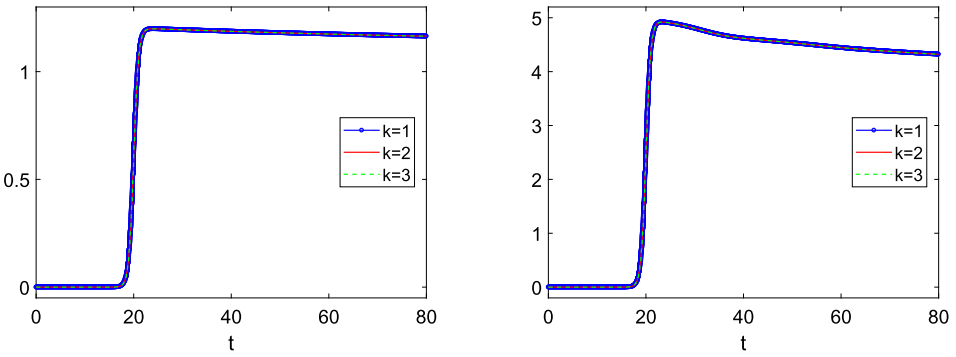

Fig. 7. 1D soliton-like wave propagation: time history of the discrete quasi-energy $\mathcal{E}_{h,LKR}^{n+1/2}$. Left: $M=1$, right: $M=2$.

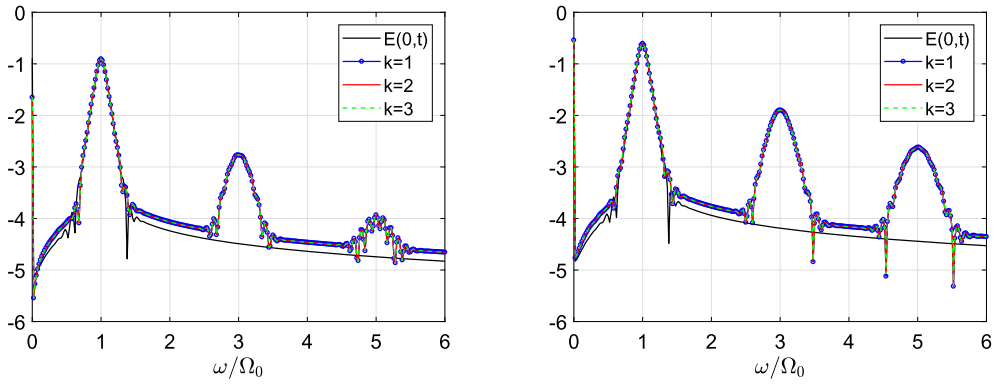

Fig. 8. 1D soliton-like wave propagation: semi-log plot of the spectrum, $\log_{10}\mathrm{E}(\omega)$, where $\mathrm{E}(\omega)$ is the discrete Fourier transform of E_h^n at $x=0.2$ over the time period $[0, 2\pi\times 50/\Omega_0]$. Left: $M=1$, right: $M=2$.

simulation, we record the electric field E_h^n at $x=0.2$ for 50 time periods, namely, over $[0, 2\pi\times 50/\Omega_0]$, and apply the discrete Fourier transform to convert the data from the time domain to frequency domain. As is shown in Fig. 8, apart from the linear response, higher order (particularly, the third and fifth orders) harmonic waves are generated in the process as one would expect for such system.

4.2.2. 2D spatial-soliton propagation

In this example, we simulate a 2D spatial-soliton propagation in optical glasses with the three-pole Sellmeier linear dispersion, nonlinear Kerr and Raman scattering [14]. The (dimensional) governing equations are

$$\mu_0\partial_t H_z + \partial_x E_y - \partial_y E_x = 0, \tag{80a}$$

$$\partial_t D_x - \partial_y H_z = 0, \quad \partial_t D_y + \partial_x H_z = 0, \tag{80b}$$

$$\boldsymbol{D} = \epsilon_0\Big(\epsilon_\infty \boldsymbol{E} + b\sum_{s=1}^{3}\boldsymbol{P}_s + a(1-\theta)|\boldsymbol{E}|^2\boldsymbol{E} + a\theta Q\boldsymbol{E}\Big), \tag{80c}$$

$$\partial_{tt}\boldsymbol{P}_s + \gamma_s\partial_t\boldsymbol{P}_s + \omega_{0s}^2\boldsymbol{P}_s = \omega_{ps}^2\boldsymbol{E}, \quad s=1,2,3, \tag{80d}$$

$$\partial_{tt}Q + \gamma_v\partial_t Q + \omega_v^2 Q = \omega_v^2|\boldsymbol{E}|^2, \tag{80e}$$

where $\omega_{01}=2.7537\times10^{16}$ rad/s, $\omega_{02}=1.6205\times10^{16}$ rad/s, $\omega_{03}=1.9034\times10^{14}$ rad/s, $\beta_1=0.69617$, $\beta_2=0.40794$, $\beta_3=0.89748$; $\omega_{ps}=\sqrt{\beta_s}\omega_{0s}$, $\gamma_s=0$, $s=1,2,3$, $\epsilon_\infty=1.0$, $b=1.0$, $a=1.89\times10^{-22}$ m^2/V^2, $\theta=0.3$, $\tau_1=12.2$ fs, $\tau_2=32.0$ fs, $\gamma_v=2/\tau_2$, $\omega_v=\sqrt{(\tau_1^2+\tau_2^2)/(\tau_1^2\tau_2^2)}$. Note that, the system (80) is formulated in the TE mode, where the two components of the electric field $\boldsymbol{E}=(E_x,E_y)^\top$ are nonlinearly coupled via the constitutive relation (80c) (and (80e)).

The computational domain is $\Omega=[0,60\ \mu\mathrm{m}]\times[-4\ \mu\mathrm{m}, 4\ \mu\mathrm{m}]$. On the boundary $x=0$, we introduce the following signal,

$$H_z(x=0,y,t) = H_0\sin(\omega_c t)\mathrm{sech}(y/w), \tag{81}$$

where $\omega_c=4.35\times10^{15}$ rad/s is the carrier frequency. w, H_0 are the width and the magnitude of the incident wave, respectively, which will be specified in each case study. Since the signal (81) is injected via the magnetic field at $x=0$, we use Alternating II flux in this example, with the approximate numerical boundary treatments as in [22] on the top, right, bottom boundary of Ω. The mesh

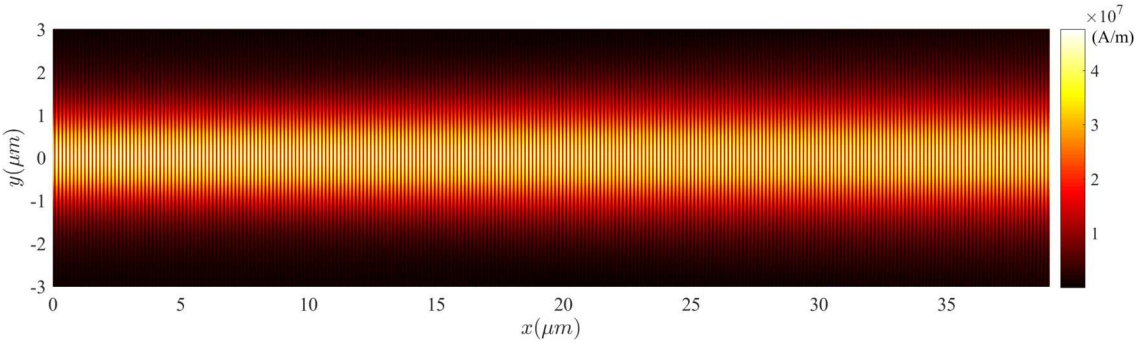

Fig. 9. 2D spatial-soliton propagation: snapshot of $|H_{zh}|$ at $T = 300$ fs for the fundamental soliton propagation, with $w = 667.0$ nm, $H_0 = 4.77 \times 10^7$ A/m, and $k = 2$.

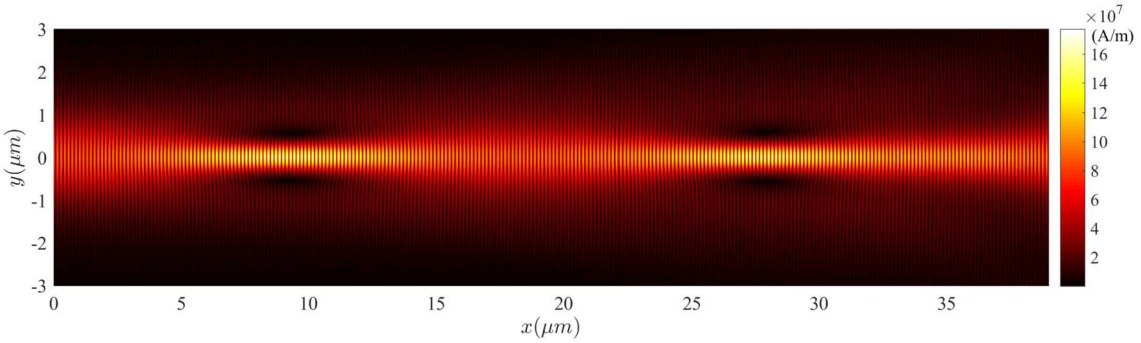

Fig. 10. 2D spatial-soliton propagation: snapshot of $|H_{zh}|$ at $T = 300$ fs for the second-order soliton propagation, with $w = 667.0$ nm, $H_0 = 2 \times 4.77 \times 10^7$ A/m, and $k = 2$.

in space is uniform, with $h = \Delta x = \Delta y = 20$ nm. The final time is $T = 300$ fs, with the time step as $\tau = 0.06\sqrt{\epsilon_0 \epsilon_\infty \mu_0} h$. The CPU time for each simulation is about 1500 seconds.

In Fig. 9, we present the snapshot of the magnetic field $|H_{zh}|$ in the domain of our interest $[0, 38\ \mu\text{m}] \times [-3\ \mu\text{m}, 3\ \mu\text{m}]$ at the final time T for the fundamental spatial soliton, whose parameters are taken as $w = 667$ nm and $H_0 = 4.77 \times 10^7$ A/m. Due to the focusing effects of the Kerr nonlinearity [8], the shape and magnitude of the fundamental spatial soliton merely change as it propagates in the optical glass. If we double the strength of incident wave (81), namely, $H_0 = 2 \times 4.77 \times 10^7$ A/m, a second-order soliton will be launched. Unlike the fundamental soliton, the width and the magnitude of the second-order soliton vary from location to location as shown in Fig. 10, exhibiting periodic focusing and defocusing effects. From the physical point of view, it is the interference between the two fundamental solitons that directly leads to this interesting optical phenomenon [8].

In Fig. 11, we further show the spectrum plots of $\mathsf{E}_{yh}(\omega)$ for these two cases. Here, $\mathsf{E}_{yh}(\omega)$ is obtained after the discrete Fourier transform is applied to the average of $E_{yh}(x, \cdot, t)$ along the y-direction at $x = 50$ nm over 200 periods, namely, over $[0, 2\pi/\omega_c \times 200]$. As expected, the third order harmonic waves are detected in the solution. Similar as in [23], second-order harmonic waves of weaker strength are also observed from such spectrum analysis.

4.2.3. 2D airhole scattering

In this example, we consider the propagation of a second-order soliton in an imperfect glass [14] with a computational domain $\Omega = [0, 32\ \mu\text{m}] \times [-12\ \mu\text{m}, 12\ \mu\text{m}]$. This imperfection is caused by an airhole centered at $(5\ \mu\text{m}, 0)$, modeled as material discontinuity specially with $a = b = 0$ in (80c) in the relevant subdomain of a size to be specified. The final time is $T = 160$ fs. We take $w = 667.0$ nm and $H_0 = 2 \times 4.77 \times 10^7$ A/m. All other physical parameters are the same as those used in Section 4.2.2. For this example, since the glasses are not uniform and the wave propagation is not paraxial, the full-vector Maxwell's equations are important for simulating the light-dielectric interaction. It takes about 1500 seconds for each simulation.

In Fig. 12, we plot the magnetic field $|H_{zh}|$ at $t = T$ when the size of the airhole is 250 nm × 250 nm (top) and 350 nm × 350 nm (bottom), respectively, over the domain of our interest $[0, 29\ \mu\text{m}] \times [-5\ \mu\text{m}, 5\ \mu\text{m}]$. After the interaction with the airhole, significant scattering of the electromagnetic field is observed, followed by a weaker-powered soliton reformed. With the smaller airhole (top), the newly reformed soliton becomes narrower and exhibits periodic focusing and defocusing similar to the second order soliton shown Fig. 10. With the larger airhole (bottom), the newly formed soliton has weaker intensity and propagates similarly as the fundamental soliton in Fig. 9. These results are in good agreement with those in [14] by FDTD methods and in [22] by the DG type nonlinear methods.

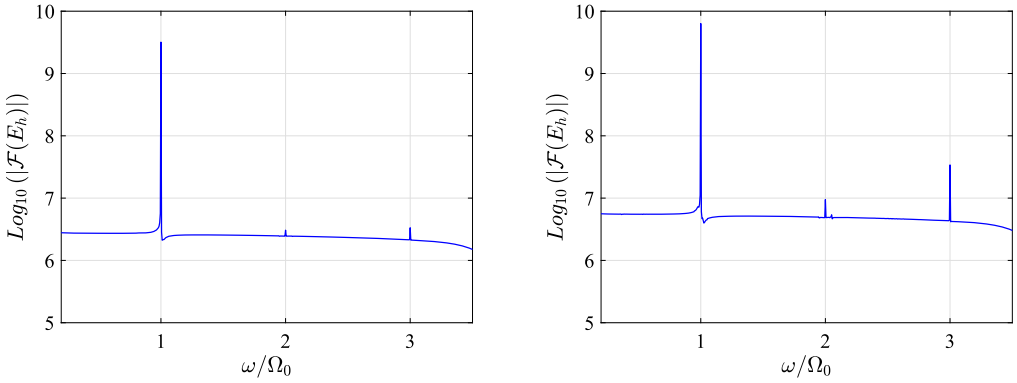

Fig. 11. 2D spatial-soliton propagation: semi-log plot of the spectrum of the average of E_{yh} in the y direction at $x = 50$ nm and with $k = 2$. Left: fundamental soliton, with $w = 667.0$ nm, $H_0 = 4.77 \times 10^7$ A/m, right: second-order soliton, with $w = 667.0$ nm, $H_0 = 2 \times 4.77 \times 10^7$ A/m.

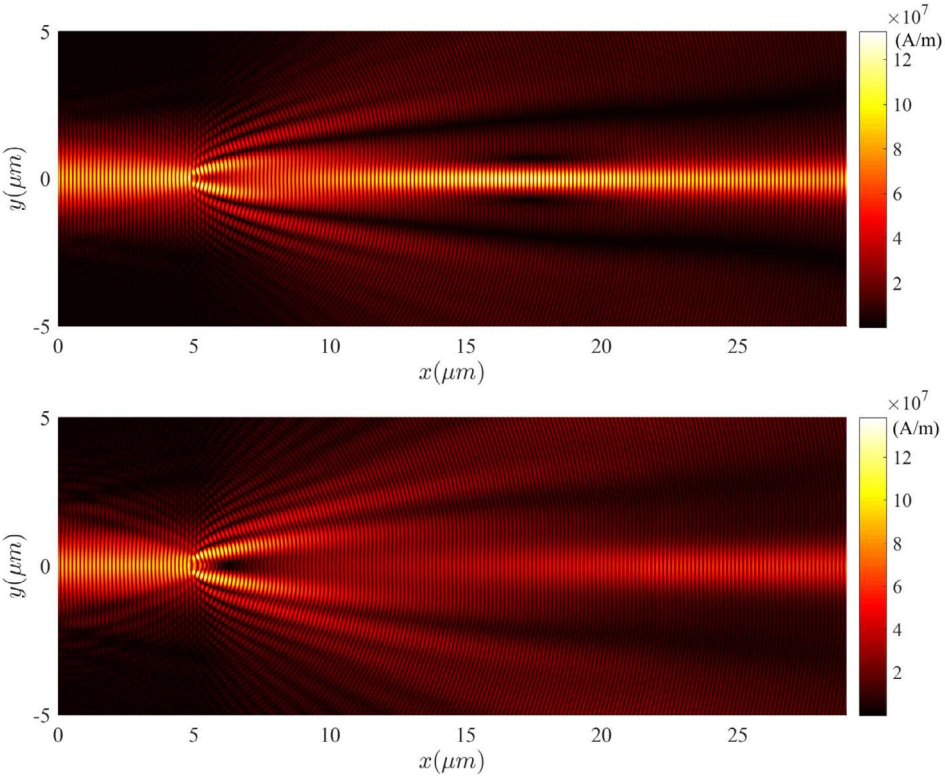

Fig. 12. 2D airhole scattering: snapshot of $|H_{zh}|$ at $T = 160$ fs, with $w = 667.0$ nm, $H_0 = 2 \times 4.77 \times 10^7$ A/m, and $k = 2$. Airhole size: 250 nm × 250 nm (top), 350nm × 350 nm (bottom).

4.2.4. 3D spatial-soliton propagation: effect of nonlinearity

In this final example, we turn to the simulation of a 3D spatial-soliton propagation. The governing equations are (1)-(2), with the parameters chosen as follows,

$$\omega_0 = 3.0 \times 10^{16} rad/s,\ \omega_{ps} = \sqrt{0.8}\omega_0,\ \gamma = 0,$$
$$\epsilon_\infty = 1.0,\ a = \lambda \times 1.89 \times 10^{-22} m^2/V^2,\ \theta = 0.3,$$
$$\gamma_v = \frac{2}{\tau_2},\ \omega_v = \sqrt{(\tau_1^2 + \tau_2^2)/(\tau_1^2 \tau_2^2)},\ \tau_1 = 10.0 fs,\ \tau_2 = 30.0 fs.$$

Here a new parameter λ is introduced as a multiplicative factor of the nonlinear strength parameter a. By tuning λ, one can examine the effect of the nonlinearity strength to the propagation of the soliton in an optical medium.

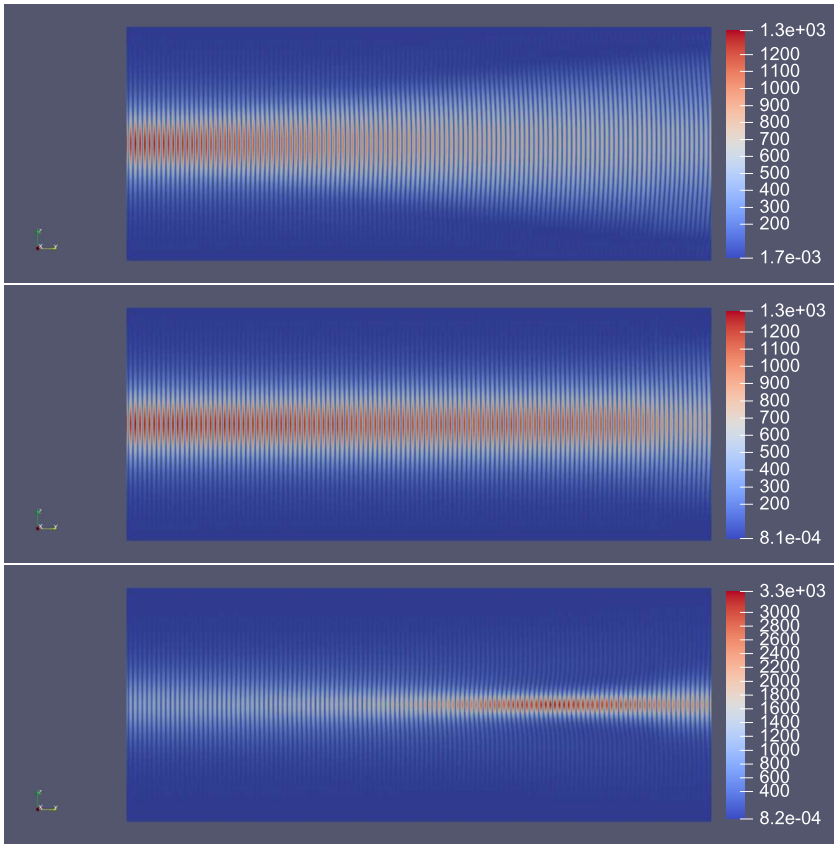

Fig. 13. 3D spatial-soliton propagation: sliced snapshot of $|\boldsymbol{E}_h|$ from the plane $z = 0$ at $T = 100$ fs, with $k = 1$. Top: $\lambda = 0$, middle: $\lambda = 1$, bottom: $\lambda = 2$.

The computational domain is $\Omega = [-4\ \mu\text{m}, 4\ \mu\text{m}] \times [0, 20\ \mu\text{m}] \times [-4\ \mu\text{m}, 4\ \mu\text{m}]$. The meshsize is $\Delta x = \Delta z = 40$ nm, $\Delta y = 25$ nm. The time step is set as $\tau = 0.15\sqrt{\epsilon_0 \epsilon_\infty \mu_0}/(1/\Delta x + 1/\Delta y + 1/\Delta z)$. At $y = 0$, a z-polarized incident wave enters, propagating in the positive y direction,

$$H_z(x, y = 0, z, t) = H_0 \sin(\omega_c t)\text{sech}\Big(\frac{\sqrt{x^2 + z^2}}{w}\Big), \tag{82}$$

with $H_0 = 4.77 \times 10^7$ A/m, $w = 667.0$ nm, $\omega_c = 4.35 \times 10^{15}$ rad/s.

We run the simulations up to the final time $T = 100$ fs when $\lambda = 0, 1, 2$ and each single run takes about 10000 seconds. In Fig. 13, we show the slices of the electric field $|\boldsymbol{E}_h|$ from the plane $z = 0$ at time $t = T$ for the three cases. One can observe that in the medium without the nonlinear effect ($\lambda = 0$), the introduced wave spreads out as it propagates. As the nonlinear effect increases moderately with $\lambda = 1$, the wave propagates with little variation in width and amplitude. Due to the focusing effect of the nonlinearity, the wave signal will become narrower as the nonlinearity further grows (with $\lambda = 2$).

5. Conclusion

In this paper, we develop a class of accurate and efficient numerical methods for simulating the propagation of electromagnetic waves in the optical Lorentz-Kerr-Raman medium, modeled by Maxwell's equations coupled with a constitutive relation describing some instantaneous and delayed linear and cubic nonlinear medium responses. The main contribution of this work to the algorithmic development lies in the design of computationally efficient linear methods, featured as being free of any nonlinear algebraic solvers, for the underlying nonlinear model. The proposed methods also respect the energy law for the special case of Lorentz-Kerr model. All these are achieved through careful formulations of temporal and spatial discretizations. The computational efficiency of the methods in the parallel implementation environment can be credited to the local nature of the methods as well as their explicitness for the PDE part. With the computational efficiency demonstrated by the proposed methods, this work further adds to our continuing efforts in developing accurate and robust numerical methods with provable properties for simulating nonlinear optics based on the full-vector Maxwell's equations.

Though optimal *a priori* error estimates are established for the proposed methods applied to the Lorentz-Kerr model, more intricate analysis techniques are needed to lift some stringent conditions (e.g. on the time step size, the approximation order of the discrete space). In the case of complex geometries, more general meshes such as those with d-simplex elements (i.e. triangles in 2D,

tetrahedrons in 3D) can be preferred. The methodology and the analysis in this work can be extended to more general meshes to design linear methods, as long as numerical quadrature rules of certain exactness with positive weights are available. In practice, the efficiency of the methods also relies on robust numerical boundary treatments with sufficient control of non-physical artifacts, and this deserves a systematic investigation especially for nonlinear and dispersive media.

CRediT authorship contribution statement

Maohui Lyu: Writing – review & editing, Writing – original draft, Visualization, Validation, Software, Methodology, Investigation, Funding acquisition, Formal analysis, Data curation, Conceptualization. **Fengyan Li:** Writing – review & editing, Writing – original draft, Validation, Supervision, Project administration, Methodology, Investigation, Funding acquisition, Formal analysis, Conceptualization.

Declaration of competing interest

The authors declare that they have no known competing financial interests or personal relationships that could have appeared to influence the work reported in this paper.

Data availability

Data will be made available on request.

Acknowledgements

In this project, the author Lyu was supported in part by NSFC Grants 12101597, 12271082 and 11871139 and the author Li was supported in part by NSF grant DMS-1913072.

Appendix A. Proof of Theorem 3

Proof. With the numerical fluxes in (11) being consistent, the exact solution satisfies $-(\nabla\times \boldsymbol{H}^{n+1/2},\boldsymbol{\phi})=\mathcal{B}_h^H(\boldsymbol{H}^{n+1/2},\boldsymbol{\phi})$ and $(\nabla\times \boldsymbol{E}^{n+1},\boldsymbol{\phi})=\mathcal{B}_h^E(\boldsymbol{E}^{n+1},\boldsymbol{\phi})$, $\forall\boldsymbol{\phi}\in V_h^k$, and

$$(\delta_\tau^{n+1/2}\boldsymbol{D},\boldsymbol{\phi})+\mathcal{B}_h^H(\boldsymbol{H}^{n+1/2},\boldsymbol{\phi})=(\boldsymbol{\tau}_{\boldsymbol{D}}^{n+1/2},\boldsymbol{\phi}),\qquad \forall\boldsymbol{\phi}\in V_h^k, \tag{A.1a}$$

$$\mu_0(\delta_\tau^{n+1}\boldsymbol{H},\boldsymbol{\phi})+\mathcal{B}_h^E(\boldsymbol{E}^{n+1},\boldsymbol{\phi})=\mu_0(\boldsymbol{\tau}_{\boldsymbol{H}}^{n+1},\boldsymbol{\phi}),\qquad \forall\boldsymbol{\phi}\in V_h^k, \tag{A.1b}$$

hence

$$(\delta_{2\tau}^n\boldsymbol{D},\boldsymbol{\phi})+\mathcal{B}_h^H(\overline{\boldsymbol{H}^n},\boldsymbol{\phi})=(\overline{\boldsymbol{\tau}_{\boldsymbol{D}}^n},\boldsymbol{\phi}),\qquad \forall\boldsymbol{\phi}\in V_h^k, \tag{A.2a}$$

$$\frac{\mu_0}{2}(\delta_\tau^{n+1}\boldsymbol{H}+\delta_\tau^{n-1}\boldsymbol{H},\boldsymbol{\phi})+\mathcal{B}_h^E(\overline{\boldsymbol{E}^n},\boldsymbol{\phi})=\mu_0(\overline{\overline{\boldsymbol{\tau}_{\boldsymbol{H}}^n}},\boldsymbol{\phi}),\qquad \forall\boldsymbol{\phi}\in V_h^k. \tag{A.2b}$$

Subtracting (A.2a) from (24a), and subtracting (A.2b) from (24b), we get two error equations

$$(\delta_{2\tau}^n(\boldsymbol{D}_h-\boldsymbol{D}),\boldsymbol{\phi})+\mathcal{B}_h^H(\overline{\xi_{\boldsymbol{H}}^n},\boldsymbol{\phi})=\mathcal{K}^n(\boldsymbol{\phi}),\qquad \forall\boldsymbol{\phi}\in V_h^k \tag{A.3a}$$

$$\frac{\mu_0}{2}(\delta_\tau^{n+1}\xi_{\boldsymbol{H}}+\delta_\tau^{n-1}\xi_{\boldsymbol{H}},\boldsymbol{\phi})+\mathcal{B}_h^E(\overline{\overline{\xi_{\boldsymbol{E}}^n}},\boldsymbol{\phi})=\mathcal{M}^n(\boldsymbol{\phi}),\qquad \forall\boldsymbol{\phi}\in V_h^k \tag{A.3b}$$

where $\mathcal{K}^n(\cdot)$ and $\mathcal{M}^n(\cdot)$ are given in (42a)-(42b).

From the constitutive relation in (2) and its discrete counterpart (8c), we reach the third error equation, again with $\forall\boldsymbol{\phi}\in V_h^k$,

$$(\delta_{2\tau}^n(\boldsymbol{D}_h-\boldsymbol{D}),\boldsymbol{\phi})=\epsilon_0(\epsilon_\infty\delta_{2\tau}^n\xi_{\boldsymbol{E}}+\delta_{2\tau}^n\xi_{\boldsymbol{P}},\boldsymbol{\phi})-\mathcal{L}^n(\boldsymbol{\phi})+a\mathcal{N}^n(\boldsymbol{\phi}), \tag{A.4}$$

with $\mathcal{L}^n(\cdot)$ and $\mathcal{N}^n(\cdot)$ given in (42c).

For the Lorentz term, we subtract (37c) from (8f), and obtain the fourth error equation

$$(\delta_{\tau^2}^n\xi_{\boldsymbol{P}}+\gamma\delta_{2\tau}^n\xi_{\boldsymbol{P}}+\omega_0^2\overline{\xi_{\boldsymbol{P}}^n}-\omega_p^2\overline{\overline{\xi_{\boldsymbol{E}}^n}},\boldsymbol{\phi})=\omega_p^2\epsilon_0^{-1}\mathcal{Q}(\boldsymbol{\phi}),\qquad \forall\boldsymbol{\phi}\in V_h^k, \tag{A.5}$$

with $\mathcal{Q}^n(\cdot)$ given in (42d).

Now by taking special test functions in error equations above, specifically, with $\boldsymbol{\phi}=\overline{\overline{\xi_{\boldsymbol{E}}^n}}$ in (A.3a) and (A.4), $\boldsymbol{\phi}=\overline{\xi_{\boldsymbol{H}}^n}$ in (A.3b), $\boldsymbol{\phi}=2\tau\delta_{2\tau}^n\xi_{\boldsymbol{P}}$ in (A.5), following a similar derivation as in **Step 1** of Theorem 2, we reach the master error relation in (39). □

Appendix B. Proof of Proposition 1

Proof. By subtracting (A.1b) from (8b), we get

$$\mu_0(\delta_\tau^{n+1}\xi_{\boldsymbol{H}},\boldsymbol{\phi})+\mathcal{B}_h^E(\xi_{\boldsymbol{E}}^{n+1},\boldsymbol{\phi})=\widehat{\mathcal{M}}^{n+1}(\boldsymbol{\phi}),\qquad \forall\boldsymbol{\phi}\in V_h^k \tag{B.1}$$

with

$$\widehat{\mathcal{M}}^{n+1}(\boldsymbol{\phi}):=\mu_0(\delta_\tau^{n+1}\eta_{\boldsymbol{H}},\boldsymbol{\phi})+\mathcal{B}_h^E(\eta_{\boldsymbol{E}}^{n+1},\boldsymbol{\phi})-\mu_0(\boldsymbol{\tau}_{\boldsymbol{H}}^{n+1},\boldsymbol{\phi}). \tag{B.2}$$

Using the approximation properties of V_h^k in Lemma 2, the bound on $\boldsymbol{\tau}_{\boldsymbol{H}}^{n+1}$ in Lemma 3, and a super-convergence result similar to (44) [10,20], we have

$$\left|\widehat{\mathcal{M}}^{n+1}(\boldsymbol{\phi})\right|\le C(h^{k+1}+\tau^2)\|\boldsymbol{\phi}\|,\qquad \forall\boldsymbol{\phi}\in V_h^k. \tag{B.3}$$

Following a similar derivation for (29) and based on (B.1), with $\lambda=C_\star v_\infty\tau/h$, we get the following with any $\rho\in(0,1)$,

$$\begin{aligned}\mu_0\int_\Omega\overline{\xi_{\boldsymbol{H}}^{n+1}}\cdot\overline{\xi_{\boldsymbol{H}}^{n}}d\Omega&\ge\mu_0\big(1-\frac{\lambda}{2}\big)\|\overline{\xi_{\boldsymbol{H}}^{n+1}}\|^2-\epsilon_0\epsilon_\infty\frac{\lambda}{4}\Big(\Big\|\xi_{\boldsymbol{E}}^{n+1}\Big\|^2+\Big\|\xi_{\boldsymbol{E}}^{n}\Big\|^2\Big)-\frac{\tau}{2}\big(\widehat{\mathcal{M}}^{n+1}+\widehat{\mathcal{M}}^{n}\big)(\overline{\xi_{\boldsymbol{H}}^{n+1}})\\&\ge\mu_0\big(1-\rho-\frac{\lambda}{2}\big)\|\overline{\xi_{\boldsymbol{H}}^{n+1}}\|^2-\epsilon_0\epsilon_\infty\frac{\lambda}{4}\Big(\Big\|\xi_{\boldsymbol{E}}^{n+1}\Big\|^2+\Big\|\xi_{\boldsymbol{E}}^{n}\Big\|^2\Big)-C_\rho C\tau^2(h^{2k+2}+\tau^4).\end{aligned} \tag{B.4}$$

Following a similar derivation for (30)-(31) and based on (B.1), we further obtain

$$\begin{aligned}4\mu_0\|\xi_{\boldsymbol{H}}^{n+1/2}\|^2&\le4\mu_0(1+\lambda)\|\overline{\xi_{\boldsymbol{H}}^{n+1}}\|^2+\epsilon_0\epsilon_\infty\frac{\lambda}{2}\Big\|\xi_{\boldsymbol{E}}^{n+1}\Big\|^2\\&\quad+4\mu_0\lambda\|\xi_{\boldsymbol{H}}^{n+1/2}\|^2-2\tau\widehat{\mathcal{M}}^{n+1}\big(\overline{\xi_{\boldsymbol{H}}^{n+1}}+\xi_{\boldsymbol{H}}^{n+1/2}\big)\\&\le4\mu_0(1+\rho+\lambda)\|\overline{\xi_{\boldsymbol{H}}^{n+1}}\|^2+\epsilon_0\epsilon_\infty\frac{\lambda}{2}\Big\|\xi_{\boldsymbol{E}}^{n+1}\Big\|^2\\&\quad+4\mu_0(\rho+\lambda)\|\xi_{\boldsymbol{H}}^{n+1/2}\|^2+C_\rho C\tau^2(h^{2k+2}+\tau^4),\end{aligned} \tag{B.5}$$

and therefore

$$\begin{aligned}\Big\|\xi_{\boldsymbol{H}}^{n+1/2}\Big\|^2&\le\frac{1+\rho+\lambda}{1-\rho-\lambda}\|\overline{\xi_{\boldsymbol{H}}^{n+1}}\|^2+\frac{\epsilon_0\epsilon_\infty}{\mu_0}\frac{\lambda}{8(1-\rho-\lambda)}\Big\|\xi_{\boldsymbol{E}}^{n+1}\Big\|^2\\&\quad+\frac{C_\rho C}{4\mu_0(1-\rho-\lambda)}\tau^2(h^{2k+2}+\tau^4),\end{aligned} \tag{B.6}$$

under the condition

$$\lambda<1-\rho. \tag{B.7}$$

Combining (B.4) and (B.6), we reach

$$\begin{aligned}&\mu_0\int_\Omega\overline{\xi_{\boldsymbol{H}}^{n+1}}\cdot\overline{\xi_{\boldsymbol{H}}^{n}}d\Omega-\frac{\mu_0}{2}\|\xi_{\boldsymbol{H}}^{n+1/2}\|^2+\frac{\epsilon_0\epsilon_\infty}{4}(\|\xi_{\boldsymbol{E}}^{n+1}\|^2+\|\xi_{\boldsymbol{E}}^{n}\|^2)\\&\ge\frac{\mu_0}{2}\big(2(1-\rho)-\lambda-\frac{1+\rho+\lambda}{1-\rho-\lambda}\big)\|\overline{\xi_{\boldsymbol{H}}^{n+1}}\|^2\\&\quad+\frac{\epsilon_0\epsilon_\infty}{4}\big(1-\lambda-\frac{\lambda/4}{1-\rho-\lambda}\big)\Big(\Big\|\xi_{\boldsymbol{E}}^{n+1}\Big\|^2+\Big\|\xi_{\boldsymbol{E}}^{n}\Big\|^2\Big)-\frac{C_\rho C}{8(1-\rho-\lambda)}\tau^2(h^{2k+2}+\tau^4).\end{aligned} \tag{B.8}$$

Now we require λ to satisfy (B.7) and

$$2(1-\rho)-\lambda-\frac{1+\rho+\lambda}{1-\rho-\lambda}\ge\rho,\quad 1-\lambda-\frac{\lambda/4}{1-\rho-\lambda}\ge\rho, \tag{B.9}$$

In order for such positive λ to exist, we further restrict $\rho\in(0,1-\sqrt{2/3})$ (this can be seen by examining (B.9) with $\lambda=0$). Now we take $\rho=\rho_{err}$ with a pre-set $\rho_{err}\in(0,1-\sqrt{2/3})$, then (B.7) and (B.9) will be simplified as

$$\lambda\le2(1-\rho_{err})-\sqrt{(\rho_{err}-1)^2+2},$$

hence the time step condition (47). The estimate in (46) then follows along with (49). □

Appendix C. Proof of Corollary 1

Proof. With a direct calculation and $\boldsymbol{E}_h^n = \boldsymbol{A}_h^n + \xi_{\boldsymbol{E}}^n$, we proceed as follows,

$$
\begin{aligned}
&\left(|\boldsymbol{E}_h^n|^2\mathbb{I} + 2\boldsymbol{E}_h^n\boldsymbol{E}_h^{n\top}\right)\delta_{2\tau}^n\boldsymbol{E}_h - \left(|\boldsymbol{E}^n|^2\mathbb{I} + 2\boldsymbol{E}^n\boldsymbol{E}^{n\top}\right)\delta_{2\tau}^n\boldsymbol{E}\\
=&\big(|\xi_{\boldsymbol{E}}^n|^2\mathbb{I} + 2\xi_{\boldsymbol{E}}^n\xi_{\boldsymbol{E}}^{n\top} + 2\boldsymbol{A}_h^n\cdot\xi_{\boldsymbol{E}}^n\mathbb{I} + 2\boldsymbol{A}_h^n\xi_{\boldsymbol{E}}^{n\top} + 2\xi_{\boldsymbol{E}}^n\boldsymbol{A}_h^{n\top}\big)\delta_{2\tau}^n\boldsymbol{A}_h\\
&+\big(|\boldsymbol{A}_h^n|^2\mathbb{I} + 2\boldsymbol{A}_h^n\cdot\xi_{\boldsymbol{E}}^n\mathbb{I} + |\xi_{\boldsymbol{E}}^n|^2\mathbb{I} + 2\boldsymbol{A}_h^n\boldsymbol{A}_h^{n\top} + 2\boldsymbol{A}_h^n\xi_{\boldsymbol{E}}^{n\top} + 2\xi_{\boldsymbol{E}}^n\boldsymbol{A}_h^{n\top} + 2\xi_{\boldsymbol{E}}^n\xi_{\boldsymbol{E}}^{n\top}\big)\delta_{2\tau}^n\xi_{\boldsymbol{E}}\\
&+\big(|\boldsymbol{A}_h^n|^2\mathbb{I} + 2\boldsymbol{A}_h^n\boldsymbol{A}_h^{n\top}\big)\delta_{2\tau}^n\boldsymbol{A}_h - \left(|\boldsymbol{E}^n|^2\mathbb{I} + 2\boldsymbol{E}^n\boldsymbol{E}^{n\top}\right)\delta_{2\tau}^n\boldsymbol{E}\\
=&\big(|\xi_{\boldsymbol{E}}^n|^2\mathbb{I} + 2\xi_{\boldsymbol{E}}^n\xi_{\boldsymbol{E}}^{n\top} + 2\boldsymbol{A}_h^n\cdot\xi_{\boldsymbol{E}}^n\mathbb{I} + 2\boldsymbol{A}_h^n\xi_{\boldsymbol{E}}^{n\top} + 2\xi_{\boldsymbol{E}}^n\boldsymbol{A}_h^{n\top}\big)\delta_{2\tau}^n\boldsymbol{A}_h\\
&+\big(|\eta_{\boldsymbol{E}}^n|^2\mathbb{I} - 2\boldsymbol{E}^n\cdot\eta_{\boldsymbol{E}}^n\mathbb{I} + 2\eta_{\boldsymbol{E}}^n\eta_{\boldsymbol{E}}^{n\top} - 2\boldsymbol{E}^n\eta_{\boldsymbol{E}}^{n\top} - 2\eta_{\boldsymbol{E}}^n\boldsymbol{E}^{n\top}\big)\delta_{2\tau}^n\boldsymbol{E}\\
&-\big(|\boldsymbol{A}_h^n|^2\mathbb{I} + 2\boldsymbol{A}_h^n\boldsymbol{A}_h^{n\top}\big)\delta_{2\tau}^n\eta_{\boldsymbol{E}} + \big(|\xi_{\boldsymbol{E}}^n|^2\mathbb{I} + 2\xi_{\boldsymbol{E}}^n\xi_{\boldsymbol{E}}^{n\top}\big)\delta_{2\tau}^n\xi_{\boldsymbol{E}}\\
&+\big(|\boldsymbol{A}_h^n|^2\mathbb{I} + 2\boldsymbol{A}_h^n\boldsymbol{A}_h^{n\top} + 2\boldsymbol{A}_h^n\cdot\xi_{\boldsymbol{E}}^n\mathbb{I} + 2\boldsymbol{A}_h^n\xi_{\boldsymbol{E}}^{n\top} + 2\xi_{\boldsymbol{E}}^n\boldsymbol{A}_h^{n\top}\big)\delta_{2\tau}^n\xi_{\boldsymbol{E}}.
\end{aligned}
$$

Here for the last equality, $\boldsymbol{A}_h^n = \boldsymbol{E}^n - \eta_{\boldsymbol{E}}^n$ is used. With this,

$$
\mathcal{N}^n(\overline{\overline{\xi_{\boldsymbol{E}}^n}}) = \sum_{i=1}^4 \mathcal{S}_i^n + \mathcal{S}_5^{n,(1)} + \mathcal{S}_5^{n,(2)} \tag{C.1}
$$

where $\mathcal{S}_i^n, i = 1,2,3,4$ are defined in (60) and

$$
\mathcal{S}_5^{n,(1)} = \epsilon_0\Big(\mathcal{I}_h\big((|\xi_{\boldsymbol{E}}^n|^2\mathbb{I} + 2\xi_{\boldsymbol{E}}^n\xi_{\boldsymbol{E}}^{n\top})\delta_{2\tau}^n\xi_{\boldsymbol{E}}\big), \overline{\overline{\xi_{\boldsymbol{E}}^n}}\Big), \tag{C.2a}
$$

$$
\mathcal{S}_5^{n,(2)} = \epsilon_0\Big(\mathcal{I}_h\big((|\boldsymbol{A}_h^n|^2\mathbb{I} + 2\boldsymbol{A}_h^n\boldsymbol{A}_h^{n\top} + 2\boldsymbol{A}_h^n\cdot\xi_{\boldsymbol{E}}^n\mathbb{I} + 2\boldsymbol{A}_h^n\xi_{\boldsymbol{E}}^{n\top} + 2\xi_{\boldsymbol{E}}^n\boldsymbol{A}_h^{n\top})\delta_{2\tau}^n\xi_{\boldsymbol{E}}\big), \overline{\overline{\xi_{\boldsymbol{E}}^n}}\Big). \tag{C.2b}
$$

Using the property of $\mathcal{I}_h$ in Lemma 6, one has

$$
\mathcal{S}_5^{n,(1)} = \frac{\epsilon_0}{4\tau}\left(\|\mathcal{I}_h(|\xi_{\boldsymbol{E}}^{n+1}||\xi_{\boldsymbol{E}}^n|)\|^2 + 2\|\mathcal{I}_h(\xi_{\boldsymbol{E}}^{n+1}\cdot\xi_{\boldsymbol{E}}^n)\|^2 - \|\mathcal{I}_h(|\xi_{\boldsymbol{E}}^n||\xi_{\boldsymbol{E}}^{n-1}|)\|^2 - 2\|\mathcal{I}_h(\xi_{\boldsymbol{E}}^n\cdot\xi_{\boldsymbol{E}}^{n-1})\|^2\right). \tag{C.3}
$$

To deal with $\mathcal{S}_5^{n,(2)}$, we first derive an identity for any $b^n, b^{n+1} \in \mathbb{R}^m$, together with any C^n either being a scalar or in $\mathbb{R}^{m\times m}$, with $m \in \mathbb{N}$,

$$
\begin{aligned}
&{b^{n+1}}^\top C^n b^{n+1} - {b^{n-1}}^\top C^n b^{n-1}\\
=&{b^{n+1}}^\top C^n b^{n+1} + {b^n}^\top C^n b^n - {b^n}^\top C^{n-1} b^n - {b^{n-1}}^\top C^{n-1} b^{n-1}\\
&-\tau {b^n}^\top(\delta_\tau^{n-1/2}C)b^n - {b^{n-1}}^\top(\delta_\tau^{n-1/2}C)b^{n-1}.
\end{aligned}
\tag{C.4}
$$

The key principle is that the last two terms in (C.4) no longer involve terms with the index $n+1$.

By taking $C = |\boldsymbol{A}_h|^2$ and $b = |\xi_{\boldsymbol{E}}|$ in (C.4), we have

$$
\begin{aligned}
&\Big(\mathcal{I}_h(|\boldsymbol{A}_h^n|^2\delta_{2\tau}^n\xi_{\boldsymbol{E}}), \overline{\overline{\xi_{\boldsymbol{E}}^n}}\Big)\\
=&\frac{1}{4\tau}\int_\Omega \mathcal{I}_h\Big(|\boldsymbol{A}_h^n|^2(|\xi_{\boldsymbol{E}}^{n+1}|^2 + |\xi_{\boldsymbol{E}}^n|^2)\Big)d\Omega - \frac{1}{4\tau}\int_\Omega \mathcal{I}_h\Big(|\boldsymbol{A}_h^{n-1}|^2(|\xi_{\boldsymbol{E}}^n|^2 + |\xi_{\boldsymbol{E}}^{n-1}|^2)\Big)d\Omega\\
&-\frac{1}{4}\int_\Omega \mathcal{I}_h\Big(\delta_\tau^{n-1/2}(|\boldsymbol{A}_h|^2)(|\xi_{\boldsymbol{E}}^n|^2 + |\xi_{\boldsymbol{E}}^{n-1}|^2)\Big)d\Omega.
\end{aligned}
\tag{C.5}
$$

By taking $C = \boldsymbol{A}_h\boldsymbol{A}_h^\top$ and $b = \xi_{\boldsymbol{E}}$ in (C.4), we have

$$
\begin{aligned}
&\Big(\mathcal{I}_h(\boldsymbol{A}_h^n{\boldsymbol{A}_h^n}^\top\delta_{2\tau}^n\xi_{\boldsymbol{E}}), \overline{\overline{\xi_{\boldsymbol{E}}^n}}\Big)\\
=&\frac{1}{4\tau}\int_\Omega \mathcal{I}_h\Big((\boldsymbol{A}_h^n\cdot\xi_{\boldsymbol{E}}^{n+1})^2 + (\boldsymbol{A}_h^n\cdot\xi_{\boldsymbol{E}}^n)^2\Big)d\Omega - \frac{1}{4\tau}\int_\Omega \mathcal{I}_h\Big((\boldsymbol{A}_h^{n-1}\cdot\xi_{\boldsymbol{E}}^n)^2 + (\boldsymbol{A}_h^{n-1}\cdot\xi_{\boldsymbol{E}}^{n-1})^2\Big)d\Omega\\
&-\frac{1}{4}\int_\Omega \mathcal{I}_h\Big({\xi_{\boldsymbol{E}}^n}^\top\delta_\tau^{n-1/2}(\boldsymbol{A}_h\boldsymbol{A}_h^\top)\xi_{\boldsymbol{E}}^n\Big)d\Omega - \frac{1}{4}\int_\Omega \mathcal{I}_h\Big({\xi_{\boldsymbol{E}}^{n-1}}^\top\delta_\tau^{n-1/2}(\boldsymbol{A}_h\boldsymbol{A}_h^\top)\xi_{\boldsymbol{E}}^{n-1}\Big)d\Omega.
\end{aligned}
\tag{C.6}
$$

By taking $C = \boldsymbol{A}_h\cdot\xi_{\boldsymbol{E}}$ and $b = |\xi_{\boldsymbol{E}}|$ in (C.4), we have

$$
\Big(\mathcal{I}_h((\boldsymbol{A}_h^n\cdot\xi_{\boldsymbol{E}}^n)\delta_{2\tau}^n\xi_{\boldsymbol{E}}), \overline{\overline{\xi_{\boldsymbol{E}}^n}}\Big)
$$

$$=\frac{1}{4\tau}\int_{\Omega}\mathcal{I}_h\Big((\boldsymbol{A}_h^n\cdot\xi_{\boldsymbol{E}}^n)(|\xi_{\boldsymbol{E}}^{n+1}|^2+|\xi_{\boldsymbol{E}}^n|^2)\Big)d\Omega-\frac{1}{4\tau}\int_{\Omega}\mathcal{I}_h\Big((\boldsymbol{A}_h^{n-1}\cdot\xi_{\boldsymbol{E}}^{n-1})(|\xi_{\boldsymbol{E}}^n|^2+|\xi_{\boldsymbol{E}}^{n-1}|^2)\Big)d\Omega$$
$$-\frac{1}{4}\int_{\Omega}\mathcal{I}_h\Big(\delta_\tau^{n-1/2}(\boldsymbol{A}_h\cdot\xi_{\boldsymbol{E}})(|\xi_{\boldsymbol{E}}^n|^2+|\xi_{\boldsymbol{E}}^{n-1}|^2)\Big)d\Omega. \tag{C.7}$$

By taking $C=\boldsymbol{A}_h\xi_{\boldsymbol{E}}^{\top}$ and $b=\xi_{\boldsymbol{E}}$ in (C.4), we have

$$\Big(\mathcal{I}_h((\boldsymbol{A}_h^n\xi_{\boldsymbol{E}}^{n\top}+\xi_{\boldsymbol{E}}^n\boldsymbol{A}_h^{n\top})\delta_{2\tau}^n\xi_{\boldsymbol{E}}),\overline{\overline{\xi_{\boldsymbol{E}}^n}}\Big)$$
$$=\frac{1}{2\tau}\int_{\Omega}\mathcal{I}_h\Big(\xi_{\boldsymbol{E}}^{n+1\top}\boldsymbol{A}_h^n\xi_{\boldsymbol{E}}^{n\top}\xi_{\boldsymbol{E}}^{n+1}-\xi_{\boldsymbol{E}}^{n-1\top}\boldsymbol{A}_h^n\xi_{\boldsymbol{E}}^{n\top}\xi_{\boldsymbol{E}}^{n-1}\Big)d\Omega$$
$$=\frac{1}{2\tau}\int_{\Omega}\mathcal{I}_h\Big((\boldsymbol{A}_h^n\cdot\xi_{\boldsymbol{E}}^{n+1})(\xi_{\boldsymbol{E}}^n\cdot\xi_{\boldsymbol{E}}^{n+1})+(\boldsymbol{A}_h^n\cdot\xi_{\boldsymbol{E}}^n)|\xi_{\boldsymbol{E}}^n|^2\Big)d\Omega$$
$$-\frac{1}{2\tau}\int_{\Omega}\mathcal{I}_h\Big((\boldsymbol{A}_h^{n-1}\cdot\xi_{\boldsymbol{E}}^n)(\xi_{\boldsymbol{E}}^{n-1}\cdot\xi_{\boldsymbol{E}}^n)+(\boldsymbol{A}_h^{n-1}\cdot\xi_{\boldsymbol{E}}^{n-1})|\xi_{\boldsymbol{E}}^{n-1}|^2\Big)d\Omega$$
$$-\frac{1}{2}\int_{\Omega}\mathcal{I}_h\Big(\xi_{\boldsymbol{E}}^{n\top}\delta_\tau^{n-1/2}(\boldsymbol{A}_h\xi_{\boldsymbol{E}}^{\top})\xi_{\boldsymbol{E}}^n\Big)d\Omega-\frac{1}{2}\int_{\Omega}\mathcal{I}_h\Big(\xi_{\boldsymbol{E}}^{n-1\top}\delta_\tau^{n-1/2}(\boldsymbol{A}_h\xi_{\boldsymbol{E}}^{\top})\xi_{\boldsymbol{E}}^{n-1}\Big)d\Omega. \tag{C.8}$$

Organizing the terms above, we have

$$\mathcal{S}_5^{n,(1)}+\mathcal{S}_5^{n,(2)}=\frac{1}{\tau}(\widetilde{\mathcal{E}^{n+1/2}}-\widetilde{\mathcal{E}^{n-1/2}})+\mathcal{S}_5, \tag{C.9}$$

with $\widetilde{\mathcal{E}^{n+1/2}}$ given in (61) and $\mathcal{S}_5^n$ in (60), hence we reach the reformulated master error relation (58). □

References

[1] Govind P. Agrawal, Nonlinear fiber optics, in: Nonlinear Science at the Dawn of the 21st Century, Springer, 2000, pp. 195–211.
[2] Anees Asad, Lutz Angermann, Energy-stable time-domain finite element methods for the 3D nonlinear Maxwell's equations, IEEE Photonics J. 12 (2) (2020) 1–15.
[3] Kim S. Bey, J. Tinsley Oden, Abani Patra, A parallel hp-adaptive discontinuous Galerkin method for hyperbolic conservation laws, Appl. Numer. Math. 20 (4) (1996) 321–336.
[4] Rupak Biswas, Karen D. Devine, Joseph E. Flaherty, Parallel, adaptive finite element methods for conservation laws, Appl. Numer. Math. 14 (1–3) (1994) 255–283.
[5] Vrushali A. Bokil, Yingda Cheng, Yan Jiang, Fengyan Li, Energy stable discontinuous Galerkin methods for Maxwell's equations in nonlinear optical media, J. Comput. Phys. 350 (2017) 420–452.
[6] Vrushali A. Bokil, Yingda Cheng, Yan Jiang, Fengyan Li, Puttha Sakkaplangkul, High spatial order energy stable FDTD methods for Maxwell's equations in nonlinear optical media in one dimension, J. Sci. Comput. 77 (1) (2018) 330–371.
[7] Robert W. Boyd, Nonlinear Optics, Academic Press, 2003.
[8] Chin-Lin Chen, Optical Solitons in Optical Fibers, John Wiley & Sons, Inc., 2005.
[9] Philippe G. Ciarlet, Finite Element Method for Elliptic Problems, Society for Industrial and Applied Mathematics, USA, 2002.
[10] Bernardo Cockburn, Guido Kanschat, Ilaria Perugia, Dominik Schötzau, Superconvergence of the local discontinuous Galerkin method for elliptic problems on Cartesian grids, SIAM J. Numer. Anal. 39 (1) (2001) 264–285.
[11] Jason Michael Cornelius, Dual grid finite-difference time-domain method for Maxwell equations in complex media, PHD Thesis, 2019.
[12] L. Gilles, S.C. Hagness, L. Vázquez, Comparison between staggered and unstaggered finite-difference time-domain grids for few-cycle temporal optical soliton propagation, J. Comput. Phys. 161 (2) (2000) 379–400.
[13] P.M. Goorjian, A. Taflove, R.M. Joseph, S.C. Hagness, Computational modeling of femtosecond optical solitons from Maxwell's equations, IEEE J. Quantum Electron. 28 (10) (1992) 2416–2422.
[14] Jethro Greene, Allen Taflove, Scattering of spatial optical solitons by subwavelength air holes, IEEE Microw. Wirel. Compon. Lett. 17 (2007) 760–762.
[15] Jethro H. Greene, Allen Taflove, General vector auxiliary differential equation finite-difference time-domain method for nonlinear optics, Opt. Express 14 (18) (2006) 8305–8310.
[16] Jan S. Hesthaven, Tim Warburton, Nodal Discontinuous Galerkin Methods: Algorithms, Analysis, and Applications, Springer Science & Business Media, 2007.
[17] Yunqing Huang, Jichun Li, Bin He, A time-domain finite element scheme and its analysis for nonlinear Maxwell's equations in Kerr media, J. Comput. Phys. 435 (2021) 110259.
[18] R.M. Joseph, A. Taflove, FDTD Maxwell's equations models for nonlinear electrodynamics and optics, IEEE Trans. Antennas Propag. 45 (3) (1997) 364–374.
[19] Buyang Li, Weiwei Sun, Error analysis of linearized semi-implicit Galerkin finite element methods for nonlinear parabolic equations, Int. J. Numer. Anal. Model. 10 (3) (2013).
[20] Jichun Li, Cengke Shi, Chi Wang Shu, Optimal non-dissipative discontinuous Galerkin methods for Maxwell's equations in Drude metamaterials, Comput. Math. Appl. 73 (8) (2017) 1760–1780.
[21] Jinjie Liu, Jason Cornelius, Moysey Brio, FDTD method with explicit non-iterative and second order treatment for Kerr nonlinearities, IEEE J. Multiscale Multiphys. Comput. Tech. 7 (2022) 195–199.
[22] Maohui Lyu, Vrushali A. Bokil, Yingda Cheng, Fengyan Li, Energy stable nodal discontinuous Galerkin methods for nonlinear Maxwell's equations in multi-dimensions, J. Sci. Comput. 89 (2021) 1–42.
[23] Maohui Lyu, Vrushali A. Bokil, Yingda Cheng, Fengyan Li, Energy stable nodal DG methods for Maxwell's equations of mixed-order form in nonlinear optical media, Commun. Appl. Math. Comput. (2022) 1–34.
[24] Ivan S. Maksymov, Andrey A. Sukhorukov, Andrei V. Lavrinenko, Yuri S. Kivshar, Comparative study of FDTD-adopted numerical algorithms for Kerr nonlinearities, IEEE Antennas Wirel. Propag. Lett. 10 (2011) 143–146.

[25] Geoffrey New, Introduction to Nonlinear Optics, Cambridge University Press, 2011.
[26] P. Tran, Photonic-band-structure calculation of material possessing Kerr nonlinearity, Phys. Rev. B 52 (Oct 1995) 10673–10676.
[27] R.W. Ziolkowski, The incorporation of microscopic material models into the FDTD approach for ultrafast optical pulse simulations, IEEE Trans. Antennas Propag. 45 (3) (1997) 375–391.